Conversion of greenhouse gases to value added products assisted by catalytic nonthermal plasma

Shaik Mahammadunnisa

A Dissertation Submitted to

Indian Institute of Technology Hyderabad

In Partial Fulfillment of the Requirements for

The Degree of Doctor of Philosophy

Department of Chemistry

July, 2014

Declaration

I declare that this written submission represents my ideas in my own words, and where others' ideas or words have been included, I have adequately cited and referenced the original sources. I also declare that I have adhered to all principles of academic honesty and integrity and have not misrepresented or fabricated or falsified any idea/data/fact/source in my submission. I understand that any violation of the above will be a cause for disciplinary action by the Institute and can also evoke penal action from the sources that have thus not been properly cited, or from whom proper permission has not been taken when needed.

Sk. Mahammadunnisa

(Signature)

(Shaik Mahammadunnisa)

(cy10p012)

ii

Approval Sheet

This thesis entitled **"Conversion of greenhouse gases to value added products assisted by catalytic nonthermal plasma"** by Shaik Mahammadunnisa is approved for the degree of Doctor of Philosophy from IIT Hyderabad.

22/oct/2014

-Name and affiliation-
Examiner

22/10/2014

-Name and affiliation-
Examiner

-Name and affiliation-
Adviser

-Name and affiliation-
Co-Adviser

-Name and affiliation-
Chairman

iii

Acknowledgements

First, I would like to express my sincere appreciation to Dr. Ch. Subrahmanyam for his invaluable guidance with constant flow of exciting new ideas and great source of help and encouragement throughout my Ph.D. Also, I would like to extend my thanks to Doctoral committee members.

I am particularly thankful to my friends Mr. J. Karuppiah, Mr. E. Lingareddy, Mr. P. Manoj Kumar Reddy, Ms. A. Dayamani, Mr. K. Krushnamurthy and chemistry department scholars from IIT-Hyderabad for their invaluable support, help, friendliness and encouragement.

The financial assistance from Council of Scientific and industrial research- New Delhi, India, was gratefully acknowledged.

I am grateful to my family; my mother, father, sisters and brothers for the patience and understanding they have shown on the other side of an ocean during my long lasting studies.

Last but not least, I am grateful to my husband Abdul Salam and my daughter Shahana Shajia, for all their love, encouragement, and support. Especially he gave tremendous support during the last year of my graduate studies that coincided with my first pregnancy.

This thesis would not have been possible without the positive input of a great many individual people. It seems inevitable that I will fail to thank everyone, so accept my apologies in advance if you have been left off the list.

SHAIK MAHAMMADUNNISA

Dedicated to

My Parents

and

My Husband

Abstract

The negative impact the greenhouse gases, especially carbon dioxide (CO_2), methane (CH_4) and nitrous oxide (N_2O) on the environment is well established and development of suitable technologies is warranted in order to regulate their increasing concentrations in the atmosphere. Co-processing of these gases has the advantage of waste minimization, energy production, resource utilization and pollution control. However, as the activation of these gases is highly endothermic, conventional thermocatalytic techniques may not be effective. In this context, nonthermal plasma (NTP) generated by electrical discharges was proposed as an alternative to the conventional methods. NTP created by electrical discharges generate the energetic electrons that colloid with the target gas molecules to decompose them without increasing the temperature of the back ground gas. However, as NTP is non–selective, catalytic NTP was proposed, in order to improve the selectivity to the desired product. The objectives of this research work were to explore NTP for the conversion of the selected greenhouse gases to value added products and to arrive at the suitable catalyst combination to obtain the best selectivity to the desired products like syngas and methanol. This presentation will focus on

- The design of NTP reactors and the fundamental understanding of the discharge characteristics with and without catalyst packing.
- Activation of selected individual greenhouse gases (CH_4, CO_2 and N_2O) and optimization of various parameters like the input power, catalyst addition and residence time in improving the efficiency of the process.
- CO_2 reduction by *in-situ* decomposition of H_2O and the influence of various parameters on the selectivity to the syngas.
- Co-processing CH_4 with CO_2 (dry reforming) for syngas production and influence of various parameters like input power, catalyst, water vapor, etc in controlling the selectivity.
- Partial oxidation of CH_4 to CH_3OH by *in-situ* decomposition of N_2O and optimization of the parameters like input power, catalyst, water vapor, etc in controlling the selectivity to CH_3OH.

Nomenclature

IPCC	**International Panel on Climate Change**
GHG	**Greenhouse Gas**
AC	**Alternating Current**
DC	**Direct Current**
RF	**Radio Frequency**
DBD	**Dielectric Barrier Discharge**
PCD	**Pulsed Corona Discharge**
GC	**Gas Chromatograph**
NTP	**Nonthermal Plasma**
SIE	**Specific Input Energy**
MFC	**Mass Flow Controller**
TCD	**Thermal Conductivity Detector**
SS	**Stainless Steel**
SMR	**Steam Methane Reforming**
POMR	**Partial Oxidation of Methane Reforming**
ATR	**Autothermal reforming of methane**
F-T	**Fischer-Tropsch**
PEM	**Proton Exchange Membrane**
Vol%	**Volume in percentage**
ppm	**parts per million**
PVD	**Physical Vapor Deposition**
PECVD	**Plasma Enhanced Chemical Vapor Deposition**
APGD	**Atmospheric Pressure Glow Discharge**
GTL	**Gas-to-liquid**
XRD	**X-ray diffraction**
TEM	**Transmission Electron Microscope**

Contents

LIST OF TABLES

LIST OF FIGURES

CHAPTER 1
INTRODUCTION

1.1. Preface

As the population is growing at a rapid rate, there is an immediate need to increase the energy production strategies in order to meet the increasing demand. It is estimated that world's energy demand may increase by 44% by 2030, due to rapid growth of developing nations [1]. The pressing issue in establishing a sustainable environment is to have a positive energy balance during fuel production and electricity generation. Since the beginning of the industrial revolution in the 18th century, the world has relied heavily on the fossil fuels like oil, coal, and natural gas that are the deposits of ancient organic rests [2]. But the fossil fuel reserves (such as crude oil) are depleting, yet demand continues to raise [1]. At the same time, the oil refineries are experiencing a declining production of the fuel and there are limited oil prospects identified [1].

The most striking problem associated with the combustion of fossil fuels is the emission of large amounts of greenhouse gases into the atmosphere. Carbon dioxide (CO_2), nitrogen dioxide (NO_2) and many of the volatile organic compounds (VOCs) are greenhouse gases and are thought to be the contributors to the increasing global temperature [2]. An increase in the global temperature may lead to ruinous problems, such as, melting of the polar ice caps, a subsequent rise in the sea levels and varied patterns of the weather. Figure 1.1 shows the world's heavy reliance on oil, gas and coal compared with other, cleaner energy options [3].

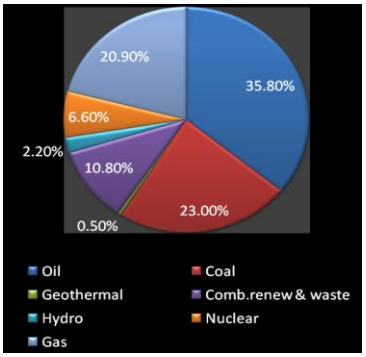

Figure 1.1: Part of total primary energy supplies in 2001 for the world [1].

1. 1.1. Global Warming

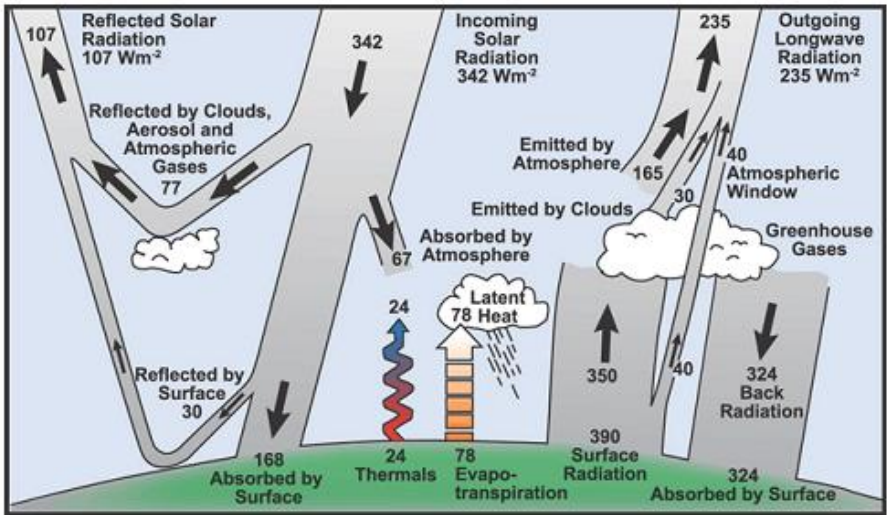

Figure 1.2: **A sketch of the Earths annual energy balance illustrating the incoming radiation from the sun and the radiated energy from earth surface. All the numbers are in Wm^{-2}, the width of arrows is proportional to their importance (This sketch is taken from [2]).**

Global warming occurs when greenhouse gases (primarily carbon dioxide (CO_2), nitrous oxide (N_2O), methane (CH_4),ozone (O_3), hydrofluorocarbons (HFCs), perfluorocarbons(PFCs) and sulphur hexafluoride (SF_6)) absorb Earth rejected solar radiation and re-emit the same. Figure 1.2 shows a sketch of the Earth's annual energy balance illustrating the incoming radiation from the sun and the radiated energy from earth surface. The main anthropogenic sources of these gases are: industrial combustion, chemical and petrochemicals, road transport, energy production and landfilling of solid waste [4-8].The concentration of these greenhouse gases continues to increase in the atmosphere and thereby creating a "greenhouse-like" effect by trapping heat from the solar energy, resulting in an increase in the Earth's average temperature. According to International Panel on Climate Change (IPCC), the current trends indicate that Earth's surface temperatures can rise by 3.8 to 11.2 ^{0}F over the next 50 years, primarily due to the greenhouse effect. This increase in the temperature may have profound effects across the globe, like increased sea-levels, severe storms and melting of the large glaciers and icebergs. These changes in the nature would in-turn produce annihilating results in the form of floods, loss of plant and animal life, more frequent droughts, famine, and a greater risk of human casualties.

1. 2. Man-made forcing

1. 2. 1. Emissions of Carbon Dioxide (CO_2)

As shown in the Fig.1.3, concentration of carbon dioxide is increasing in the atmosphere since 1955 [9]. The emission of CO_2 is increasing by almost 3 % per year during the last 50 years [9]. Before 1960, the level of carbon dioxide was about 315 ppm (parts per million) that increased to about 390 ppm (Figure 1.3) by 2005[9]. CO_2 is considered to be a potential greenhouse gas and is responsible for over a half of the enhanced greenhouse effect. Currently, the annual emissions of CO_2 are over 23 billion tons.

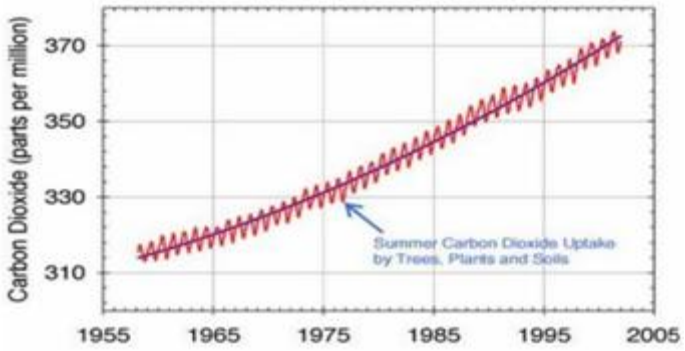

Figure 1.3: The carbon dioxide is increasing from 1955 to 2005[9].

CO_2 enters the atmosphere through the burning of fossil fuels like oil, coal and natural gas, trees, and other chemical reactions. It is estimated that the combustion of fossil fuels may emit upto 63% of CO_2, 24% CH_4 and 10% NO_x. Carbon dioxide emissions therefore are the most important cause of global warming.

1.2.2. Emissions of methane (CH_4): Methane is considered to be the second most contributing greenhouse gas (after CO_2) and is estimated to be responsible for one-fifth of the global warming. CH_4 is released into the atmosphere during the combustion of fossil fuels, landfill sites and agriculture, particularly livestock and rice farming [9].CH_4 is also the predominant constituent of the natural gas. Hence, natural gas can play a significant role as a carbon source for the world's supply of energy and for the production of fuel-based chemicals. For the sustainable energy supply, methane has been playing an important role for many years. When compared to CO_2, global warming potential of methane is almost 150 times higher.

1.2.3. Emissions of nitrous oxides (N_2O)

Nitrous oxide (laughing gas) has been accumulating in the atmosphere since 17th century, and it is a powerful and persistent gas. The source of more than half of N_2O is probably the soil. One molecule of N_2O has the global warming potential equal to 300 molecules of CO_2 [10, 11]. It can stay in the atmosphere for more than 100 years before it is destroyed naturally. At present N_2O concentration in the atmosphere is around 390 ppb. According to IPCC, every year 17 million tons of nitrogen is released into the atmosphere, as N_2O.

1.2.4 Water vapour

Water vapour is one of the most important GHGs and it has two important properties that influence the Earth's radiation [9]. Clouds (water droplets and ice crystals) are reflective and increase the whiteness of the atmosphere, resulting in the reflection of incoming solar radiation. The evaporation of water in the atmosphere increases substantially with rising temperatures that also leads to an increase in the global temperature. Condensation and evaporation processes account for most of the energy transfer between the atmosphere and land via latent heat fluxes. These fluxes do not directly influence temperature but are very important in driving the water cycle [9].

1.2.5 Kyoto protocol

One of the historical events in the environmental history took place in 1997 at the third conference of the parties of the United Nations framework on convention of climate change (UNFCC). Kyoto Protocol was targeted to cut the six main GHG emissions in developed countries. The protocol sets an average GHG reduction target of 5.2% over the period 2008-2012 and uses 1990 as the base year [9]. To retain the developmental efforts, no target was set for developing countries. Kyoto protocol was enforced on February 16th of 2005 [8]. As mentioned, the target was to reduce GHG emissions.

1.3 Can we solve climate change?

The first impression one may have is that we cannot avoid the climate change because we have left it too late. Scientists suggest that in this century climate is changing in many ways and is hostile to humans. The increasing usage of petroleum in the modern society together with decreasing crude oil reserves accelerated the research on the alternative energy sources. Moreover, concerns about the climate change related to increasing global warming are forcing more investment on sustainable energy conversion processes. This stimulated a considerable interest in the area of reduction and/or use of greenhouse gases (GHGs).

Reforming of greenhouse gases to synthesis gas is the most promising route for the utilization of GHGs. Most of these gases emissions are from the combustion of fossil fuels in transportation sectors, power generation, industrial boilers, residential and commercial heating. Several scientific studies have been proposed to develop alternate and renewable technologies to produce energy and electricity. An ideal way of improving combustion processes as well as decreasing noxious emissions is to carryout fuel–air conversion directly into hydrogen and/or synthetic gas (H_2 + CO).

1. 3. 1. Hydrogen - The Flexible Storage for Renewable Energy

The energy systems will have to be cleaner, reliable and efficient. Hydrogen (H_2) that has the potential to satisfy many of our energy needs and also considered to be the cleanest fuel that can replace the fossil fuels. H_2 sales are increasing by 6% annually since 2008 due to increasing demand [11, 12]. Currently the interest in producing H_2 is due to stringent environmental policies, climate change and energy security [11, 12].

1. 3. 2. Syngas (CO+H_2)

While significant efforts have been made to utilize renewable energy sources such as wind and solar radiation, in the near future, liquid fuels may still remain to be essential in transport sector. In this context, syngas, the mixture of hydrogen and carbon monoxide, a key intermediate used as the feedstock during Fischer-Tropsch process (a well-known process for gas-to-liquid-GTL conversion) for the production of liquid fuels, plays an important role [13-18]. Fig.1.4. is a schematic representation of a GTL plant. Natural gas-based plants for GTL are predominant since the cost is about one third to that of a coal-based plants [19].Coal, natural gas, crude oil and biomass are the major sources of syngas.

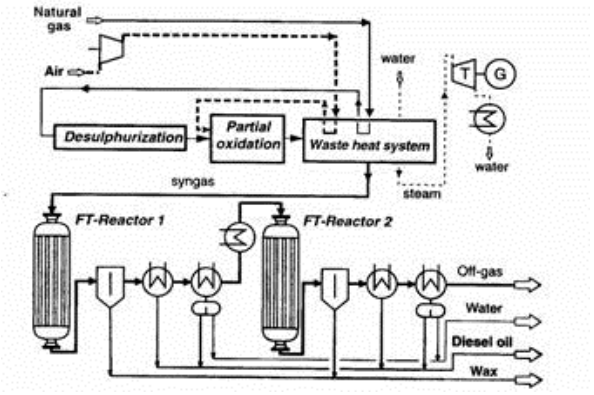

Figure1.4: Conversion of natural gas to diesel oil and wax based on nitrogen rich syngas represented in above flow sheet [16].

1. 4. Technologies for Hydrogen or Syngas Production

The commercial technologies for the production of syngas include steam reforming, partial oxidation, dry reforming and auto-thermal reforming, which will be discussed in the following sections. The oxy-gasification process that produces syngas with different H_2/CO ratios can be coupled with a variety of downstream processes to produce several fuel products (Fig.1.5).

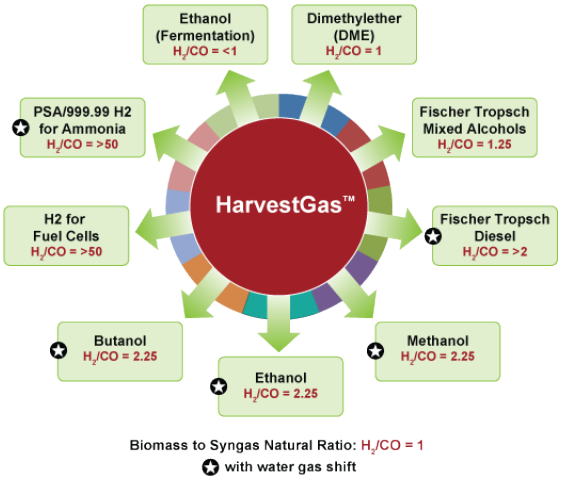

Figure 1.5. Biomass to syngas [9].

1.4.1 Steam reforming

Since methane is the principal component of natural gas, major studies have been conducted on methane reforming (SRM). Flow chart of a steam methane reformer is shown in Fig.1.6, where, carbon monoxide and hydrogen are produced via thermo catalytic conversion of hydrocarbons during the reaction with steam. SRM (Eq-1.1) is an endothermic process (ΔH=-206 kJ/mol) and therefore, requires high temperatures (greater than 1073 K) and usually conducted in the presence of a nickel-based catalyst and excess steam (Steam to carbon ratio of between 2 to 4). This makes the process very expensive [20, 21].

$$CH_4+H_2O \longrightarrow CO+3H_2 \quad (1.1)\ \Delta H= 206\ kJ/mol$$

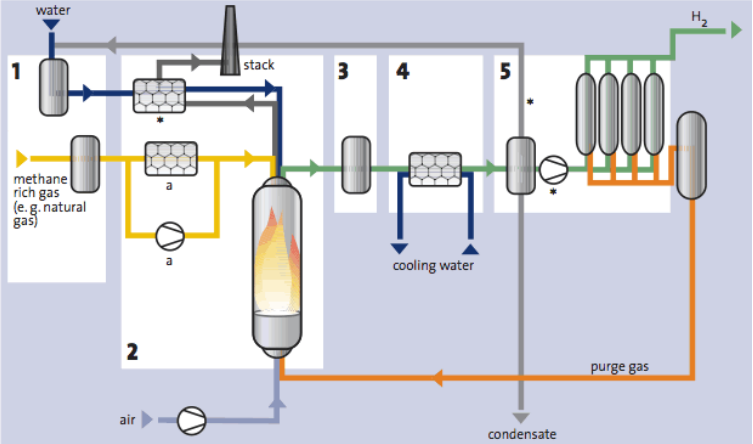

Figure 1.6: (1) Feed Pre-Treatment (2) Reforming & Steam Generation (3) High Temperature Conversion (4) Heat Exchanger Unit (5) Purification Unit [16].

The syngas (H_2 + CO) with H_2/CO of around 2 is considered to be ideal to obtain high-purity hydrogen. However, the use of steam may pose several disadvantages, namely: (1) poor heat transfer (2) corrosion (3) high product H_2/CO ratio of 3 or more (which is not suitable for downstream processing such as Fischer-Tropsch synthesis) and (4) costs in handling excess steam and (5) the occurrence of water-gas shift reaction due to which more amount of CO_2 is produced [14]. Therefore in order to ensure the economic viability, research on alternative processes of methane reforming are warranted.

1.4.2. Partial oxidation

The partial oxidation of methane is a thermo catalytic process, where methane reacts directly with oxygen in the presence of a catalyst to produce syngas [22]. The scheme of the partial oxidation of methane is shown Eq-1.2.

$$CH_4 + \tfrac{1}{2} O_2 \longrightarrow CO + 2H_2 \quad (1.2) \qquad \Delta H = -38 \text{ kJ/mol}$$

Compared to SRM, the partial oxidation of methane is an exothermic process and considered to be economical. But from the practical point of view, it is considered to be expensive because it requires a flow of pure oxygen and also, the process has to be operated below the auto ignition limit of methane to avoid explosion. Moreover, excess oxygen can lead to the formation of CO_2.

1.4.3. Auto-thermal reforming

The combination of two reforming techniques i.e. exothermic partial oxidation and endothermic steam methane reforming has been combined in autothermal reforming of methane (ATR). In ATR process the hydrogen production can be optimised by limiting the water to oxygen feed ratio [23]. Hence, this process

of catalytic reforming of methane involves three reagents (CH_4, H_2O and O_2). The autothermal reforming of methane to syngas was designed to save energy, because the thermal energy required for steam reforming of methane is generated during the partial oxidation of methane [23]. The H_2/CO ratio in autothermal reforming is a function of the mole fraction of the feed gases and typically, the ratio of H_2/CO is in between 1 and 2. On the negative side, an extensive control system is needed for ATRs to ensure robust operation of the fuel processing.

1.4.4. CO_2 (Dry) reforming

When compared to the previous methods, dry reforming is a promising approach, where methane reacts with CO_2 in the presence of a catalyst to yield syngas [24-26]. The scheme of the dry reforming of methane (DRM) reaction is in Eq 1.3.

$$CH_4+CO_2 \longrightarrow 2CO+2H_2 \quad (1.3) \qquad \Delta H = 247 \text{ kJ/mol}$$

This process has the advantage that it consumes two potential greenhouse gases for the production of syngas. On the positive side of dry reforming reaction, the lower H_2/CO ratio (~ 2) is a preferable feedstock for the Fischer-Tropsch synthesis of long-chain hydrocarbons, whereas, on the downside, it is very expensive, because it is more endothermic than steam reforming process and it consumes a great excess amount of energy (247kJ/mol). Another disadvantage of this process is the production of by-products, typically coke, higher hydrocarbons, etc that are deposited on the surface of the catalyst and decrease the activity of the catalyst.

The main challenge for the industrial application of the DRM is the development of an active catalyst that can withstand the poisoning effect of coke. Traditionally, coke deposits during the reaction can be controlled by using a support that favours the dissociation of CO_2 into CO and O, instead of favouring Bouldart reaction (where CO decomposes to give coke).The formation of 'O' species being responsible for the cleaning of the carbon deposited on the surface [19]. To overcome the challenges involved in the dry reforming, two advanced technologies have been developed, especially to take care of the coke deposition, namely the Calcor process and the SPARG (sulphur-passivated reforming) process [27]. The Calcor process is used for the onsite production of high purity CO at chemical manufacturing plants. In this case, dry reforming of methane has been optimised to reduce the H_2 content of the products. The reaction is carried out in an excess CO_2 by passing a desulphurised feed through reformer tubes filled with unspecified catalysts of different activities and shapes at low pressure and high temperature. The SPARG process works on the principle of 'promotion by poisoning'. The active sites on the catalyst that promote carbon nucleation can be 'blocked' by the addition of H_2S to the feed gas. The chemisorption of sulphur on the catalytic sites is thermodynamically favoured over carbon growth. Variation in the CO_2

and steam concentrations in the feed gas allows production of syngas with a low H_2/CO ratio (< 1.8) (Figure 1.6) [17].The overall list of reaction enthalpies in various fuel conversion processes are shown in Table 1.1. Regardless of any kind of reforming process employed, it is important to emphasize that the success on the conversion of greenhouse gases is strongly dependent on the catalytic system used and on the operational conditions such as reaction temperature and feed gas composition etc**.**

Table 1.1

Conversion Process				**Reaction Enthalpy (kJ/mol)**
Steam reforming:	CH_4+H_2O	⟶	$CO+3\ H_2$	$\Delta H = 206$ kJ/mol
Water-gas shift reaction:	$CO+\ H_2O$	⟶	CO_2+H_2	$\Delta H = -41$ kJ/mol
Partial oxidation:	$CH_4+½\ O_2$	⟶	$CO+2\ H_2$	$\Delta H = -38$ kJ/mol
Dry reforming:	CH_4+CO_2	⟶	$2CO+2H_2$	$\Delta H = 247$ kJ/mol
Direct decomposition:	CH_4	⟶	$C(s)+\ 2H_2$	$\Delta H = 76$ kJ/mol

The conventional catalytic technologies have drawbacks and are not environmentally begnin. Even though the catalyst can be selectively poisoned by introducing sulphur or halogen-containing compounds and/or solid carbon adsorption, still dry reforming is far from the practical usage [28]. Moreover, catalyst needs to be activated by heating at high temperature and low flow rates. To overcome all the above difficulties, fuel reforming by unconventional methods such as plasma (nonthermal) technology has been proposed.

1.5. Alternative to traditional catalyst in fuel reforming- Plasma technology

The previously described kinetic limitations associated with reforming technologies often demand higher reaction temperatures than what is necessary. This has led to a major interest in the development of alternative reforming techniques in pursuit of mild reaction conditions, more durable catalysts and reduced energy costs [29-34]. One of such techniques, plasma chemistry, has become a rapidly growing area of scientific endeavour that holds a great promise for practical applications for industrial and medical fields. Plasma is not a new technology to public, as many of the IC circuits used in computers, cell phones, and other modern electronic devices are manufactured by using plasma-enabled chemical processing equipment [32]. The synthetic fibers used in clothing, photomaterials, and advanced packaging

materials are plasma treated. Interestingly, a significant amount of potable water in the world is purified using ozone, derived by plasma technology. The developments in plasma chemistry are enabling tremendous growth in a variety of applications in manufacturing, environmental remediation, and therapeutic and preventive medicine. Plasma reforming systems claim that plasma behaves like a catalyst [29]. Plasma reformers showed the potential for H_2 production from methane both at fuelling stations or on-board vehicles, where the H_2 can be used directly as a feedstock for fuel cells. This would eliminate the need for H_2 storage and transport, as the existing infrastructure would be used to supply natural gas to fuelling stations. In favour of plasma reformers is the low device weight, compactness, rapid response and low cost. However the main drawback of these reformers is their reliance on electrical power to sustain plasma [29].

1.6. Introduction to plasma

1.6.1. History of Plasma Generation:

Plasma is the universal form of matter and often referred to as the fourth state of the matter, generated due to ionization of gases by the application of either electric field, energetic beam or by adiabatic gas compression. Plasma can be simply defined as the collection of charged (electrons, ions) and neutral particles such that the overall electrical charge of the medium is zero. Under these conditions, the gas molecules ionised to form free electrons and ions that make plasma electrically conductive. Naturally occurring plasmas include lightning, fire, sun and the stars, the aurora borealis. More than 99% of the universe is composed of plasma in many forms such as solar corona, nebula and solar wind. Plasma also appears naturally on the earth as aurora and lightning. Aurora appears about 100 kilometres above the earth's surface and mostly towards the poles. The solar radiation interacts with the molecules and atoms in the atmosphere causing them ionized. The earth's magnetic field traps these particles which get denser near the poles and generate aurora. Lightning occurs in storms when accumulated charged particles inside the clouds cause a large potential difference between the clouds and earth. This huge potential difference leads to the formation of discharges between clouds and earth, as shown in Figure 1. 7. This discharge stream consists of accelerated electrons, which cause the air in this path to be ionized, creating a highly conductive plasma path between the clouds and earth [35, 36].

Figure1.7: Examples of naturally generated plasma, sun, aurora and lightening [37]

1.6.2. Industrial/commercial applications of plasmas: Since the first investigation into electrical arcs, plasma is a word that was first described by William Crookes in 1879, the medium created in electrical discharges, later named as plasma by Irving Langmuir, an American chemist and physicist in 1928, mainly due to that the strongly interacting ionized gas has a resemblance to blood plasma coagulation phenomenon [35, 36]. The first industrial application of plasma is the syntheses of ozone (O_3) from O_2 silent discharge, by Siemens in 1850. Due to the diverse nature of plasmas, it has become an important contributor to a wide range of applications and technological developments. Below is a list of many technological applications of plasmas:

Processing:
• Surface Processing
• Nonequilibrium (low pressure)
• Thermal (high pressure)

Volume Processing:
• Flue gas treatment
• Metal recovery
• Waste treatment

Chemical Synthesis:
• Plasma spraying
• Diamond film deposition
• Ceramic powders

Light Sources:
• High intensity discharge lamps
• Low pressure lamps
• Specialty sources

Surface Treatment:
• Ion implantation

Flat-Panel Displays:
• Field-emitter arrays
• Plasma displays

Radiation Processing:
• Water purification
• Plant growth

Switches:
• Electric power
• Pulsed power

Energy Converters:
• MHD converters
• Thermionic energy converters

Medicine:
• Surface treatment
• Instrument sterilization

Isotope Separation

• Hardening
• Welding
• Cutting
• Drilling

Beam Sources

Lasers

Material Analysis

emission control: destruction of volatile organic compounds (VOCs) from diesel exhausts and flue gases, destruction of odorous molecules and many others.

1.7. Types of Plasma:

Plasma can be generated artificially in the laboratory by using different types of plasma reactors. Based on the temperature variation between the constituents of plasma, two main types of plasmas are proposed, namely, (thermal) equilibrium plasmas and (nonthermal) non-equilibrium plasmas.

1.7.1 Thermal and Nonthermal Plasmas:

Plasma-assisted ignition and combustion are driven by thermal and non-thermal mechanisms. The thermal mechanism, in which plasma's contribution to gas heating results in a local temperature rise, exponential acceleration of elementary combustion reactions, chain propagation and ultimately stable combustion. This mechanism is well-known and has one of its earliest applications been the spark ignition in internal combustion engines. The thermal ignition mechanism is not very relevant for applications because, although it is the easiest to organize, it has a high energy cost, since electrical energy from the plasma is spent non-selectively and is distributed in many ways that are irrelevant for ignition and combustion (i.e. heating of the diluent gas). Alternatively, non-thermal plasma (NTP) mechanism for ignition and combustion has been shown to induce reactions as a result of interactions between the active species, such as excited particles and ions. Often, significant fraction of neutral species acquires and store energy internally (through vibrational or electronic excitation) due to collisions between ions and electrons in plasma. This stored energy may be used by the reactants to overcome the activation energy barriers. Additionally, nonthermal ignition mechanism allows plasma energy to be used selectively in the creation of the active species. Most of what is known about the plasma catalysis is related to mechanism related to fuel-lean (or oxygen-rich) ignition/combustion of hydrocarbons. The main characteristics of plasmas are very high energy density (100 W cm^3 to above10 kW cm^3) and the production of large varieties of active species, which lead to numerous industrial applications.

Table 1.2 Subdivision of plasma

Low temperature plasma (LTP)		High temperature plasma (HTP)
Thermal LTP	**Nonthermal LTP**	
$T_e \approx T_i \approx T \leq 2 \times 10^4$ K **e. g., arc plasma at normal pressure**	**$T_i \approx T \approx 300$ K** **$T_i << T_e \leq 10^5$ K** **e. g., low-pressure glow discharge**	**$Ti \approx T_e \geq 10^7$ K** **e. g., fusion plasmas**

Unlike thermal plasmas, nonthermal plasmas (NTPs) or cold plasmas are characterised by multiple temperature gradients between plasma species, where energy is primarily delivered to electrons instead of molecules. This means that the gas remains cold whilst the electrons gain much high energy and temperature (Te), which range from 10,000 K to 100,000 K (1-10 eV). Thus, the heavy particles in the gas discharge have temperatures (T_i) between 300 to 1000 K. (Te>> T_i) and are considered to be cold, whereas, the energetic electrons are responsible for initiating the chemical reactions in the plasma.

1.7.2 Non-thermal plasma generation, properties and applications:

In general, NTP is generated by applying an electric field between the electrodes that creates high energy electrons. These energetic electrons collide with the molecules in the gas and cause them ionized, excited or dissociated. The main reactions occurring in plasma are divided into homogenous and heterogenous reactions. Homogenous reactions occur between species in the gaseous phase as a result of inelastic collisions between electrons and heavy species or collisions between the heavy species; whereas, heterogenous reactions occur between the plasma species and the solid surface that is in contact with the plasma. These typical reactions have been listed in Table 1.3. The heterogeneous reactions are particularly important in the processing of semiconductor materials [38].

Table 1.3 Gas phase reactions involving electrons and heavy species [38]

Name	Reaction	Description
Excitation of atoms or Molecules	$E+A_2 \rightarrow A^{\cdot}_2 + e$ $E+A \rightarrow A^{\cdot} + e$	Leads to electronically excited state of atoms and molecules by energetic electron impact.
De-excitation	$A_2^{\cdot} + e \rightarrow A_2 + e + h\nu$	Electronically excited state emits electromagnetic radiations on returning to the ground state.
Ionization	$e+A_2 \rightarrow A_2^{+} + e$	Energetic electrons ionize neutral species through electron detachment and positively charged particles are formed.

Dissociation	$e+A_2 \rightarrow 2A + e$	Inelastic electron impact with a molecule causes its dissociation without ions.
Dissociative attachment	$e+A_2 \rightarrow A^+ + A + e$	Negative ions are formed when free electrons attach themselves to neutral species.
Dissociative ionization	$E + A_2 \rightarrow A + e$	Negative ions can also be formed by dissociative ionization reactions.
Volume recombination	$e + A + B \rightarrow A + B$	Loss of charged particles from plasma by recombination of oppositely charges.
Penning dissociation	$M^* + A_2 \rightarrow 2A + M$	Collision of energetic metastable species with neutral leads to ionization or dissociation
Penning ionization	$M^* + A \rightarrow A^+ + M + e$	
Charge exchange	$A^+ + B \rightarrow B^+ + A$	Transfer of charge from the incident ion to the target neutral between two identical or dissimilar partners.
Recombination of ions	$A^- + B^+ \rightarrow AB$	Two colliding ions recombine to form a molecule
Electron-ion recombination	$e + M + A^+_2 \rightarrow A_2 + M$	Charge particles are lost from the plasma by recombination of opposite charges.
Ion- ion recombination	$M + A^+ + B^- \rightarrow M + AB$	Ion-ion recombination can take place through three body collisions.
Etching	$C_{solid} + AB \rightarrow A + BC_{vapour}$	Material erosion
Adsorption	$M_g + S \rightarrow M$ $R_g + S \rightarrow R_s$	Molecules or radicals from a plasma come in contact with a surface exposed to the plasma and are adsorbed on surfaces.
Deposition	$AB \rightarrow A + B_{solid}$	Thin film formation
Recombination	$S\text{-}A + A \rightarrow S + A_2$ $S\text{-}R + R_1 \rightarrow M + S$	Atoms or radicals from the plasma can react with the species already adsorbed on the surface to combine and form a compound.
Metastable de-excitation	$A^* + S \rightarrow A$	Excited species on collision with a solid surface return to the ground state.
Sputtering	$S\text{-}B + A^+ \rightarrow S^+ + B + A$	Positive ions accelerated from the plasma towards the surface with sufficient energy can remove an atom from the surface.
Polymerization	$R_g + R_S \rightarrow P_X$ $M_g + R \rightarrow P_X$	Radicals in the plasma can react with radicals adsorbed on the surface and form polymers.

In general, discharge is ignited by applying a high voltage between the electrodes. To sustain plasma, the applied voltage must exceed the breakdown voltage of the gas. When this voltage is reached, gas loses the dielectric properties and turn into a conductor. The minimum voltage required to breakdown a gas to form plasma discharge is called as Paschen's breakdown voltage (Vb). The physical significance of this minimum voltage is that no matter how small the gap or pressure, it is impossible to create discharge at a voltage below V_b [39]. Breakdown voltage was described by the equation:

$$Vb = \frac{a(pd)}{\ln(pd) + b}$$

Where V_b is the breakdown voltage in Volts, *p* is the pressure and *d* is the gap distance in meters. The constants *a* and *b* depend upon the composition of the gas. For air at standard atmospheric pressure of 101 kPa the value of a and b are 436×10^5 V/(atm*m) and 12.8, respectively.

1.8. Schemes of Nonthermal plasma:

Non-thermal plasma can be formed by applying an electric field, which may be a continuous or pulsed direct current (DC) or an alternating current (AC), radio frequencies (kHz – MHz) or microwave frequencies (GHz). Among the NTP reactor configurations investigated for fuel conversion, gliding arc discharge, pulsed corona and dielectric barrier discharge (DBD), spark discharges, and the RF capacitively-coupled plasma (CCP) discharge have been tested. In the following section, a brief introduction of each type of discharge will be presented to highlight its characteristics and benefits for fuel conversion applications.

1.8.1 Corona discharge:

The corona discharge is a self-sustained, weak plasma and low current gas discharge typically found in the regions of non-uniform electric field near sharp edges, thin wires or points [40]. A corona discharge can be generated with a strong, continuous DC electric field or a pulsed DC voltage between two electrodes in which one of the electrodes may be a wire, needle or a sharp edge. Figure 1.8 shows examples of corona discharge reactors, where (a) presents a wire and pipe plasma reactor and (b) represents a wire and plate plasma reactor. Corona discharge can be created by using DC, AC, RF or pulsed voltages. The use of a pulsed power supply reduces the energy consumption by a factor up to five. The discharge mode in a pulsed corona discharge is a streamer, which makes it suitable for pollutant removal. The advantages of pulsed corona discharge are the relatively big discharge gap of about 10 cm which is good for large scale applications and low pressure drop through the reactor. The other advantage

is the low capital cost. Pulsed corona discharge has wide applications for air pollution treatment such as the removal of NOx, SO_2 and VOCs [30, 41-43].

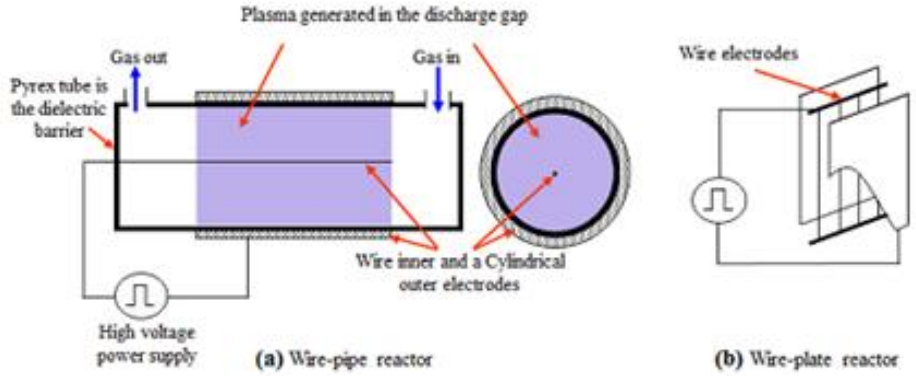

Figure 1.8: Two examples of pulsed corona plasma reactor (a) a wire and pipe reactor and (b) is a wire and plate reactor [37].

1.8.2. Radio frequency (RF) and microwave discharges:

For the selected applications like hydrocarbon cracking, plasma discharges that are held at high frequency are employed. In radio frequency (RF) plasmas, electromagnetic field may generate weakly ionised plasma at low pressures. Up to 100 MHz frequencies were used to generate RF plasmas at low pressures, typically in the range of 1-103Pa [35, 36].

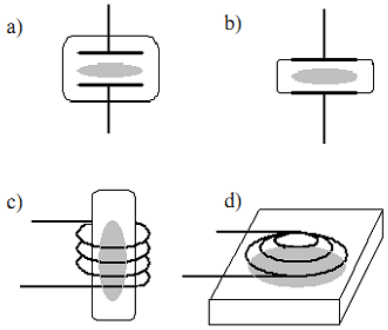

Figure 1.9: Electrode configurations for RF discharges a) CCP with the electrodes inside the gas chamber, b) CCP with the electrodes outside the gas chamber, c) ICP with the discharge located inside an inductive coil and d) ICP with the discharge located adjacent to an inductive coil [38].

For practical applications 13.56 MHz (λ = 22 m) frequency is used. The properties of the RF discharge will change at higher pressures due to increasing collisions, temperature of gas. Radio frequency power can be used to produce two main types of plasma. Firstly, oscillating magnetic field generates inductively coupled plasma (ICPs), and secondly, an oscillating electric field generates capacitive coupled plasma (CCPs). Figure 1.9 show typical reactor designs for each of these configurations.

1.8.3. Dielectric barrier discharges (DBD):

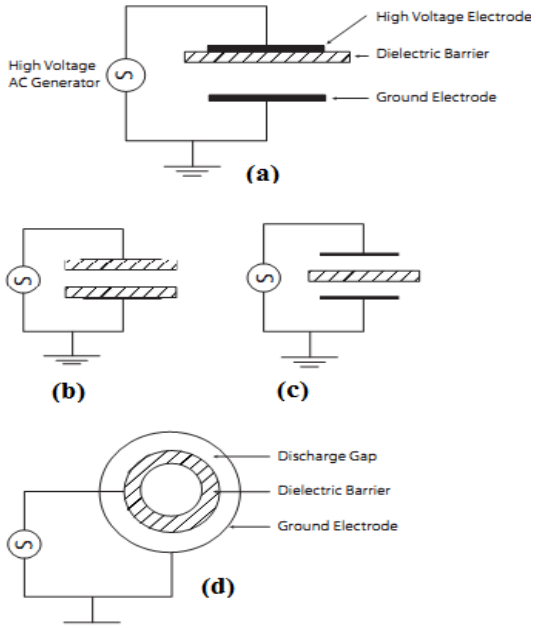

Figure 1.10: Common configuration of the dielectric-barrier discharges (DBDs): planar (a,b,c), cylindrical (d) [42].

The dielectric barrier discharge (DBD) or silent discharge (due to the absence of sparks, which are accompanied by local overheating and the generation of local shock waves and noise) is a commonly used nonthermal plasma discharge that is employed in many industrial processes related to surface treatments such as polymers and textile [39], sterilization, ventilation, ozone generation [41] and air conditioning systems. For the generation of ozone, DBD was first introduced by Siemens in 1857, which determined its direction for many decades [31, 44,45]. Discharge occurs in a number of individual tiny breakdown channels, which are now referred to as microdischarges. The corona-to-spark transition is prevented in a streamer channel due to the presence of a dielectric barrier that stops current and prevents spark formation. The presence of a dielectric barrier precludes DC operation. The operating frequency is in the range 0.05 to 500 kHz. DBDs have numerous applications because they operate at non-equilibrium conditions and atmospheric pressure and can be operated with different gases (in contrast to the pulsed corona), without using sophisticated pulse power supplies. The DBD consists of layered or cylindrical electrode structure, which is located in the current path between metal electrodes that are separated by a thin layer of dielectric material (often made from ceramic, quartz, or glass).

Two specific DBD configurations, planar and cylindrical, are illustrated in Figure1.10. Typical discharge gaps vary from 0.1 mm to several centimetres [46]. The breakdown voltages of these gaps with dielectric barriers are practically the same as those between metal electrodes. DBD is not uniform and consists of numerous microdischarges distributed in the discharge gap, often moving and interacting with

each other. The formation of the DBD microdischarges, their plasma parameters, and interaction between them is an interesting and important subject. In some special cases, particularly in helium gas, DBD can be uniform without any streamers and microdischarges. Special DBD modification, operating with one high-voltage electrode and external conductive object (like a human body for medical applications) as the second electrode, is called a floating-electrode DBD (FE-DBD). DBDs are widely applied for ozone generation, in UV sources, excimer lamps, polymer treatment (particularly to promote wettability, printability, and adhesion), pollution control, exhaust cleaning, biological and medical applications. One of the largest expected DBD applications is related to plasma display panels for large-area flat screens, including plasma TVs.

1.8.3.1 Modifications of DBD: Surface, Packed-Bed, and Ferroelectric Discharges:

Closely related to the DBD are surface discharges, which are generated at dielectric surfaces imbedded by metal electrodes and supplied by either AC or pulsed voltage. The dielectric surface essentially decreases the breakdown voltage because of the significant non-uniformities of the electric field and local overvoltage. In addition, an effective decrease of the breakdown voltage can be reached in the surface discharge configuration (called the sliding discharge) with one electrode located on the dielectric plate and the other one partially wrapped around. The sliding discharge can be uniform on large surfaces with typical linear size over 1 m at voltages around 20 kV. The component of the electric field normal to the dielectric surface plays an important role in generating the pulse periodic sliding discharge, which does not depend essentially on the distance between electrodes along the dielectric.

Surface discharges can be achieved in two different ways: the complete mode/ surface spark and the incomplete mode/ surface corona. The surface corona discharge is ignited at voltages below the critical one and has the current density, limited by the dielectric capacitance. The spark at sliding surface occurs at voltages exceeding the one corresponding to the breakdown voltages. Combination of DBD and sliding surface discharges results the packed-bed discharge configuration. NTP can be generated in a packed bed reactor by applying AC high voltage (about 15-30 kV). Plasma generated in between the voids of dielectric pellets makes the discharge stronger than the original electric field by a factor of 10 to 250 times. Packed-bed DBD consists of an inner electrode connected to a high-voltage AC power supply. The main role of the dielectric barrier is to inhibit direct charge transfer between the two electrodes and serves as a vessel of plasma-chemical reaction.

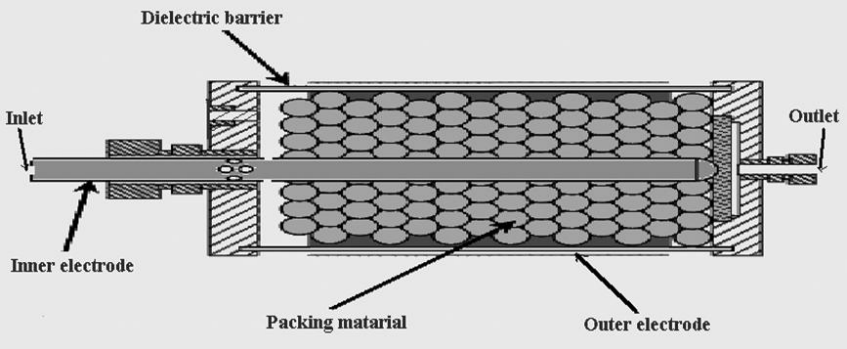

Figure 1.11: Schematic representation of packed-bed DBD reactor

Another special mode of DBD, known as the ferroelectric discharge uses ceramic packing with high dielectric permittivity (ε>1000) as the dielectric barrier (Figure 1.11). $BaTiO_3$ ceramics are the most common materials used in this special mode for the generation of microdischarges. In the absence of an external electric field, these materials can have significant dipole moment. External AC voltage leads to over polarization of the ferroelectric material and generates strong local electric fields on the surface of these materials, which can exceed upto100 V/cm, and stimulates the discharge on the ferroelectric surfaces [47]. The discharge can be arranged, for example, using a packed bed of ferroelectric pellets.

1.9. Plasma as an alternative to traditional catalyst in fuel reforming

Research has been widely focussed on plasma-assisted pyrolysis, steam, dry reforming and partial oxidation of hydrocarbons to synthesis gas [30, 48-52]. Conversion of methane has drawn the attention due to its high abundance in natural gas and also the large database of kinetic information that describes the details of reactions [53-56]. The kinetic limitations of fuel conversion processes often require higher reaction temperatures than what is necessary to produce the same results when the system is at thermodynamic equilibrium. In this context, nonthermal plasma offers advantage of initiating the reactions under ambient conditions. Lower reaction temperatures are desired, not only from the industrial point of view but also for improving energy efficiency. As high temperature operation also leads to undesirable product formation in hydrocarbon reforming systems, NTP processing may be promising. Many modern fuel conversion technologies incorporate the catalysts in order to minimize the activation energy and ultimately to lower the reaction temperatures

1.10. Combined plasma-catalytic reforming for mitigation of greenhouse gases:

In general, it is widely reported that plasma is a non-selective process and it may be difficult to avoid unwanted product formation. Conversion of greenhouse gases into value added products by thermal and catalytic oxidation has low efficiencies due to high energy consumption. However, the greatest

advantage of the NTP processes is the production of highly reactive species, such as ions, radicals, atomic oxygen O, OH radicals, under ambient conditions. However, high energy consumption and unwanted by-products formation are still some of the serious issues for industrial applications of plasma. Hybrid NTP reactor, named plasma-catalysis, appears to be a promising technique to improve the energy efficiency and to achieve a better conversion of hydrocarbons to syngas/Hydrogen. The hybrid reactor can be either single-stage or two-stage system. For the single-stage one, the catalysts/packed materials are placed inside the NTP reactor, commonly known as *in-plasma* catalysis, whereas in a two-stage system, the catalysts are usually placed down-stream to the NTP reactor, also referred to as *post-plasma* catalysis.

In a single stage plasma reactor, due to the introduction of catalysts in plasma discharge, the dielectric properties of the catalyst may be affected that can influence the performance of the system, in addition to other operating parameters such as specific input energy (SIE), feed gas molar ratio, gas temperature, operating pressure and DBD configuration [16]. Various catalysts like nickel/alumina, metal-coated monoliths, zeolites and ceramic materials have been investigated with DBD reactors for a variety of fuel reforming process. For example, Gallon et al. used Ni/Al_2O_3 during plasma dry reforming and found higher reactant conversions, whereas for the same reaction, the use of zeolites improved the selectivity towards lighter hydrocarbon products, particularly $C_2 – C_4$ species. Zeolites are known for their adsorbent properties that allow the species to be adsorbed onto the surface or inside the pore structure to increase the residence time of the species in the plasma discharge. This can lead to increased energy transfer/collisions with the plasma active species. The preferential formation of C_2-C_4 chain hydrocarbons was due to shape selectivity feature of zeolites [49,50]. In general, identification of suitable catalyst combination to improve the selectivity to syngas is far from reality and there is a need to revisit the basic aspects of heterogeneous catalysis for this purpose.

1.11. Motivation and objectives of the proposed work

The previously described challenges associated with the conventional methods of reforming techniques, such as high temperature operation, etc led to a major interest in developing alternative reforming techniques that may operate under ambient conditions. In this context, NTP generates high energy electrons with short residence times that are capable of initiating the chemical reactions under ambient temperature. In particular, depending on the physical characteristics of the plasma produced, three types of processes can be classified: (1) destruction of toxic/harmful materials; (2) modifications of existing materials, e.g., surface treatment for catalyst; (3) creation of new materials. Many researchers reported the applications of NTP for emission control, such as removal of H_2S, N_2O, $CHCl_3$ and CCl_4 etc. However, application of NTP for greenhouse gas conversion to value added products offers advantages like fuel

production, resource utilization and waste minimization. Therefore, this study was focused on the catalytic non-thermal (non-equilibrium) plasma (NTP), generated at atmospheric pressure combined with heterogeneous catalysts for the conversion of three potential greenhouse gases, carbon dioxide (CO_2), nitrous oxide (N_2O) and methane (CH_4). A systematic approach was followed, where the initial study was focused on the direct activation of these gases and at a later stage, co-processing of these gases was addressed. Dry reforming and partial oxidation of methane may complete the scope of the work. The presence of a catalyst in plasma zone may show synergistic effect and expected to improve the performance. To exploit the synergy and to achieve the best selectivity to syngas/methanol at every stage, synthesis, screening and integration of the suitable catalyst with plasma has been carried out.

CHAPTER 2
METHODOLOGY

2.1. Introduction:

The purpose of the present chapter is to describe the experimental setup used for the greenhouse gases conversion by using NTP-DBD reactor. Outline and operational aspects of the various catalyst characterisation techniques will be discussed.

2.2. DBD reactor setup

The experimental set-up is shown in Figure2.1. Briefly, a dielectric barrier discharge configuration was used to create non-thermal plasma (NTP). For this purpose, the outer surface of the quartz tube was wrapped with a copper wire (for 15 cm) that acts as the ground electrode, whereas a stainless steel rod placed at the center of the tube acts as the inner electrode [43, 57-59]. The presence of the dielectric distributes the microdischarges throughout the discharge volume. Inner electrode diameter was varied between 10 to 15 mm to obtain the discharge gap variation between 2.5 to 5 mm and corresponding discharge volume variation between 20.6 to 35.32 cm^3. 10% of the discharge volume was packed with various catalysts placed between quartz wool plugs towards the outlet of the reactor. Plasma reactor was powered by a high voltage AC generator (Yaskawa varispeed F7 AC inverter upto 40 kV and 50 Hz). The voltage (V) and charge (Q) waveforms were recorded with an oscilloscope Tektronix, (TDS 2014B). A 1000:1 high voltage probe (Agilent 34136A HV) was used to measure the voltage across a capacitor of varying capacitance (0.68 to 1.5 µF) connected series to the ground electrode. The voltage across the capacitor multiplied by its capacitance corresponds to the charge accumulated in the reactor. The energetic hot electrons create the reactive species like radicals and ions and initiate the chemical reactions. The plasma input energy per period is equal to the area enclosed by the charge-voltage curve in the V-Q Lissajous.The specific input energy (SIE) was calculated by dividing the power with flow rate of the gas as expressed below,

$$\text{SIE (J/L)} = \text{Power (W)} / \text{gas flow rate (L/Sec)} \qquad (2.1)$$

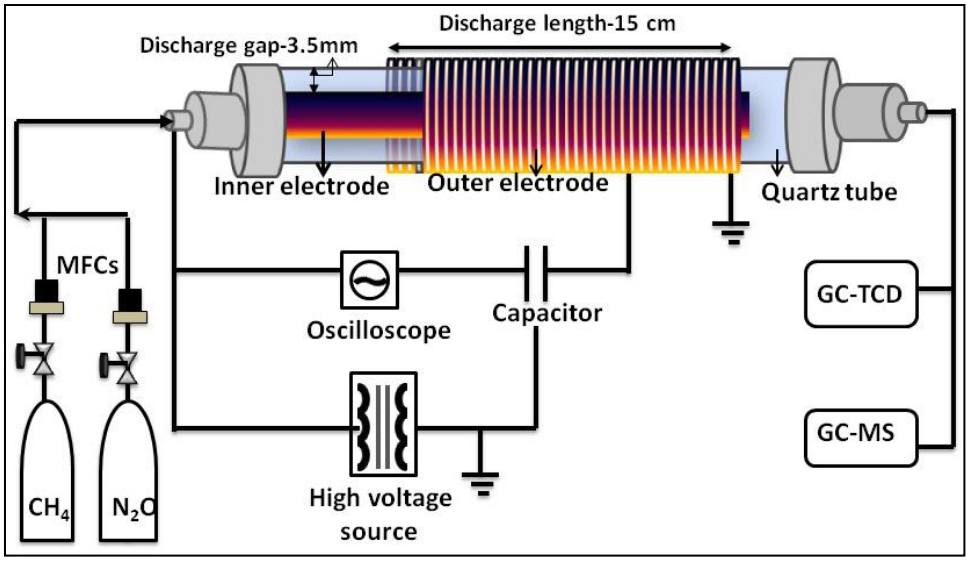

Figure 2.1: Schematic representation of the dielectric barrier discharge reactor with electrical circuit used for measuring the discharge power of a DBD reactor.

2.3. Operating parameters

The operating parameters were divided into three categories like electrical, reactor and gas composition based and is listed in Table 2.1. Based on the type of the reaction, reactant gas diluted with argon (Ar) was introduced into the system through a Teflon tube after regulating through calibrated mass flow controllers.

Table 2.1.List of the operating parameters.

Category	**Item**	**Symbol**	**Unit**
Electrical parameters	Applied voltage (peak value)	V_p	V
	Applied frequency	f	Hz
Reactor parameters	Radius of inner electrode	r_i	Mm
	Ground electrode material		
	Reactor operating temperature	T	K
Gas parameters	Gas composition		Vol %
	Gas flow rate	$\dot{V}$	ml/min

2.3.1. Effect of applied voltage

It has been reported that the number of microdischarges formed inside the discharge volume is proportional to the applied voltage [60, 61]. Also, increasing the voltage increases the density of electrons thereby increasing the collision with gas molecules. This fact is also confirmed by Kogelschatz et al. [62], who reported that the high voltage operations tend to spread and increase the number of microdischarges and thereby chemical reactions.

2.3.2. Effect of discharge gap

The residence time of the gas inside the reactor has been calculated by the following relation, based on which, it may be concluded that increasing discharge gap increases the residence time of the gas.

$$\text{residence time} = \text{discharge volume/flow rate (ml/s)} \qquad (2.2)$$

Where, discharge volume (V) = $\pi(r_2-r_1)^2 \times L$

r_2 = radius of the quartz tube

r_1 = radius of the SS electrode

L = discharge length

Increasing the discharge gap increases the residence time. In addition, the conversion of the reactants may also be effected, mainly due to the influence of residence time on the microdischarge properties. Experiments on ozone formation confirmed that the amount of charge transferred to the microdischarges per half cycle is proportional to the discharge gap [63]. Based on this, it may be inferred that with increasing the discharge gap, the gas breakdown voltage increases, the microdischarge current decreases and therefore, the number of electrons capable of initiating reactions also decreases. Hence, operating the reactor with an optimum discharge gap is needed.

2.4. Power measurement

A voltage-charge (V-Q) Lissajous method was used for the measurement of the power in the present work and the corresponding circuit diagram was shown in Figure 2.1. It requires the measurement of the high voltage (V) and the voltage across a capacitor (V_c). This V_c was used to calculate the charge Q(t) accumulated as a result of current flow through the capacitor. The area of the Lissajous was calculated by following equation (2.3) [47, 60]. The gradients and positions of the lines that make up the Lissajous can

be used to calculate the electrical parameters of the discharge, including the peak-peak charge, charge discharged, transferred charge and capacitance.

$$W = \int_{t_0-T/2}^{t_0+T/2} V(t).C.V_c(t).dt = \int_{t_0-T/2}^{t_0+T/2} V(t).dQ(t) \qquad (2.3)$$

The signals for Q(t) and V(t) over a series of regularly sampled points were measured by a digital oscilloscope (Tektronix, TDS 2014B) and typical wave forms are shown in Figure 2.2, which were used to generate Lissajous figure by plotting the values of charge (Q on Y-axis) against applied voltage (kV on X-axis). The power was measured by calculating the area inside the Lissajous curve and multiplying with the frequency [Equation (2.3)].The specific input energy was further calculated by using Equations 2.4.

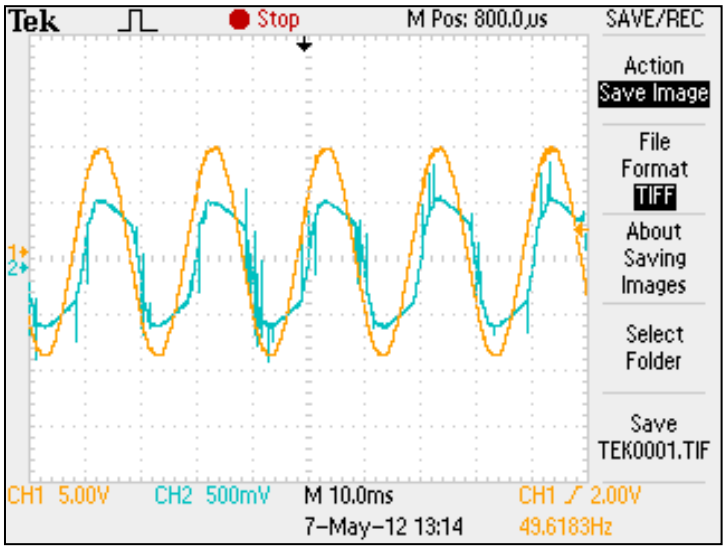

Figure 2.2. Sign waves (voltage and charge) recorded by using digital oscilloscope.

Figure 2.3 is an illustrative example of Lissajous figure, whose area is proportional to the power.

$$P\ [W] = \text{area} \times \text{frequency} \qquad (2.4)$$

$$SIE\left[\frac{kJ}{mol\ H_2}\right] = \frac{Power\left[\frac{J}{s}\right]}{Volume\left[\frac{l}{s}\right]} \times \frac{22.4\left[\frac{l}{mol}\right]}{[c_0]\times X} \times 0.001 \qquad (2.5)$$

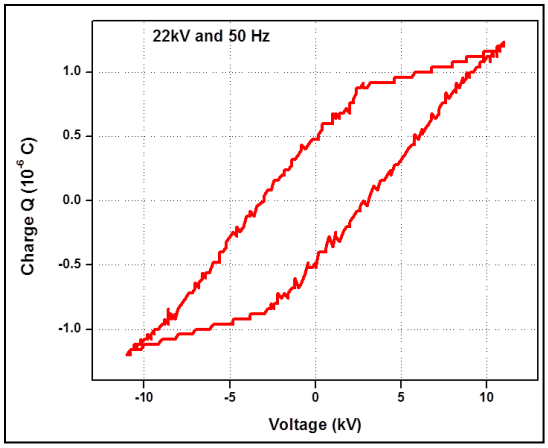

Figure 2.3: V-Q Lissajous model.

2.5. Gas chromatography

Gas chromatography was used to analyse the gas mixture. In general, chromatography refers to the chemical separation of mixtures into pure substances and can be used for both gases and liquids. Essentially, chromatography requires a mobile phase (containing the mixture to be separated) and a stationary phase through which the mobile phase can be eluted. In gas chromatography (GC), the mobile phase is usually an inert carrier gas such as helium or argon. The carrier gas is continuously passed through a column containing the stationary phase. GC columns originally consisted of a tube containing a packing of solid support material with various liquid or solid coatings depending on the type of mixture being separated.

The gas mixture was controlled by a set of mass flow controllers (Aalborg-USA). At the reactor outlet gas analysis was made with an online gas chromatograph (Varian 450-GC), whereas an on-line GC-MS (Thermo Fischer) was used to identify the by-products. The gas chromatograph was equipped with a thermal conductivity detector. Argon (UHP grade) was used as a carrier gas at a flow of 15 ml/min. Separation was made with a packed column (Porapak Q packed column followed by Hysep Q column, with 2 m length each, 1/8" OD and 2.1 mm ID). The mixture to be separated was injected into the column. Different gas species pass through the column at different rates depending on the strength of electrostatic interactions with the mobile and stationary phases present in the column based on their retention times. This causes the gas mixture to become separated into individual components that reach the end of the column and are detected at different times. By measuring the retention time of each species in the column, the component gases can be identified by comparison with chromatograms for known species. Retention times are affected by the gas concentration, flow rate and pressure as well as the column material and temperature. The signal produced by each gas as it reaches the detector results in a

peak on the chromatogram at a residence time that is characteristic for that gas. The peak area is proportional to the gas concentration.

2.5.1. Thermal conductivity detector

The thermal Conductivity Detector (TCD) is a universal detector also called as katherometer, which responds based on the gas ability to transfer heat (Figure 2.4). Heat sensing resistors are connected to form a Wheatstone bridge, so that one or two cells form a bridge. A carrier gas, in general, helium, flows across the resistors that are heated by applying a current. The gas cools the resistor at a constant rate as long as the gas mixture does not change. At the beginning of the analysis, the bridge is equilibrated, but as compounds enter the cell, a change in resistance and imbalance of the bridge is recorded. Two gas sources enter the detector, a reference gas and the reactor effluent. The cells in one diagonal of the bridge form the reference gas signal, and the other side represents the analytical signal from the compounds separated in the column. The voltage across the bridge is measured and the signal is amplified to provide the GC response signal. Electrically heated tungsten-rhenium or platinum wires are typically employed for the analytical filaments [64, 65]. The filaments often have a non-linear response and therefore require individual calibration for each type of gas being analysed.

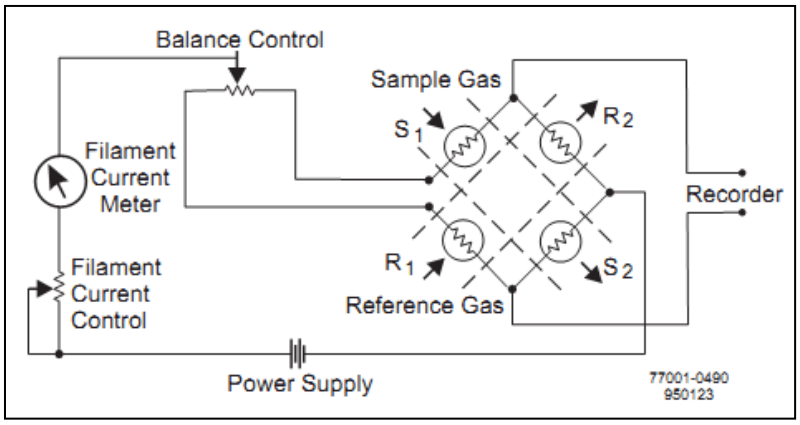

Figure 2.4: TCD Wheatstone bridge Current (taken from [66]).

2.6. Catalyst Characterisation:

2.6.1. Determination of total surface area

The Brunauer-Emmett-Teller (BET) method is the most acceptable procedure for measuring surface area of various materials by physical adsorption of gases at their boiling temperatures. In the present investigation, the BET surface area was determined by N_2 adsorption using a Quantachromeautosorb automated gas sorption analyzer (NOVA 2200e). Prior to analysis, the samples were dried at 593 K in

heating mantles for 12 h under vacuum and flushed with Argon gas for 2 h. All the BET values in this study were measured within the precision of ± 5%. The physisorption of N_2 is utilized to measure the surface area of a solid material. The principle is physisorbed N_2 molecules form a monolayer covering the total area of the material at liquid nitrogen temperature (77K) and this principle is mostly applied within the saturated pressure ($p/p_0 < 0.33$). In principle the amount of adsorbate (nitrogen) required to form a monolayer of molecules over the surface of catalyst is given by the following BET equation.

$$\frac{1}{V[\left(\frac{Po}{P}\right)-1]} = \frac{C-1}{Vm}\left(\frac{P}{Po}\right) + \frac{1}{VmC} \qquad (2.6)$$

Where,

P is the pressure,

P_0 is the saturation vapour pressure,

V_a is the amount of gas adsorbed at the relative pressure P/P_0,

V_m is the monolayer capacity, and

C is a BET constant.

A plot of P/V_a (P_0-P) versus relative pressure of P/P_0 is a straight line with a slope of $(C–1)/(V_mC)$ and intercept of $1/(V_mC)$, respectively. Knowing the slope and the intercept permits calculation of V_m. Subsequently the specific surface area (SA) of the sample can be determined by the following equation. The experiment is performed at 77K and the measured parameter is pressure P. The values P_0, N_A/V_A should be given by standard data and the amount of added gas V is controlled by the instrument. V_m and C are calculated by the computer and are used to calculate surface area (SA). The BET equation:

$$Specific\ surface\ area\left(\frac{m^2}{g}\right) = \frac{V_m\ X\ l\ X\ A_m}{W X\ V_o} \qquad (2.7)$$

Where,

L is the Avogadro's constant (6.023 X 1023 molecules mol^{-1})

A_m is cross sectional area of adsorbate molecule (N_2) is 0.162 nm^2

W is the weight of the sample

V_0 is 22414 mL mol^{-1}

2.7 X-ray diffraction for powder catalysts

Identification of the designed catalysts was done with powder X-ray diffraction (XRD) patterns by PANalytical X'pert pro X-ray diffractometer using Cu K_α (λ = 1.541 Å radiation, 30 mA, 40 kV). X-ray diffraction (XRD) was used to investigate the bulk phases present in the sample. X-rays are energetic enough to penetrate into the material and their wavelengths are of the same order of magnitude as the interatomic distances in solids. Thus X-rays are generated by electrically heated filament, usually tungsten, emits electrons, which are accelerated by a high potential difference (20-40 kV) and allow striking a metal or anode which is water cooled. The anode emits a continuous spectrum of white X-radiation but superimposed on this are sharp, intense X-ray peaks (K_α, K_β) as depicted. The frequency of the K_α and K_β lines are characteristic of the anode metal. The target metals commonly used in X-ray crystallographic studies are copper and molybdenum, which have $K_\alpha$lines at 154.18 pm and 71.07 pm respectively. These lines occur because the bombarding electrons knock out electrons from the innermost K shell (n=1) and this in turn creates vacancies which are filled by electrons descending from the shells lying above [67]. The difference in energy appears as radiation; electrons descending from the L shell (n=2) give the K_α lines and electrons from the M shell (n=3) give the K_β lines. As the atomic number, Z of target increases, the lines shift to shorter wavelength. Normally in X-ray diffraction, monochromatic radiation is required. Usually the K_α line is selected and K_β line is filtered out by using a filter made of a thin metal foil of the element adjacent (Z-1) in the periodic Table; thus nickel effectively filters out the K_β line of copper, and niobium is used for molybdenum. A monochromatic beam of X-rays can also be selected by reflecting the beam from a plane of a single crystal, normally graphite.

A finely grounded crystalline powder contains a very large number of small crystals, known as crystallites, which are oriented randomly to one another. If such a sample is placed in the path of a monochromatic X-ray beam, diffraction occurs from planes that are oriented at the correct angle to fulfil the Bragg condition. For a crystalline solid, the waves are scattered from lattice planes separated by the inter planar distance 'd'. If the scattered waves interfere constructively, they remain in phase since the path length of each wave is equal to an integer multiple of the wavelength. The path difference between two constructive interference waves is given by 2dsinθ, where θ is the scattering angle. Bragg's law, which describes the condition for constructive interference from successive crystallographic planes (h, k, l) of the crystalline lattice is following:

$$n\lambda = 2dSin\Theta \qquad (2.8)$$

A detector is used to record the intensity of the diffracted beams, which are plotted as intensity against 2θ. Thus d (h, k, l) spacing for each reflection can be calculated by the above Braggs lawas shown in Figure 2.5.

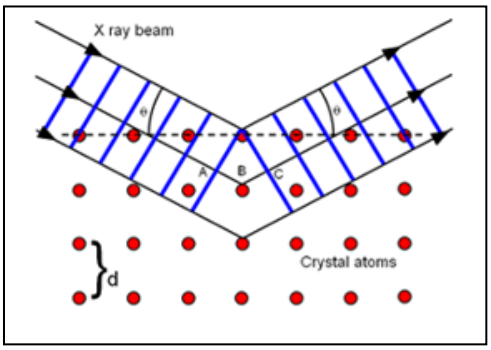

Figure 2.5: Diffraction of X-Rays [20]

2.7.1. Crystallite Size Determination

The average crystallite size in various samples was estimated with the help of Scherrer equation by using the most intense line of the XRD data. Diffraction lines should, in principle, are very narrow; however, when the crystallite size of a polycrystalline material falls below 1000 Å, broadening of the diffraction lines is observed. Instrumental limitations and lattice strain can also cause line broadening. The relation between line broadening and crystallite size for a stress free material, is given by Scherrer's formula:

$$< L >= \frac{K\lambda}{\beta_{hkl} Cos\Theta} \qquad (2.9)$$

Where K is a constant that depends on the definition of β [FWHM] value of a particular hkl plane, in degrees, needs to be converted into radians, since, crystallite size measures in length units] used and the crystal geometry. The constant K varies from 0.98 to 1.39, but because of experimental uncertainties, the constant is often set equal to 1. When β is defined as the integral breadth, <L> is average crystallite size [67].

2.8. Transmission Electron Microscopy

Transmission electron microscopy (TEM) offers a unique advantage of allowing the direct observation of morphology and also provides structural information by lattice imaging and micro diffraction techniques. The technique of high-resolution electron microscopy (HREM) is performed with axial illumination using an objective aperture, which allows several diffracted beams to be combined with the axial transmitted beam to form the image. The HREM images can be directly related with the atomic structure of the material. From the images it is possible to obtain data on the shape and size of particles belonging to supports as well as active phases. Structural information such as symmetry and unit cell parameters of

crystallites, crystal orientations (e.g. epitaxial relationship between support and active phase), and lattice defects can be obtained by electron diffraction and lattice imaging techniques [68, 69]. Specimen preparation is a critical step in electron microscopy because image quality is highly dependent on how the different solid phases are dispersed on the microscope grid and on their thickness. The thickness of solid phases should be less than 50-100 nm to allow sufficient transmittance. Specimens were deposited on 2/3 mm diameter carbon coated copper grids (100−400 mesh) covered with a thin amorphous carbon film. The easiest way is to ultrasonically disperse a few milligram of the powder in a few millilitre of ethanol (EtOH), deposit a drop of the suspension onto a carbon coated grid. In this study, the size and morphology of the nanoparticles were examined by using an FEI model TECNAI G 220 S-Twin TEM instrument.

2.9. Raman Spectroscopy

Raman spectroscopy is one of the useful techniques for characterization of oxides to obtain the information on both metal-oxygen (M-O) bond arrangement and lattice defects [70]. Raman spectra of the fluorite type oxides are dominated by oxygen lattice vibrations, which are sensitive to the crystal symmetry, being thus a potential tool to obtain additional structural information. It can discriminate the different chemical states of the metal oxides, because each state possesses a unique vibrational spectrum that is related to its structure. Therefore, Raman spectroscopy provides the direct information about the structure of the each state. In the present investigation, the Raman spectra were recorded with a Bruker senterra dispersive Raman microscope with laser excitation of wavelength of 532 nm, equipped with a confocal microscope and liquid-nitrogen cooled charge-coupled device (CCD) detector. The emission line at 532 nm from He-Cd laser (Melles Griot Laser) was focused on the sample under the microscope, with the diameter of the analyzed spot being ~1 μm. The time of acquisition was adjusted according to the intensity of the Raman scattering. The wave number values reported from the spectra are accurate to within 1 cm^{-1}. In order to ascertain the homogeneity of the samples, spectra were recorded at various points and compared.

2.10 X-ray Photoelectron Spectroscopy

X-ray photoelectron spectroscopy (XPS), also known as Electron Spectroscopy for Chemical Analysis (ESCA), is a widely used analytical technique for investigating the chemical composition of solid surfaces. XPS is recorded by irradiating a sample with monochromatic X-rays and analysing energy of the electrons emitted. X-rays derived from Mg K_α (1253.6 eV) or Al K_α (1486.6 eV) X-rays are generally used. These X-ray photons have limited penetrating power in a solid, of the order of 1-10 micrometers.

The working principle of XPS is based on photoelectric effect, causing electrons to be emitted from the inner shells of the target. The emitted electrons have kinetic energy (KE) given by:

$$KE = h\upsilon - BE - \varphi s \quad (2.10)$$

Where, hυ is the energy of photon, BE is the binding energy of atomic orbital from which the electron was knocked out, φs is work function of the spectrometer. The binding energy may be regarded as ionization energy of the atom for the particular shell involved. XPS data of the synthesized catalysts were recorded by an Axis Ultra instrument under ultra-high vacuum condition ($<10^{-8}$Torr) and using a monochromatic Al K_α X-ray source (1486.6 eV). Charging of the catalyst samples was corrected by setting the binding energy of the carbon (C 1s) at 284.6 eV. Prior to analysis, the samples were out-gassed in a vacuum oven overnight [71].

2.11. Temperature Programmed Reduction:

Temperature programmed reduction (TPR), temperature programmed oxidation (TPO) and catalytic activity measurements has were carried out in a flow system (Quantachrome autosorb-IQ automated gas sorption Analyzer) equipped with a thermal conductivity detector (TPR-TCD) and mass spectrometer [72, 73]. For TPR measurements, 50mg of the sample was sandwiched between quartz wool plugs in a U-shaped quartz reactor and flushed with He for 30 min. The TPR profiles were obtained by heating the sample from room temperature to the desired temperature (800^{o}C) in 10% H_2 in Ar, (gas flow rates 40 ml / min and heating rate of 10^{o}C/min). The gaseous products were sampled through a fine control leak valve to thermal conductivity detector explained briefly in section 2.5.1 (ASiQ TCD Controller-P/N 00542-7324-1) after passing through a cold tarp to remove H_2O. Quantitative analysis was done by integrating the reduction signal and comparison was made by pre-calibrated signals.

2.12. Temperature Programmed oxidation:

Temperature Programmed oxidation (TPO) measurement carried out in a flow system (Quantachrome autosorb-IQ automated gas sorption Analyzer) connected to mass spectrometer (Pfeiffer PrismaPlus). For TPO measurements, 50mg of the sample was sandwiched between quartz wool plugs in a U-shaped quartz reactor and flushed with He for 60 min. The TPO profiles were obtained by heating the sample from room temperature to the desired temperature (800^{o}C) in 10% O_2 in Ar, (gas flow rates 40 ml / min and heating rate of 10^{o}C/min) and the gaseous products were sampled through a finely controlled leak valve to mass detector shown in Figure 2.6.

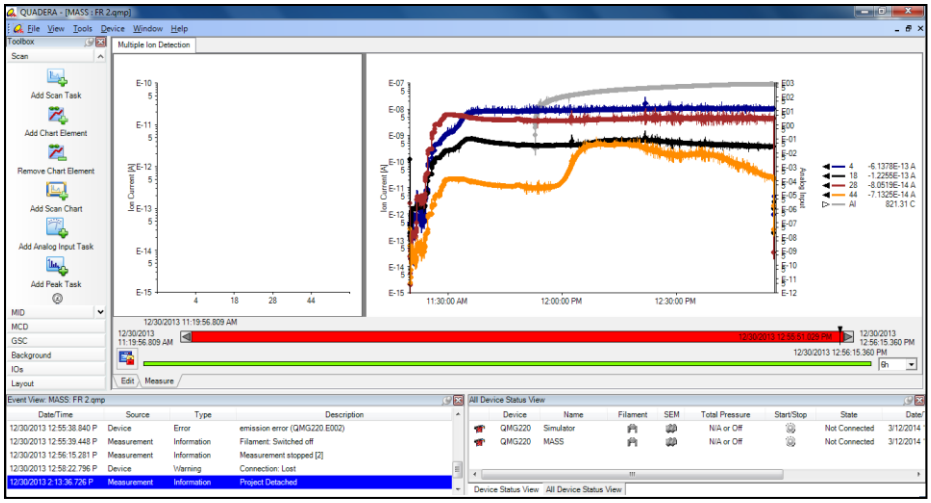

Figure 2.6: Sample picture of evolution of CO_2 during temperature programmed oxidation.

CHAPTER 3
CO_2 reduction to syngas and carbon nanofibres by plasma-assisted *in-situ* decomposition of water

---

3.1. Introduction:

Emission of greenhouse gases (GHCs) by combustion of fossil fuels continues to raise the average global temperature and affecting the environment. The contribution of carbon dioxide (CO_2) towards greenhouse effect is well-established. CO_2 is emitted naturally through the carbon cycle and human activities like burning of the fossil fuels. Short-term solutions such as the mitigation of CO_2bycarbon capture and storage [74, 75] etc., are no longer environmentally acceptable. Syngas (CO, H_2) plays an important role in the energy sector as it can be converted into a number of important energy carriers and liquid fuels in Fischer-Tropsch process [21, 76].For the production of hydrogen, water is advocated as the ideal source. On a large scale, hydrogen is produced by steam reforming of methane (SRM), followed by the water gas shift (WGS) reaction. However, this process is highly endothermic and also emits large amounts of CO_2 into the atmosphere [77]. In this context, several attempts have been made to generate syngas from CO_2, like a two-step thermo chemical cycle [78-81]high-flux solar-driven thermo chemical splitting over a ceria catalyst [82], high-temperature steam/CO_2 co-electrolysis [83-87] and solar assisted CO_2 and H_2O splitting [88]. However, as activation of both the reactants is highly endothermic, these techniques are not promising. It has been confirmed by several researchers that nickel based catalysts are promising for hydrogen and syngas production [50, 62,89-91].

Non-thermal plasma (NTP) generated under ambient conditions is widely used for various applications such as the remediation of air pollutants [49, 62] and depolymerisation of biopolymers [92]. The reforming of CH_4 and CO_2 in DBDs has received little attention in the literature; however, the behaviour of these species in a plasma discharge has fundamental implications for plasma-assisted dry

reforming of methane. However, the Co-processing CO_2 has not yet explored. Hence, it is worthwhile to activate both H_2O and CO_2, especially for energy applications like syngas and methanol formation, etc.

Simultaneous activation of CO_2 and water vapor in a catalytic non-thermal plasma (NTP) dielectric barrier discharge (DBD) reactor operated under ambient conditions has been tested. The discharge volume of the plasma reactor was partially packed (10% volume of the discharge) with a NiO/γ-Al_2O_3 catalyst. Experiments were also performed with an unreduced 33wt% NiO/γ-Al_2O_3 catalyst and with partially reduced NiO/γ-Al_2O_3 catalyst treated under 10% H_2 (Ar) plasma at 22 kV for 3 h, designated as Ni/γ-Al_2O_3.

3.2. Material synthesis and Characterisation:

The NiO/Al_2O_3 catalyst was a commercial catalyst with 33 wt% NiO supplied by Johnson Matthey. Identification of NiO/Al_2O_3, reduced Ni/Al_2O_3 and deposited carbon nano fibres (CNFs) was done by PANalytical X'pert pro X-ray diffractometer using Cu K_α (λ = 1.541 Å radiation, 30 mA, 40 kV). Percentage of metal dispersion and Temperature Programmed Reduction (TPR) of unreduced and reduced NiO/Al_2O_3catalysts was carried out in a flow system (QuantachromeAutosorb-IQ automated gas sorption analyser) equipped with a thermal conductivity detector (TPR-TCD). Temperature programmed oxidation (TPO) of CNFs after HNO_3 treatment have done in a TGA instruments. The morphologies of CNFs deposited on the surface of inner electrode along with the colloidal nano/micro particles were examined by using an FEI model TECNAI G 220 S-Twin TEM instrument. Raman spectra of as produced CNFs were recorded on a Bruker Senterra dispersive Raman microscope with laser excitation of wavelength of 532 nm.

3.3 Experimental Section:

The DBD was generated in a cylindrical quartz tube (Figure 3.1) and had a wall thickness of around 1.5 mm with an inner diameter of 20 mm. Copper wire wrapped around the quartz tube for 150 mm length acted as the outer electrode. A stainless steel (SS-316) rod of 13 mm was used as the inner electrode resulting ina discharge gap was 3.5 mm and a corresponding discharge volume of 27.2 cm^3. A high

voltage (Yaskawa Varispeed F7 AC inverter, AC voltage 0-40 kV and frequency 50-1000 Hz variable) alternating current in the range 14 to 24 kV at 100 Hz frequency was applied to ignite the discharge.

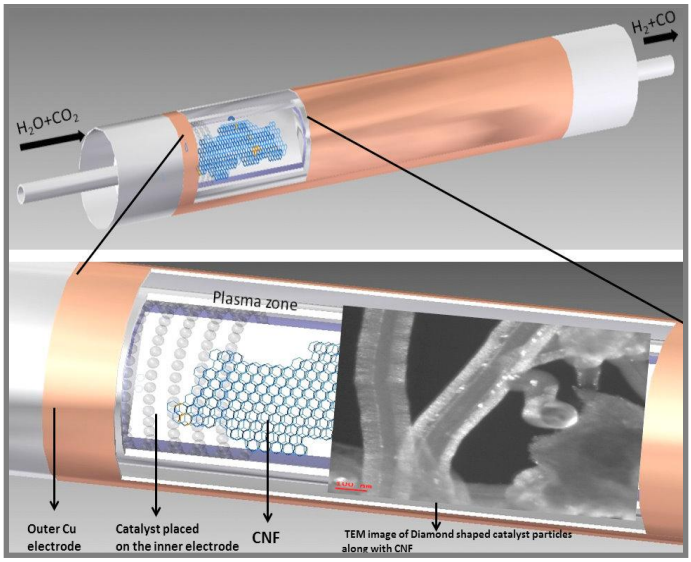

Figure 3.1: Schematic representation of DBD reactor and the formation of CNFs during the progress of the reaction confirmed by TEM.

The voltage (V) and charge (Q) waveforms were recorded with an oscilloscope (Tektronix, TDS 2014B) using a 1000:1 high voltage probe (Agilent 34136A HV). The charge Q was measured by measuring the voltage across the capacitor connected series to the ground electrode. The area of the Lissajous diagram characterizes the energy dissipated in the discharge during one period of the voltage. The average power (W) dissipated in the discharge was calculated by multiplying the area with the frequency. The residence time of the gas inside the reactor has been calculated by the following relation [47].

$$residence\ time\ (Rs.Time) = \frac{Discharge\ volume\ (ml)}{Flow\ rate\ (^{ml}/_{\sec})} \qquad (1)$$

Where, discharge volume (V) = $\pi\ (r_2\text{-}r_1)^2 \times L$

r_2 = radius of the quartz tube

r_1 = radius of SS electrode

L = discharge length

The flow rate of the gas was controlled with mass flow controllers (GFC-17, Aalborg-USA). CO_2 gas was introduced into the reactor through a Teflon tube and its concentration at the outlet was measured with a gas chromatograph (Shimadzu GC-2014) equipped with a TCD detector and a packed column. The conversion at each voltage was measured after 30 minutes. The concentration of hydrogen was confirmed with GC-TCD (Varian 450-GC), whereas a GC-MS (Thermofisher) was used to identify the products formed.CH_4 and CO_2 conversion, CO and H_2 selectivity, H_2/CO ratio and H_2 yield are calculated as given below

$$\mathrm{CO_2\ conversion\ (\%)} = \frac{\mathrm{moles\ of\ CO_2\ in\ inlet} - \mathrm{moles\ of\ CO_2\ outlet}}{\mathrm{moles\ of\ CO_2\ in\ inlet}} \times 100$$

$$\mathrm{H_2\ selectivity\ (\%)} = \frac{\mathrm{moles\ of\ H_2\ produced}}{2 \times \mathrm{moles\ of\ CH_4\ converted}} \times 100$$

$$\mathrm{CO\ selectivity\ (\%)} = \frac{\mathrm{moles\ of\ CO\ produced}}{\mathrm{moles\ of\ CH_4\ converted} + \mathrm{moles\ of\ CO_2\ converted}} \times 100$$

$$\mathrm{H_2/CO\ ratio} = \frac{\mathrm{moles\ of\ H_2\ produced}}{\mathrm{moles\ of\ CO\ produced}}$$

3.4. Results and discussion:

3.4.1. X-Ray diffraction:

The bulk structure of the catalysts was investigated by X-ray powder diffraction. The XRD pattern of the fresh sample of NiO/Al_2O_3 (as supplied) and reduced NiO/Al_2O_3 are presented in Fig. 3.2. The XRD patterns of the fresh NiO/Al_2O_3 confirmed the presence of NiO peaks at 2θ = 37.2°, 43.2°, 62.9°, 75.4° and 79.4°. It can be seen from Fig.3.2 that the sample treated under argon plasma is similar to that of the fresh sample, confirming that the NiO crystal structure remained unchanged during treatment with argon plasma. Figure 3.2 shows the appearance of peaks corresponding to metallic Ni at 2θ = 44.1°, 52.2°and 76.2° [50]. These peaks indicate that the metal reduction has taken place during the treatment in H_2/Ar plasma. The average crystallite size of Ni, as calculated from Scherer equation is around 18-20 nm. The surface area for the reduced and unreduced NiO/Al_2O_3 catalysts is listed in Table 3.1. As seen in Table

3.1, reduced NiO/Al_2O_3 exhibited relatively high specific surface area than unreduced NiO/Al_2O_3. This may be due to high dispersion of Ni nano particles observed in the case of reduced NiO/Al_2O_3. This has confirmed by % of metal dispersion analysis.

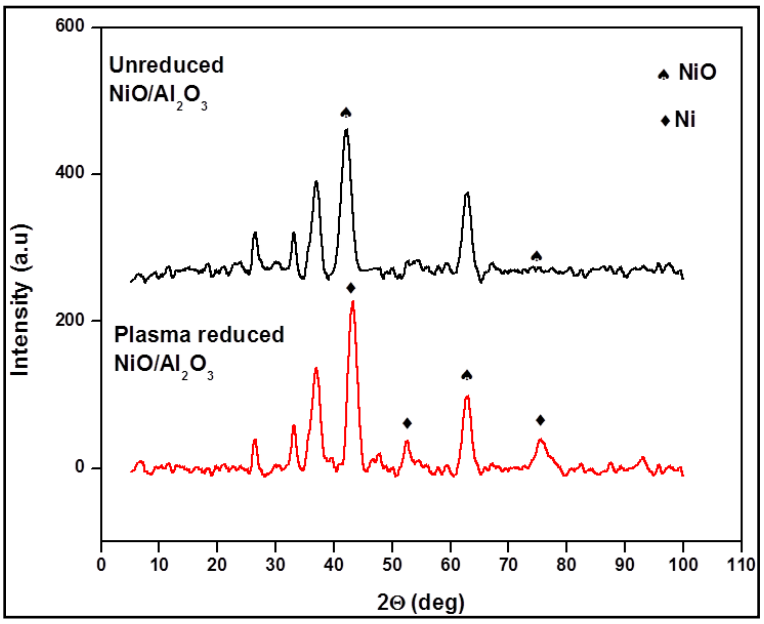

Figure 3.2: XRD patterns of NiO/Al_2O_3 catalyst a) no treatment, b) after H_2 plasma-reduction

3.4.2. Temperature programmed reduction:

Two reduction peaks (Fig. 3.3), for unreduced NiO/Al_2O_3 centered at 450 and 750 °C were observed, which correspond to the reduction of fixed NiO phase on the Al_2O_3 support and $NiAl_2O_4$phase, respectively [50]. The absence of a low temperature reduction peak in plasma reduced NiO/Al_2O_3 suggests that the Ni reduction degree is about roughly 20-30% during plasma treatment.

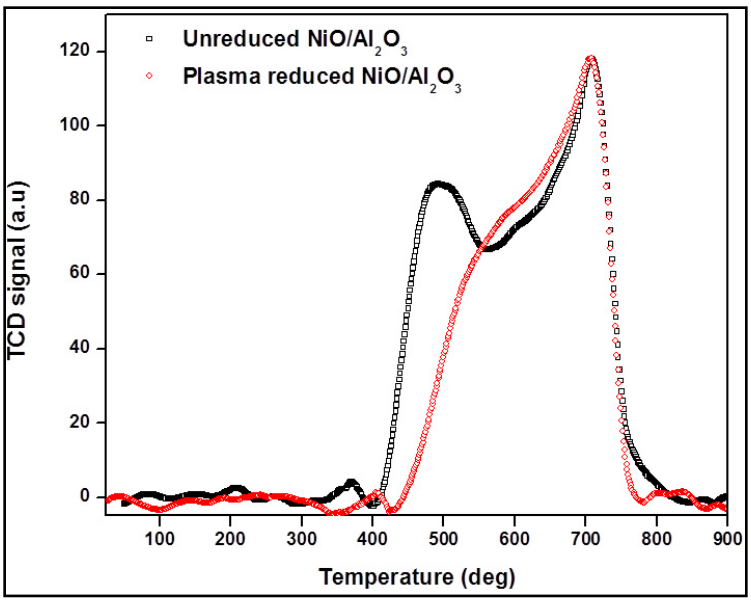

Figure 3.3: TPR spectra of NiO/Al_2O_3catalyst (Black) , H_2 plasma-reduced NiO/Al_2O_3 (Red).

3.4.3. Effect of residence time on CO_2 conversion:

10 vol% of CO_2 is admixed with Ar and then the mixture is humidified by 2.3 vol% by bubbling through water and sent through the DBD reactor. Plasma was created by varying the voltage between 14-24 kV at a 100 Hz. The CO_2 conversion and H_2/CO selectivity were determined as a function of input power (W).

Initial experiments with either only CO_2 or Ar bubbling through water did not show any significant conversion. Interestingly, bubbling CO_2 through water at 303 K resulted in syngas formation. The reason may be that water molecules, due to their lower enthalpy of formation (286 kJ mol^{-1}) than CO_2 (393 kJ mol^{-1}), are activated by plasma and may interact with excited CO_2. Figure 3.4 presents the results on plasma-assisted CO_2 reduction with H_2O as a function of input power varied between 1.6 and 6.5 W for a CO_2 flow rate varied between 20 to 60 ml min^{-1}(STP), corresponding to the gas residence time (RT) variation between 81.6 to 27.2 s, respectively. The high conversion efficiencies at high discharge powers are due to the generation of energetic electrons and ultimately a higher degree of ionisation in the plasma discharge than for the discharge operating at a lower power.

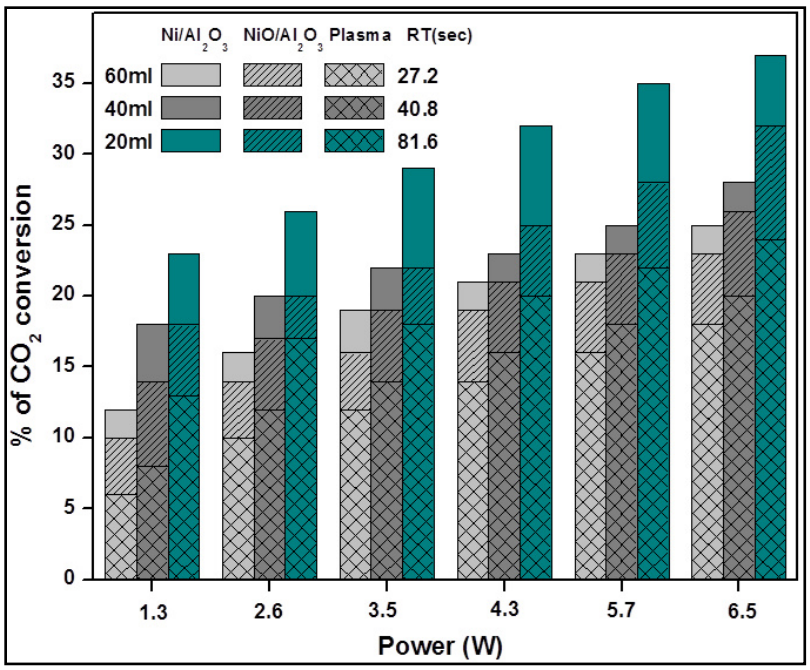

Figure 3.4:CO_2 conversion as a function of power (W) over the plasma, NiO and Ni catalysts (Reaction temperature, 300 K; catalyst weight- 0.50 g and flow rate, 20-60 ml/min.)

3.4.4. Effect of catalyst on CO_2 conversion:

The discharge volume of the plasma reactor was partially packed (10% volume of the discharge) with a NiO/γ-Al_2O_3 catalyst. Experiments were performed with an unreduced 33wt% NiO/γ-Al_2O_3 catalyst and with partially reduced NiO/γ-Al_2O_3 catalyst treated under 10% H_2 (Ar) plasma at 22 kV for 3 h, designated as Ni/γ-Al_2O_3. Figure 3.4 highlights the synergy in the plasma-catalytic CO_2 conversion between plasma, NiO/γ-Al_2O_3 and Ni/γ-Al_2O_3. The reactor with partially reduced catalyst (Ni/γ-Al_2O_3) showed better CO_2 conversion than the unreduced NiO/γ-Al_2O_3 and with no catalyst (plasma alone). This may be due to increase in the surface area and high metal dispersion of reduced NiO/γ-Al_2O_3 (shown in table 3.1. At a fixed residence time of 81.6s (flow rate of 20 ml/min), CO_2 conversion varied between 24 to 36% in case of Ni/γ-$Al_2O_3$for the power variation between 1.3 and 6.5 W, respectively. Under the same experimental conditions, NiO/γ-Al_2O_3 (unreduced) loaded rector showed slightly lower conversion (18 to 28%), whereas, reactor with no-catalyst showed least conversion (12 to 25%). The higher conversion of catalyst packed reactor was due to synergy between plasma excitation of CO_2 molecule and catalytic

action of NiO catalyst. NiO being a basic catalyst facilitates the adsorption of acid CO_2 and improves the conversion [47].

As seen in the Fig.3.4, CO_2 conversion decreased with decreasing the residence time (RT) because the reactant molecules spent less time in the plasma discharge [47]. For example at 81.6 s residence time and 6.5 W, highest conversion achieved with Ni/γ-Al_2O_3 was 36 % that decreased to 24% on decreasing RT to 27.2 s.

Table 3.1: Textural properties obtained by Surface area measurement and % of metal dispersion .

Catalyst	Surface Area (m^2/g)		Metal dispersion(%)
	Before Treatment	After 1hr Treatment	
Unreduced 33wt% NiO/Al_2O_3	180	150	3
Reduced 33wt% NiO/Al_2O_3	200	190	10

3.4.5. Product selectivity:

At 1.3 W power, the selectivity to hydrogen followed the trend NiO/γ-Al_2O_3 (45-40%) > Ni/γ-Al_2O_3 (30-25%) > plasma alone (18-14%). Under the same experimental conditions, Ni/γ-Al_2O showed lowest CO selectivity (72-75 %) than NiO/γ-Al_2O_3(93-97%) and plasma alone (97-99%). These observations highlight that plasma treatment alone is good for syngas formation, but further reduction of CO to methane, NiO catalyst is required.

The syngas ratio (H_2/CO) obtained for a 60 ml min^{-1} flow rate for NiO/γ-Al_2O_3, Ni/γ-Al_2O_3, and plasma varies between 0.95 to 0.45, 0.66 to 0.35 and 0.55 to 0.18, respectively for the input power variation between 1.6 to 6.5W as shown in Fig. 3.5. Hence, it may be concluded that higher flow rates lead to economical syngas production. Carbon balance was lower for NiO/γ-Al_2O_3 and Ni/γ-Al_2O_3 compared to plasma treatment. This was due to the formation of other products like CH_4, CH_3OH, C_2H_2 and allene ($H_2C=C=CH_2$) as identified by GC-MS (not quantified). Partial reduction of NiO to Ni facilitates the conversion of CO into methane, whereas, PCVD of methane takes place only on Ni/γ-Al_2O_3.

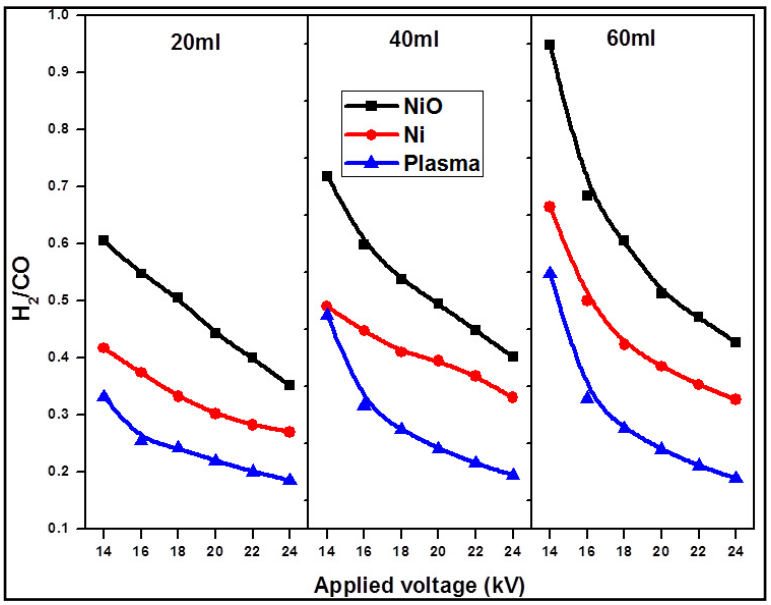

Figure 3.5: Syngas ratio at different residence times under plasma, NiO and Ni catalysts.

A very interesting observation is the formation of carbon nanofibers (CNFs) only with Ni/γ-Al_2O_3 catalyst. The variation in breakdown voltages represented in Lissajous figures at three different conditions (NiO/γ-Al_2O_3, Ni/γ-Al_2O_3 and plasma) is shown in Fig. 3.6. This formation of CNFs on surface of Ni catalyst may increase the breakdown voltage and decreases total capacitance of the dielectric reactor. The morphologies of CNFs deposited on the surface of inner electrode along with the diamond shaped nanoparticles (inset representing the diffraction pattern of Ni particles) trapped in CNFs is shown in Fig. 3.7. The diameter of bulk CNFs is about 110 nm and a hollow tube in the centre has a diameter ~ 60 nm

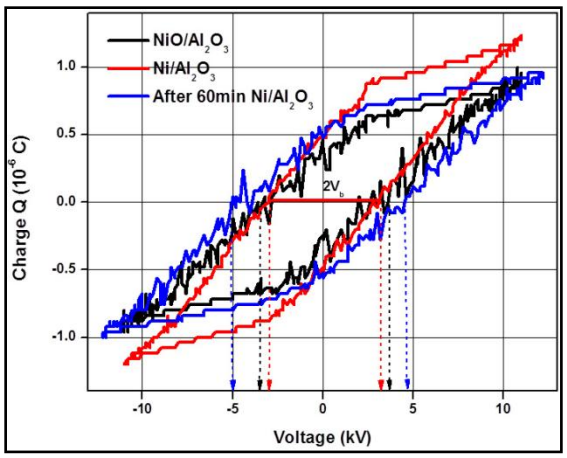

Figure 3.6: V –Q Lissajous diagram at 3.5 mm discharge gap and 50 Hz frequency of CO_2 and H_2O splitting in NiO/Al_2O_3, Ni/Al_2O_3 and Ni/Al_2O_3 after 60 min post reaction at constant capacitance (2.2 µF) and at applied voltage fixed at 22kV.

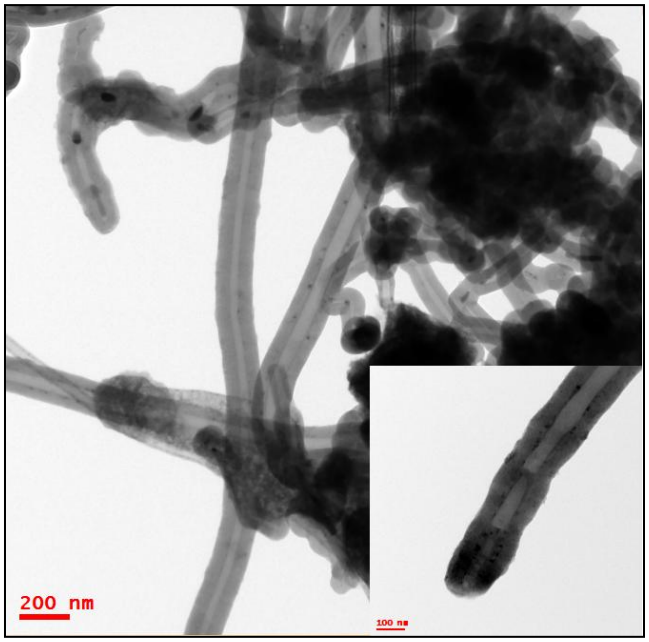

Figure 3.7: The morphologies of CNFs deposited on the surface of inner electrode along with the diamond shaped colloidal nanoparticles.

As seen in Fig. 3.4, plasma treatment showed the lowest syngas selectivity, but did not result in CNF formation. NiO catalyst integration resulted methane formation and Ni catalyst led to the formation of CNFs. Hence, it is reasonable to assume that NiO favours the formation of methane, whereas, Ni nanoparticles are necessary for the plasma-assisted CVD of methane. These observations also ruled out

the possibility of *in-situ* reduction of NiO to Ni by co-generated reducing species (like hydrogen or methane). Hence NiO only showed the formation of methane, but not CNFs.

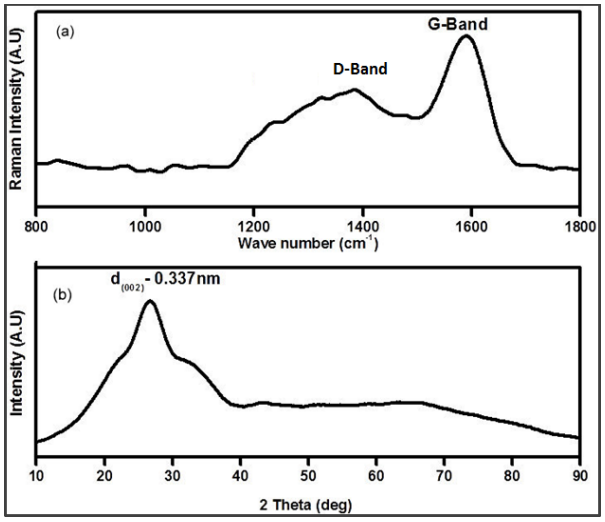

Figure 3.8: (a) Raman and (b) XRD spectra of CNFs deposited on inner electrode

The CNFs deposited were subjected to a verity of characterization techniques. The Raman spectra (Figure 3.8 (a)) confirms the intense G-band at 1580 cm^{-1} due to in-plane displacement of carbon atoms in the hexagonal sheets and D-band centred at 1380 cm^{-1} is due to disordered arrangement. The interlayer spacing of graphite d_{002} plane from XRD (Figure 3.8 (b)) is 3.3542 A˚, which is complemented by the TEM diffraction pattern (3.36 A˚ from Figure 3.7). Therefore, the CNFs formed during the reaction are graphitic in nature. Temperature programmed oxidation of CNFs is shown in Fig. 3.9. It clearly confirms on-set oxidation only at temperature > 800K indicating the stability of CNFs and resulting carbon showed graphitic character [25].

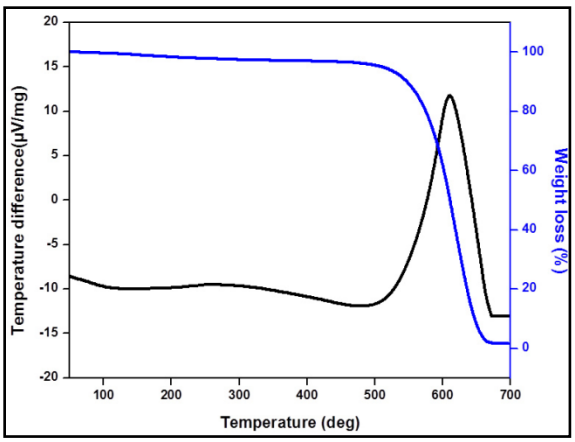

Figure 3.9: Temperature programmed oxidation of CNFs after oxidation (HNO_3) treatment

Physico-chemical (TEM, Raman, XRD and TPO) characterization of CNFs revealed that the CNFs are graphitic in nature. Formation of CNFs may indicate the *in-situ* formation and plasma-assisted chemical vapour deposition (PCVD) of methane. The reduction of CO_2 by in-situ formation of hydrogen during water splitting may produce CH_4 (as confirmed by GC-MS) and PCVD of CH_4 may lead to the formation of CNFs.

3.5. Conclusions:

In conclusion, NTP DBD plasma was successfully demonstrated for simultaneous splitting of water and CO_2 for syngas synthesis. Interesting observation is the co-generation of CNFs, as confirmed by TEM, Raman, XRD and TPO characterisation techniques. CO_2 conversion depends on the residence time. The reactor with partially reduced catalyst ($Ni/\gamma\text{-}Al_2O_3$) showed better CO_2 conversion than the unreduced $NiO/\gamma\text{-}Al_2O_3$ and with no catalyst (plasma alone).

CHAPTER4

Nonthermal plasma assisted CO oxidation by in situ N_2O decomposition

4.1. Introduction

Nitrous oxide (N_2O) is considered to be one of the potential greenhouse gases and is also responsible for stratospheric ozone layer depletion [93, 94]. Consequently, the contribution of N_2O to the greenhouse effect may be significant even at very low concentrations and its global warming potential is 310 times higher than that of CO_2 [93, 94]. N_2O mainly produced by chemical industries during the production of chemicals (adipic acid, nitric acid, acrylonitrile, nylon, caprolactam, etc), combustion processes, road vehicles and medical exhausts etc., and also from soils through the microbial processes of nitrification and denitrification [23, 93-96]. Traditional approaches to control the N_2O emissions in the atmosphere include catalytic decomposition, thermal decomposition, oxidation to NO, wet scrubbing, adsorption, masking and bio filtration, etc. [97-99]. Nevertheless, all these technologies have their own limitations like formation of secondary pollutants like NO_x, poisoning of the catalyst and relatively high process cost. Some of the recent developments for the direct decomposition of N_2O are perovskite hollow fiber membranes,[100] and photocatalytic oxidation [101-107]. In addition to these methods, attention has been focused to nonthermal plasma (NTP) processing, which is characterized by a low degree of ionisation that may facilitate the direct decomposition, even under highly dilute conditions. Studies have been carried out on the decomposition of N_2O by using glow discharges,[108] gliding arc discharge (Glid-Arc),[14, 105] and corona discharge [105].

The present study was aimed at understanding the feasibility of dielectric barrier discharge plasma (DBD) reactor for N_2O decomposition. Various parameters like discharge gap, residence time, input concentration and the effect of packing on the conversion of N_2O were studied. Electrical parameters during the discharge process and the power consumption for N_2O removal were also investigated. As the direct decomposition leads to the formation of atomic oxygen, attempts were made to utilise the atomic oxygen for a probe reaction, CO oxidation ($N_2O + CO \rightarrow N_2 + CO_2$**)** with DBD reactor combined with

various catalysts. Catalytic plasma reactor was optimized and various parameters like applied voltages, flow rate, composition of the gas mixture and catalyst combination.

4.2. Experimental

4.2.1. Catalyst synthesis

Ceria based catalyst (CeO_2 and a series of 15wt% $NiO/Ce_xNi_{1-x}O_{2-\delta}$) were prepared by solution combustion synthesis using citric acid as the fuel. In a typical synthesis, appropriate amounts of $(NH_4)_2Ce(NO_3)_6 \cdot 6H_2O$, $Ni(NO_3)_2$. H_2O and citric acid (oxidant/fuel=1) were dissolved in a minimum amount of distilled water at room temperature and sonicated for 30 min and transferred into an alumina crucible. The alumina crucible was then placed in a preheated furnace maintained at ~450^oC for 5 min. The solution undergoes dehydration and a spark appears at one corner, which spreads throughout the mass yielding a voluminous solid product with grey color. Prior to the activity test, the samples were calcined at 600^0C over 4 hours to remove the carbon content.

4.2.2. Characterization techniques:

Formation and identification of the designed catalysts was done with powder X-ray diffraction (XRD) on PANalytical X'pert pro X-ray diffractometer using Cu K_α (λ = 1.541 Å radiation, 30 mA, 40 kV). Crystallite size was calculated by using the Scherrer'sequation. The textural properties were studied by N_2 adsorption/desorption measurements at liquid nitrogen temperature (at 77K) in a Quantachromeautosorb automated gas sorption analyzer (NOVA 2200e). Before analysis, the samples were degassed at 250^oC for 6 h in vacuum.

The size and morphology of the nanoparticles was examined by using an FEI model TECNAI G 220 S-Twin TEM instrument. To investigate the surface enrichment, the as-prepared samples were immersed in 50% dilute nitric acid solution for 24 h, filtered, and washed with deionized water thoroughly to remove any dissolved nickel oxide in the sample. Inductively coupled plasma (ICP-OES on

a Teledyne prodigy high dispersion) analysis was performed to identify the amount of Ni present on NiCe (5-30 wt%) catalysts before and after enrichment. Ultraviolet-visible (UV-vis) diffuse reflectance spectra in the wavelength range 200-800 nm were performed under ambient conditions using a Shimadzu (UV-3600) spectrophotometer equipped with an integrating sphere $BaSO_4$ reference. Raman spectra of CeO_2 and $NiO/Ce_xNi_{1-x}O_{2-\delta}$ catalysts were recorded on a Bruker senterra dispersive Raman microscope with laser excitation of wavelength of 532 nm.

X-ray photoelectron spectroscopy (XPS) data of the synthesized catalysts were recorded by an Axis Ultra instrument under ultra-high vacuum condition (<10-8 Torr) and using a monochromatic Al Kα radiation (1486.6 eV). Temperature programmed reduction (TPR), temperature programmed decomposition (TPD) and catalytic activity measurements were carried out in a flow system (Quantachrome autosorb-IQ automated gas sorption Analyzer) equipped with a thermal conductivity detector (TPR-TCD). The data was reconfirmed with an in-built mass spectrometer (RGA Prisma plus-200) controlled by the software Quadera and the second confirmation was done with a pre-calibrated ULTRAMAT 23 multi-gas analyser (SIEMENS) that measures CO, CO_2 and O_2. For TPR measurements, a 50 mg of the sample was sandwiched between the quartz wool plugs in a U-shaped quartz reactor and flushed with He for 30 min. The TPR profiles were obtained by heating the sample from room temperature to the desired temperature (600^oC) in 10% H_2 in Ar, (gas flow rates 40 ml / min and heating rate of 10^oC/min) and the gaseous products were sampled through a fine control leak valve to TCD after passing through a cold tarp to remove H_2O. Quantitative analysis was done by integrating the reduction signal and comparison was made by pre-calibrated signals.

4.2.3. Reactor design:

A schematic diagram of the DBD plasma reactor used in the present study is shown in Fig. 4.1 [106]. Briefly, DBD was generated in a cylindrical quartz tube of 23 mm outer diameter and 250 mm length. The outer surface of the quartz tube wrapped with copper wire for 150 mm length acts as an outer

electrode, whereas a stainless steel rod (SS-316) with 10 mm outer diameter placed along the axis of the quartz tube serves as the the inner electrode. The discharge gap was 3.5 mm that corresponds to a discharge volume of 27.2 cm^3. 10% of this active volume between electrodes was packed with catalyst placed in between quartz wool plugs towards the outlet of the reactor. The residence time of the gas inside the reactor zone was calculated by the following equation

Residence time (sec)= Discharge volume (ml)/Flow rate (ml/sec)

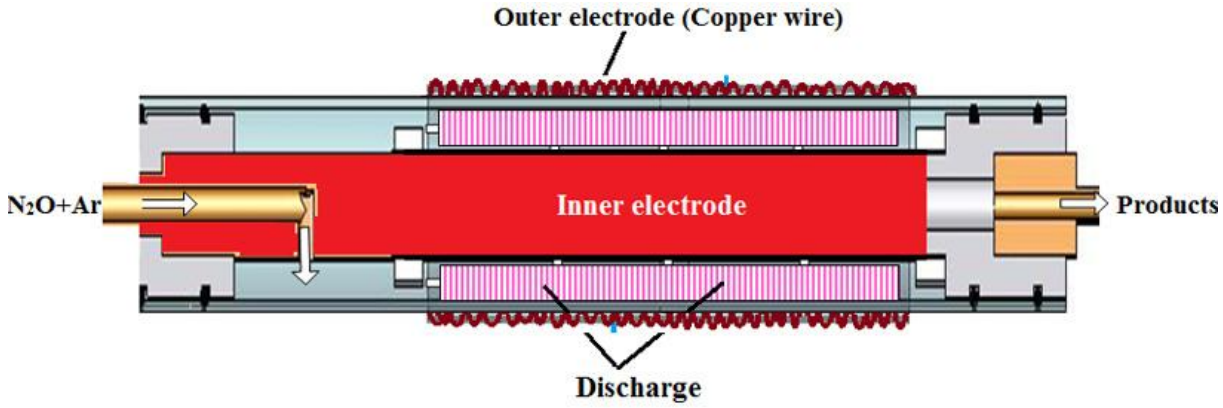

Figure 4.1: Schematic representation of dielectric barrier discharge reactor.

Plasma reactor was powered by a high voltage AC generator (Yaskawa varispeed F7 AC inverter upto 40 kV and 50 Hz). The voltage (V) and charge (Q) waveforms were recorded with an oscilloscope (Tektronix, TDS 2014B) using a 1000:1 high voltage probe (Agilent 34136A HV). The area of the Lissajous diagram characterizes the energy dissipated in the discharge during one period of the voltage. The average power (W) dissipated in the discharge was calculated by multiplying the area with the frequency. The specific input energy (SIE) was calculated by dividing the power with flow rate of the gas as expressed below

SIE (J/L) = Power (W)/ (gas flow rate (L/Sec))

The gas mixture was controlled by a set of mass flow controllers (Aalborg-USA). N_2O (2 vol% diluted in Ar) and CO (5 vol% diluted in Ar) gases were introduced into the reactor and the products were analysed

at the outlet with a Varian-450 gas chromatography equipped with a packed column and a TCD detector. N_2O and CO conversions and CO_2 selectivities were defined as

$$N_2O \text{ conversion} = 100\% \times ([N_2O]_{in} - [N_2O]_{out})/[N_2O]_{in}$$

$$CO \text{ conversion} = 100\% \times ([CO]_{in} - [CO]_{out})/[CO]_{in}$$

$$CO_2 \text{ (selectivity)} = 100\% \times [CO_2]_{out}/ ([CO]_{in} - [CO]_{out})$$

$$O_2 \text{ (selectivity)} = 100\% \times (2[O_2]_{out}/ [N_2O]_{in}-[N_2O]_{out})$$

Where $[N_2O]_{in}$, $[CO]_{in}$, $[O_2]_{in}$, $[N_2O]_{out}$, $[CO]_{out}$, $[CO_2]_{out}$ and $[O_2]_{out}$ stands for concentrations of inlet and outlet gases. Physico-chemical characterization of the packing materials was given in Table 4.1.

4.3. Results and discussion

4.3.1. Direct N_2O decomposition

The dielectric strength of pure N_2O is high (1.24) and requires a high breakdown voltage. Therefore during the present study N_2O is diluted with argon gas that has lower dielectric strength (0.18) to that of N_2O to decrease the dielectric strength of the gas mixture. The sinusoidal waveforms (Figure 4.2a) for applied voltage-charge and Lissajous figures at different applied voltages (6-14 kV, Discharge gap-3.5 mm, and Flow rate-40 ml/min) are presented in Fig.4.2a and Fig.4.2b. As seen in Fig. 4.2b, increasing applied voltage increases the input power.

4.3.1.1. Influence of the discharge gap and residence time on conversion of Nitrous oxide

Figure 4.3a presents the V-Q Lissajous figures for discharge gap length of 2.5, 3.5 and 5 mm (at applied voltage 16 kV), and the corresponding total charge dissipated per half cycle (dQ) is given in Fig. 4.3b. The method for determination of dQ, the total charge per half cycle (The total charge was measured with a non-inductive capacitor) was done as reported [47, 48,61]. Figure 4.3c presents the dependence of N_2O conversion on the discharge gap of the reactor, which was varied between 2.5 and 5 mm and the flow

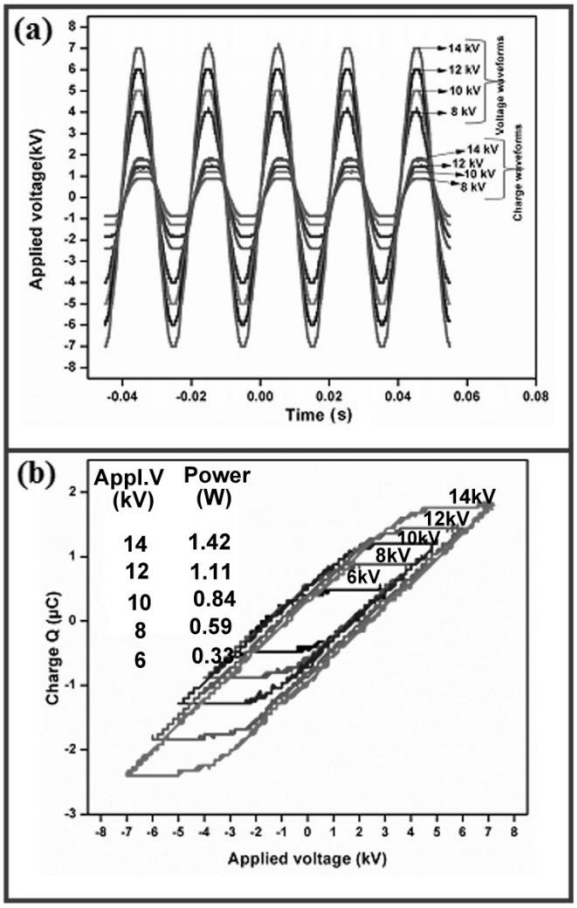

Figure 4.2 (a) Voltage and charge wave forms, and (b) V-Q Lissajous diagrams taken at different applied voltages at 3.5 mm discharge gap and 50 Hz frequency.

rate of the gas was maintained at 40 ml/min. As seen in Fig. 4.3c, increasing power leads to high conversion. At 3.5 mm discharge gap, the reactor showed ~100 % conversion of N_2O even at 1.6 W (SIE-2.4 kJ/L) input power, whereas, the same conversion was achieved at 2.4 W (SIE-3.6kJ/L) and 1.77 W (SIE-2.65 kJ/L) respectively for the reactors with 2.5 and 5 mm gap. As shown in Fig. 4.3b, the dQ at any applied voltage is more for 3.5 mm discharge gap than 5 mm. Even though dQ is more for 2.5 mm, due to the shorter residence time (30.9 sec), the conversion is less than 3.5 mm (RT-40.8 sec). Therefore the highest activity at 3.5 mm may be due to optimum residence time and dQ that may facilitate interaction between excited species and N_2O molecules. The amount of moleculear oxygen and nitrogen formed in

the reaction was quantifiedand it was found that the mass balance oxygen was close to 100%. In order to understand the influence of gas residence time at a fixed discharge gap of 3.5 mm, N_2O flow rate was varied between 20 to 80 ml/min that corresponds to the residence time variation between 81.6 and 20.4s respectively.

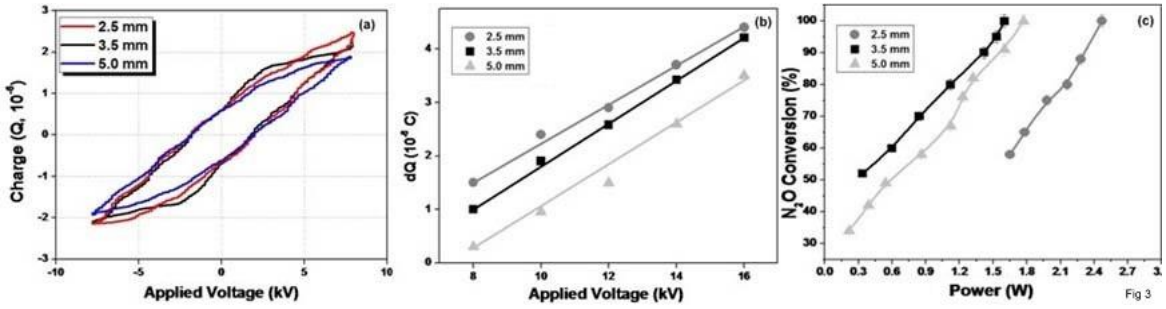

Figure 4.3: (a) The V-Q Lissajous figures (applied voltage 16 kV) (b) The total charge dissipated per half cycle (dQ) as a function of applied voltage and (c) Effect of discharge gap on N_2O conversion at 40 ml/min flow rate for discharge gap length of 2.5, 3.5 and 5 mm.

From Fig. 4.4 it is clear that the optimum flow rate is around 40 to 60 ml/min. The conversion increased with increasing SIE and 100% conversion of N_2O was achieved at 4.2, 2.4, 2.7 and 3.3 kJ/L, respectively for residence time 81.6, 40.8, 27.2 and 20.4s.

4.3.1.2. Effect of N_2O initial concentration on conversion

In order to understand the influence of the initial concentration of N_2O on the performance of the DBD plasma reactor, concentration was varied between 0.5 to 2 vol.% diluted in argon at 40 ml/min and the typical results are presented in Fig.4.5. As seen from the Fig.4.5, at any power, N_2O conversion decreased with increasing concentration and lower concentrations favor better conversion. For example, for 0.5 vol.%N_2O,the conversion was 100 % at 1.28 W (SIE-1.95 kJ/L), the same conversion was achieved at 1.4, 1.5 and 1.6 W (Corresponding SIE- 2.1, 2.3, 2.4 kJ/L), respectively for 1,1.5 and 2 vol% N_2O. It has been reported that the concentration of radicals and excited species formed

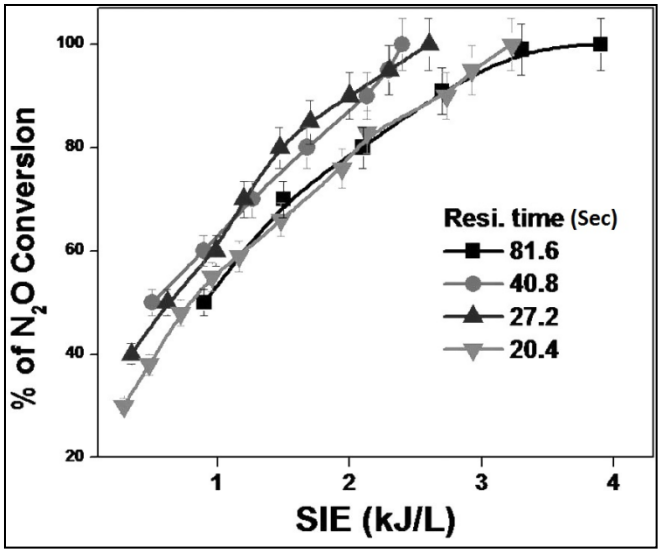

Figure 4.4: Influence of residence time on N_2O conversion as a function of SIE (kJ/L) at 3.5 mm discharge gap and 2 vol% inlet concentrations.

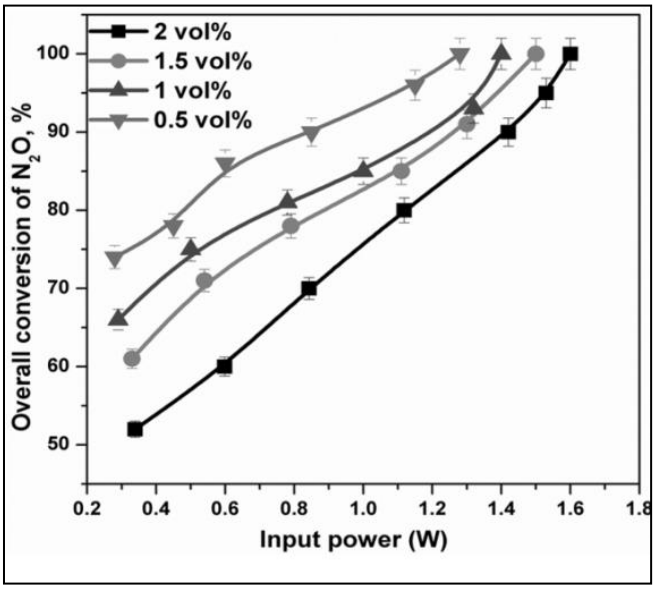

Figure 4.5: Influence of N_2O inlet concentrations (0.5-2 vol.%) on conversion at 40 ml/min flow rate and 3.5 mm discharge gap.

by electron collisions in Ar gas is around 2 to 4 orders of magnitude higher than that of the ions [109].Nonthermal plasma assisted N_2O decomposition in diluted systems may be explained as follows

(1) Direct N_2O decomposition by collision with electrons

$N_2O+e \rightarrow \quad N_2+ 1/2\ O_2$ …….. (1)

(2) N_2O excitation followed by decomposition

$N_2O + e \rightarrow N_2O^*$ …… (2)

$N_2O^* \rightarrow N_2 + 1/2\ O_2$ ……..... (3)

(3) Ar excitation followed by energy transfer between excited Ar to N_2O

$e + Ar \rightarrow Ar(^3P_2) + e$ ……(4)

$Ar(^3P_2) + N_2O \rightarrow Ar + N_2 + O^{\bullet}$ ……..…..(5)

$N_2O + O^{\bullet} \rightarrow N_2 + O_2$ ……..…... (6)

$2O^{\bullet} \rightarrow O_2$ ……..…… (7)

Several researchers [47, 48, 105, 109, 110] reported that when operating in Ar as the balance gas, due to more number of Ar atoms, probability of an electron colliding with Ar is high and the lowest energy excited state Ar ($^3P_2$) may contribute to the dissociation of the target molecule. Also, with increasing Ar gas in the mixture, dielectric strength of gas mixture decreases that also decreases the breakdown voltage of the mixture. Therefore, during the present study, N_2O is diluted with a low dielectric strength gas Ar (0.18) that may lead to Ar ($^3P_2$) active species, which initiate the N_2O decomposition (Eq. 4-7). Similar observation was made by Zhao et al., [109], who confirmed that the main active species formed during electron collision reactions with Ar are the excited states of $Ar(^3P_2)$ and not cations. It is presumed that the mechanism of N_2O decomposition proceeds via excitation of argon followed by transfer of energy between excited Ar species and N_2O molecules leading to N_2O decomposition. As stated earlier, oxygen mass balance was close to 100% which supported this assumption. Therefore excitation of argon and subsequent energy transfer reactions between excited Ar^* and N_2O^* may be dominant during the present study. The highlight of the present work is the direct decomposition of N_2O into N_2 and O_2.

4.3.1.3. Effect of packing

As the conversion was not very impressive, the discharge gap (3.5 mm) between the electrodes was packed with dielectric pellets, such as ceramic pellets (with no porosity), glass beads, and Al_2O_3 (porous) beads. The physical parameters of the packed-bed materials are summarised in Table 4.1 and the

corresponding voltage and charge waveforms are shown in Fig.4.6a. As seen in Fig.4.6a, the charge increases with ceramic materials packed reactor compared to other reactors, which may be due to high dielectric constant of the ceramic materials. As seen in Fig.4.6b (V-Q Lissajous figures for different packing materials), packing with high dielectric constant materials (ceramic beads and glass beads) decreases the breakdown voltage (V_b).The decrease in the charge for Al_2O_3 packed reactor may be due to high surface area and pore size. Figure 4.7 indicates that the charge in the ceramic packed reactor varied between 1.52 and 4.92 µC, respectively in the voltage range between 8 and 16 kV_{pk-pk}, whereas for the glass beads and Al_2O_3packed reactors at the same applied voltages (8 and 16 kV_{pk-pk}), charge varied between 1.4 to 4.42 µC and 0.8 to 3.9 µC and for empty reactor charge varied between 1 and 4.21 µC.The high charge for ceramic packing may be due to enhancement in the number of microdischarges due to its higher dielectric strength than glass beads and empty reactor, whereas, the decrease in the charge for Al_2O_3 packed reactor may be due to porosity and/or change in the discharge behavior as reported earlier [111].

Table 4.1: The physical parameters of the packed-bed materials.

Material	Specific surface area (m^2g^{-1})	dielectric constant	Beads size (mm)
Ceramic beads (ZrO_2)	<0.1	**9.16**	2-3
Glass beads (SiO_2)	<0.1	**4.1**	2-3
Al_2O_3 beads	180	**9.1**	2-3

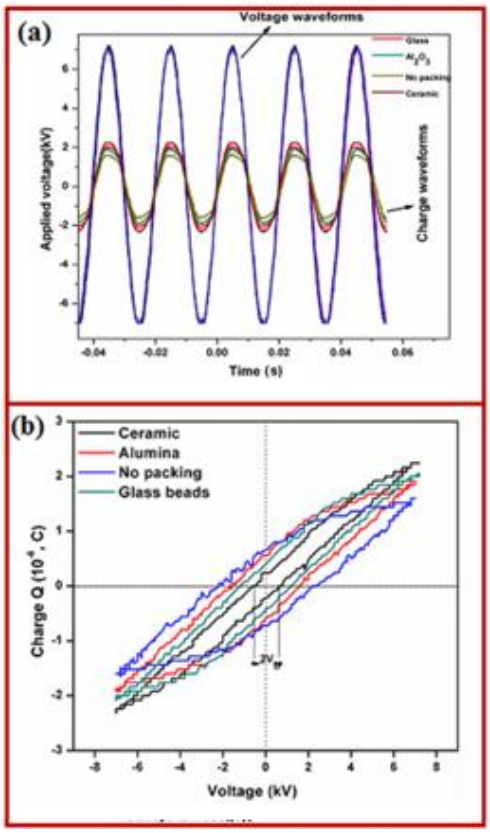

Figure 4.6: Voltage and charge waveforms and V-Q Lissajous diagrams for different dielectric materials packed reactors taken at 14 kV at 3.5 mm discharge gap and 50 Hz frequency.

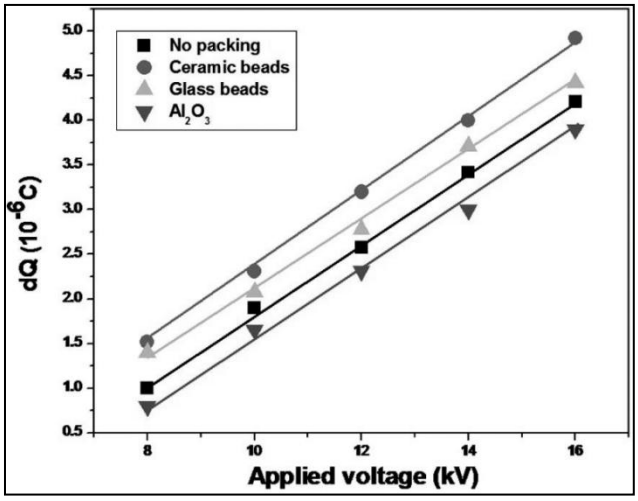

Figure 4.7: Total charge transferred by the microdischarges per half cycle as a function of applied voltage for different dielectric materials packed reactors (for 3.5 mm discharge gap), flowrate was 40 ml/min, 50 Hz frequency.

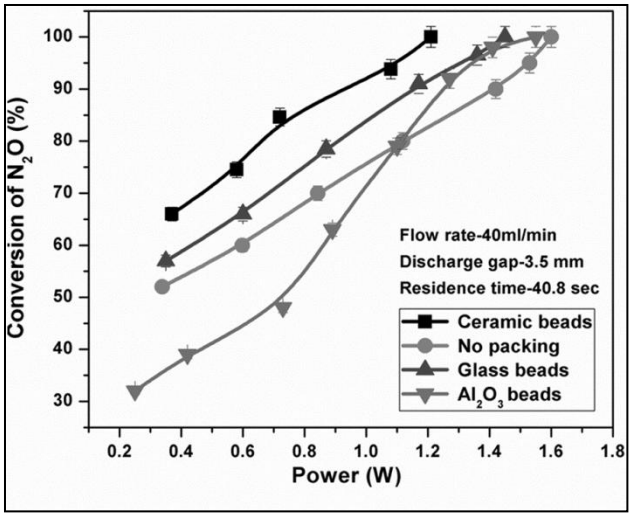

Figure 4.8: Conversion of N_2O as a function of input power (W) for reactors packed with different dielectric materials, Inlet concentration was 2 vol%; discharge gap 3.5 mm, flowrate 40 ml/min and frequency was 50 Hz.

In the case of DBD reactor without any packing, the discharge may be uniform throughout the plasma zone. On changing to a packed bed DBD reactor, due to the ability of the dielectric material to enhance the electric fields at the contact points between the beads, the electric field may be stronger than the applied field that may favour high N_2O conversion. The enhancement in conversion in the case of ceramic beads packed reactor may be due to higher dielectric constant of ceramic beads (9.16) than glass material (4.10). Packing with alumina pellets decreased the N_2O removal efficiency. Even though alumina has high dielectric constant of 9.1, due to high porosity the discharge may not be uniform and only weak filaments can be generated [111]. As seen from the results that the decomposition of N_2O mainly depends on both the concentration of inlet gas (N_2O) and the active species generated in the discharge. As the concentration of N_2O was constant (2 vol.%), the decomposition rate mainly depends on the active species generated. The concentration of the active species generated in the NTP depends on the power dissipation into the microdischarges, which are obviously influenced by the type and properties of the packing material. The rate constant for different materials packed reactors was calculated by using the following equation [112].

$$\ln(C_{in}/C_{out}) = (SIE)\ X\ k + b$$

Where “k” is the decomposition rate constant, “b” is the intercept.

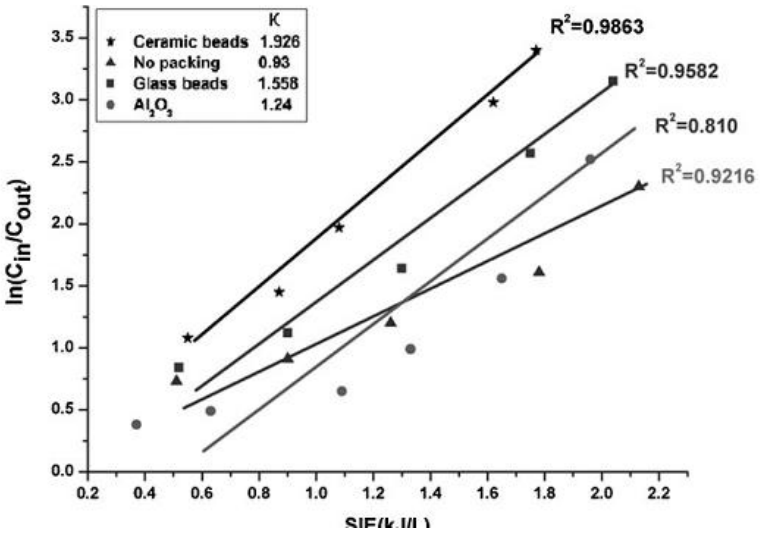

Figure 4.9: Relationship between $\ln(C_{in}/C_{out})$ and input power (linear fits) for different materials packed reactors.

In Fig.4.9, the variation in $\ln(C_{in}/C_{out})$ as a function of input power is shown for different packed bed reactors, which confirms the 'k' value of 1.926, 1.558, 1.24 and 0.93 respectively for ceramic, glass, Al_2O_3 beads and absence of packing, which also supported the best performance of the ceramic beads packed reactor.

4. 3. 2. Simultaneous CO oxidation by in-situ N_2O decomposition

4.3.2.1. Discharge characterizations

It is worth meaning that during the direct decomposition of N_2O, the potentials of N_2O as an oxidant has been wasted due to the recombination of atomic oxygen to molecular oxygen. In order to use N_2O as an oxidant, oxidation of a reducing gas like carbon monoixde (CO) was tested along with N_2O decomposition. For this purpose, the amplitude of the applied voltage was varied between 12 to 22 kV and the corresponding SIE varies between 0.1 to 1.6 kJ/L, respectively. Figure 4.10 presents the conversion of CO and N_2O as a function of SIE varied between 0.1 and 1.9 kJ/L.

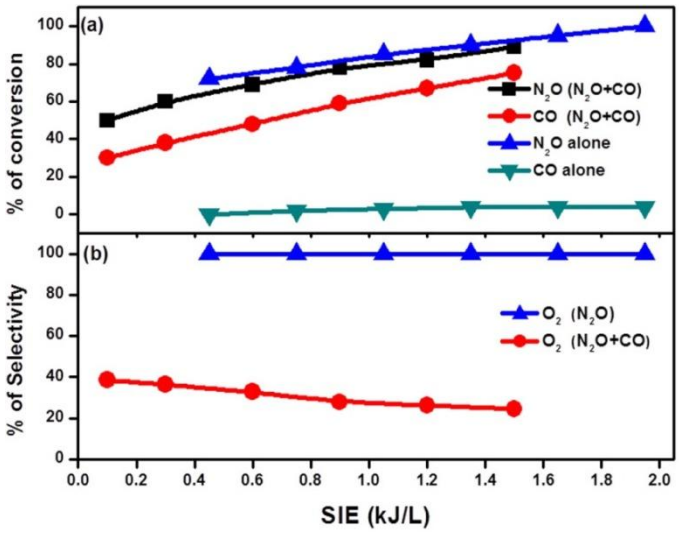

Figure 4.10: CO, N_2O conversions as a function of specific input energy. (a) CO, N_2O conversions comparison with CO conversion in the mixture (N_2O+CO) and N_2O conversion in the mixture (N_2O+CO), (b) O_2 selectivity in the absence of CO (N_2O alone) and in the presence of CO (N_2O+CO).

As seen in Fig. 4.10, direct conversion of CO is very less, which may be due to non-availability of oxidizing atmosphere (Ar is the diluent) and the observed conversion may be due to disproportionation of CO into CO_2 and C (Boudouard reaction) [109], as confirmed by CO_2 formation. Interesting observation is that addition of N_2O significantly improves the CO conversion to CO_2. Increasing SIE leads to higher conversion and among the reactants, N_2O may be decomposed at a lower input energy than CO. At 1.5 kJ/L, for the mixture containing equal amount of CO and N_2O (0.4% each with balance Ar), CO and N_2O conversion was 75 and 88%, respectively. As seen in Fig. 4.10, CO conversion was more in the presence of N_2O which may be explained by electron collision reactions [113-116] as follows:

(1) Under dilute conditions, due to the low concentration of N_2O (2 vol% diluted in Ar) and CO (5 vol% diluted in Ar), it is unlikely that energetic electrons react directly with N_2O or CO. Therefore the probability of an electron colliding with Ar is high and this event leads to the formation of excited Ar($^3P_2$) species [113].

$$e + Ar \rightarrow Ar\,(^3P_2) + e \quad \ldots\ldots\ldots\ldots\ldots\ldots\ (1)$$

(2) Electron collision reactions with CO mainly contribute to CO molecular excitation (Eq. 2) by energy transfer between excited Ar($^3P_2$)and CO followed by dissociation (Eq. 3)

$$Ar(^3P_2) + CO \rightarrow Ar + CO^* \ldots\ldots\ldots\ldots (2)$$

$$2CO^* \rightarrow CO_2 + C \quad \ldots\ldots\ldots\ldots (3)$$

$$e + CO^* \rightarrow C + O^* + e \ldots\ldots\ldots (4)$$

$$2O^* \rightarrow O_2 \ldots\ldots\ldots\ldots (5)$$

Where CO* represents excited CO.

(3) Electron collision reactions with N_2O in plasma

$$Ar\ (^3P_2) + N_2O \rightarrow Ar + N_2 + O^* \ldots\ldots\ldots\ldots (6)$$

$$N_2O + O^* \rightarrow N_2 + O_2 \ldots\ldots\ldots\ldots (7)$$

$$2O^* \rightarrow O_2 \ldots\ldots\ldots\ldots (8)$$

It has been suggested by Zhao et al. [109] and S. Futamura et al. [113] that CO is one of the least reactive species in nonthermal plasma. Hence, CO dissociation by direct electron collision as shown in Eq. 3, 4 is unlikely. These results suggest that the Ar($^3P_2$) do not contribute to direct CO conversion in the absence of N_2O. Under N_2O lean conditions, Ar($^3P_2$) species are either quenched by Ar and CO, or emit radiation [109]. The synergy during CO conversion on addition of N_2O may be due to the formation of atomic oxygen as shown in Eq. 6. In order to ensure this observation, oxygen mass balance during N_2O decomposition was calculated with and without CO as shown in Fig. 4.10(b), which confirms the decrease in oxygen selectivity (from 100% to ~38%) on addition of CO to N_2O. As a result, the rate of CO conversion increases by the addition of N_2O due to the reaction with atomic oxygen as shown in eq. 9.

$$CO^* + O^* \rightarrow CO_2 \ldots\ldots\ldots\ldots (9)$$

During the present study, the CO_2 selectivity was 82% in the presence of N_2O and it was not more than 50% with CO alone.

The overall CO oxidation by N_2O decomposition reaction is given below

$N_2O+CO \rightarrow CO_2+N_2$…… (10)

4.3.2.2. Effect of initial concentration

In order to understand the influence of initial concentration of the reactants on the performance of the DBD reactor, concentrations of N_2O and CO were varied between 0.4 to 1.2 vol. % diluted in argon at a fixed gas residence time of 40.8 s (flow rate of 40 ml/min) and typical results are presented in Fig. 4.11, which presents the activity of the reactor as a function of SIE varied between 0.1 to 2.6 kJ/L. As seen in Fig. 4.11, N_2O and CO conversions increased with increasing SIE and decreased on increasing concentration of both N_2O and CO. Low concentrations favour high conversions.

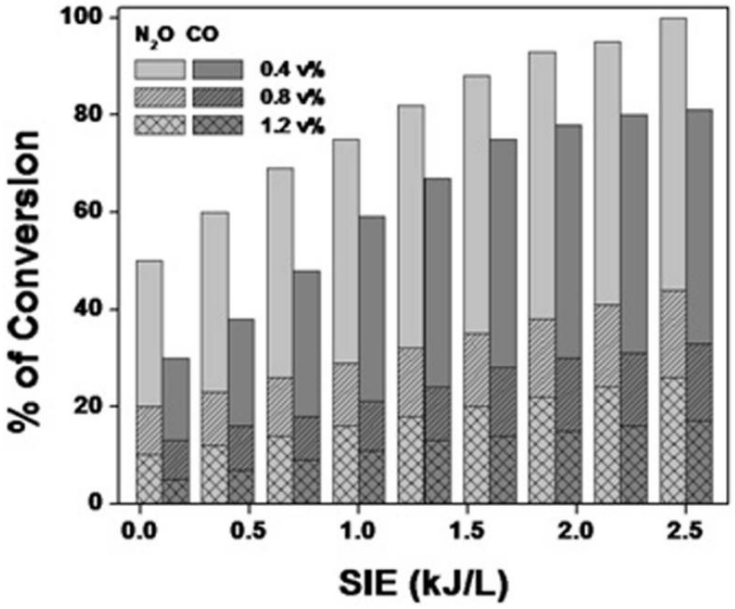

Figure 4.11. Influence of initial concentration (0.4-1.2 vol.%) on CO and N_2O conversions at 40 ml/min flow rate and 3.5 mm discharge gap.

For example at 2.6 kJ/L, N_2O and CO conversion was 100 and 81% respectively for 0.4 vol% each of N_2O and CO. At the same SIE, for 0.8% and 1.2% initial concentrations, N_2O and CO conversion varied only between 43 to 26 % and 33 to 17%, respectively. It may be concluded that low concentrations are preferable, probably due to availability of limited number of active species at any fixed SIE. Interesting observation is that even though mole ratio of the reactants are maintained at 1, CO_2 selectivity decreased with increasing concentration of the reactants and followed the order of 82% (0.4 vol%) > 71% (0.8

vol%) > 65% (1.2 vol%). One of the possibilities for this observation may be that at higher concentrations the recombination of atomic oxygen may be high, which is in agreement with oxygen selectivity that increases at higher concentrations.

4.3.2.3. Effects of gas residence time on N_2O and CO conversion

Influence of gas residence time was studied by varying the flow rate of the gas mixture (3.5 mm discharge gap and 0.4 vol% each of CO and N_2O) between 40 to 120 ml/min that corresponds to residence time variation between 40.8 and 13.6 s, respectively. As seen in Fg. 12, at any fixed residence time, conversion increases with increasing SIE. At 40.8 s and 2.6 kJ/L SIE, conversion of N_2O and CO was 100 and 81%, respectively. Under the same SIE, on decreasing residence time to 20.6 and 13.2 s, conversions decreased to 34, 25 and 21, 15%, respectively for N_2O and CO. Mass balance of the reaction was estimated by measuring the amount of oxygen and nitrogen formed in the reaction and it was close to 100%. The increase in the conversion at lower input concentrations may be due to excitation of the balance gas molecules that may decrease the breakdown voltage of the reaction mixture (Ar+ N_2O+ CO) [116]. It may be concluded that low concentrations and high residence time are preferable for high conversions.

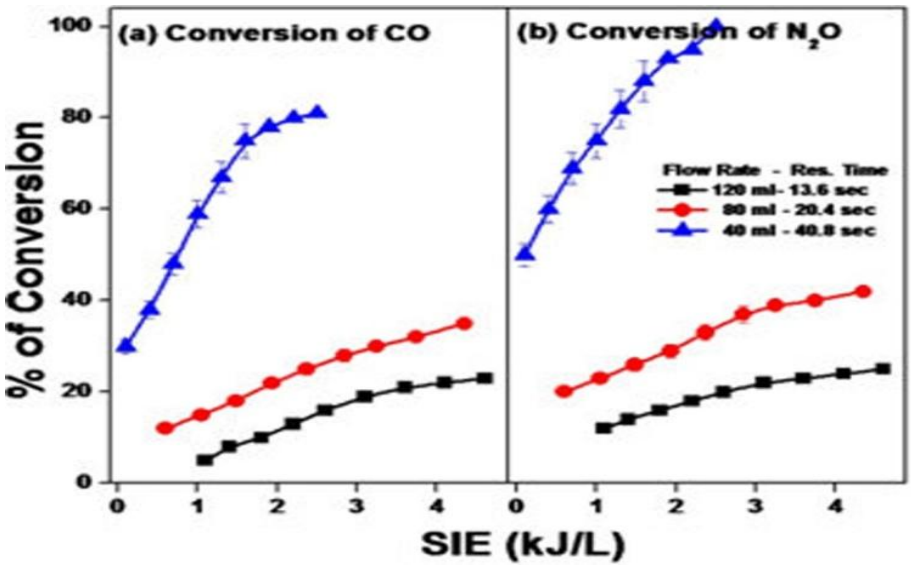

Figure 4.12: Effect of residence time on CO and N_2O for 0.4 vol. % CO and N_2O.

4.3.2.4. Influence of catalyst on CO oxidation by N_2O decomposition

4.3.2.4.1: *XRD:*

Figure 4.13 presents the XRD patterns of the NiO/$Ce_xNi_{1-x}O_{2-\delta}$ catalysts prepared by the solution combustion method. It can be seen in Fig. 4.13 that the diffraction peaks confirm the fluorite structure of CeO_2 [117-120].The absence of NiO diffraction lines for 15% CeNi catalyst indicates the uniform dispersion of NiO on the surface of ceria.

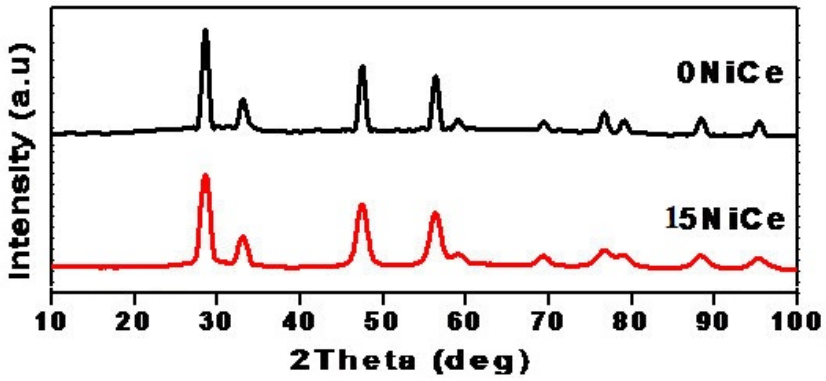

Figure 4.13. Powder XRD patterns showing 15wt % of Ni loaded ceria support and compared with bare CeO_2.

The Ni addition to the CeO_2 structure decreased the lattice parameter, because Ni^{2+} (72 A˚) has a smaller ion radius than Ce^{4+} (92 A˚) and introduces additional lattice perturbation and structural stress and cause extrinsic defects both near grain boundaries and on the plane surface [120]. From the lattice parameter of the mixed oxides one can determine the magnitude of the modification of CeO_2 structure by Ni^{+2} and results are summarized in Table 4.1. The Ni addition also decreased the crystallite size of CeO_2 suggesting dispersion of the NiO [120].

4.3.2.4.2. Nitrogen adsorption: The surface area for the NiO/$Ce_xNi_{1-x}O_{2-\delta}$ catalysts with various Ni loading is listed in Table 4.1. As seen in Table 4.1, 15wt% NiCe sample exhibited specific surface area around 50 m^2/g and CeO_2 support showed slightly higher surface area than the doped samples. The decrease in the surface area for NiCe with Ni doping may be due to penetration of the dispersed metal oxides into the pores of the support and also owing to the formation of specific solid solutions as a result of interaction with the ceria [119].

4.3.2.4.3. TEM:

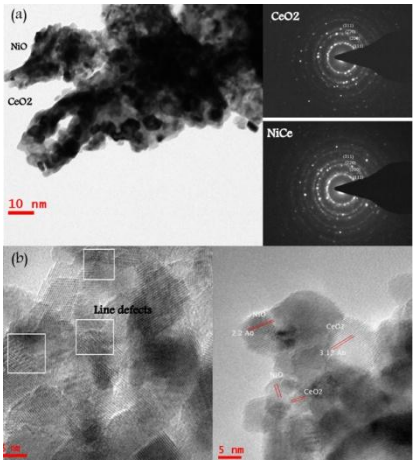

Figure 4.14 (a) TEM and Selected area electron diffraction image (SAED) pattern of 15NiCe, (b) HR-TEM of 15NiCe along with many line defects observed.

The morphology and particle size of 15NiCe catalyst was done with a high resolution TEM technique and typical pictures are shown in Fig. 4.14. Crystallites of approximately 10 nm of ceria were observed for 15NiCe sample. The crystalline size observed by TEM image is consistent with the results from XRD analysis (Table 4.1). In addition, nanoclusters with a size between 3 and 6 nm correspond to NiO distributed on the surface of the ceria particles were also observed. The lattice spacing calculated from HRTEM was 0.310 nm, 0.241 nm coinciding with XRD observation of (111) facets of CeO_2 fluorite and

rock salt NiO crystals (shown in Fig. 4.14b) [120]. In Fig. 4.14(b), many lattice line defects located in the crystalline structure of ceria (represented in squares) was observed.

4.3.2.4.4. UV-Visible spectra:

The optical absorption spectrum of $NiO/Ce_xNi_{1-x}O_{2-\delta}$ is shown in Fig. 4.15, which indicates the presence of $O^{-2} \rightarrow Ce^{+3}$ charge transfer and inter band transition in the wavelength range 260-350 nm [121, 122]. The peak corresponds to 4f→5d transitions of Ce^{3+} are observed for all $NiO/Ce_xNi_{1-x}O_{2-\delta}$ catalysts in between 220–320 nm. Also, a broad absorption edge in the region 480–550 nm due to O_{2p}→Ce_{4f} charge transfer transitions was also observed [123]. Broadening of this band for 15NiCe may be assigned due to the increasing number of surface defects [121]. The red shift for Ni doped ceria is due to surface oxygen vacancies. Hence, UV-Vis spectra of the catalysts confirmed the doping of Ni in CeO_2 matrix.

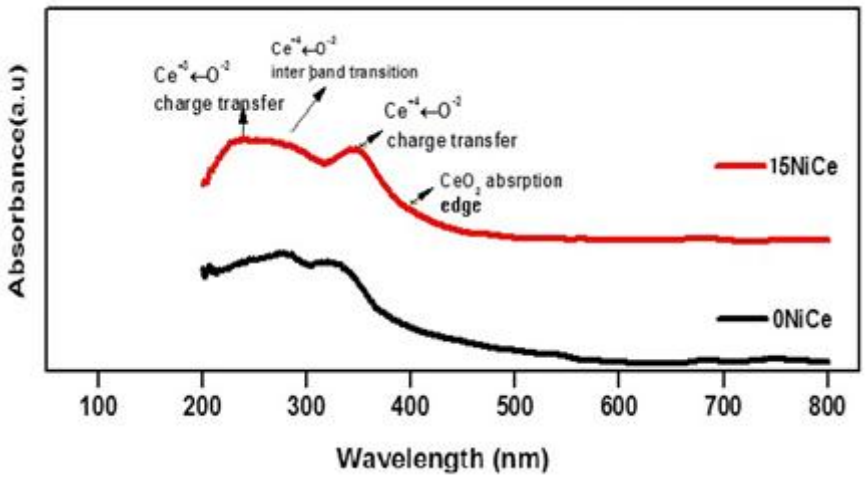

Figure 4.15. UV- Vis DRS spectra of CeO_2 and Ni doped CeO_2

4.3.2.4.5. Raman spectra:

Figure 4.16 presents the Raman spectra of various 15wt% $NiO/Ce_xNi_{1-x}O_{2-\delta}$ catalyst along with CeO_2 support for comparison. Two distinct peaks at 460 and 588 cm^{-1} are observed for $NiO/Ce_xNi_{1-x}O_{2-\delta}$

catalysts. The intense peak at ~460 cm^{-1} was assigned to F_{2g} Raman active interior phonon mode of fluorite structure, [122] whereas, the second band at ca. 588 cm^{-1} is widely reported to be due to defect-induced D band that confirms oxygen vacancies [124]. The formation of $Ce_xNi_{1-x}O_{2-\delta}$ solid solution was confirmed by the shift of Raman peaks to lower wave numbers, as presented by a solid line. The peak area of the bands at 460 and 588 cm^{-1} was calculated as shown in Fig.4.16 (denoted as A_1 and A_2, respectively). The ratio of A_2 / A_1(values included in Table 4.2) may be taken as the concentration of oxygen vacancies in the catalyst [125]. It is seen from Table 4.2 that the A_2 / A_1 value for 15NiCe catalyst (1.5) is highest than CeO_2. It is well-known that the introduction of metal cations to CeO_2 lattice may improve the oxygen vacancy [124].Thus, higher A_2 / A_1 value for 15NiCe catalyst confirms the formation of Ce_{1-x} $Ni_xO_{2-\delta}$ solid solution.

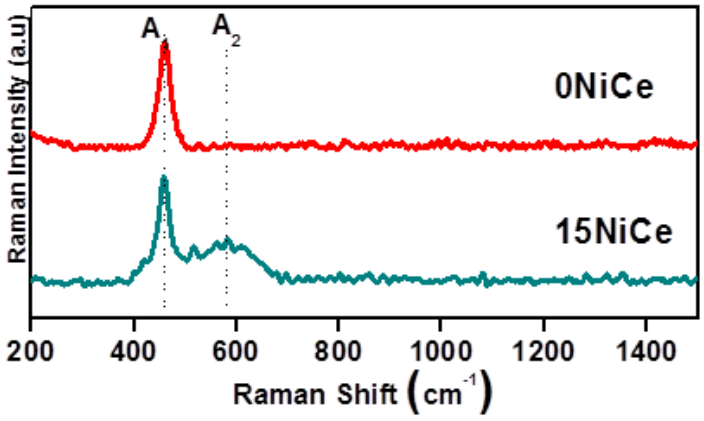

Figure 4.16. Raman spectra of CeO_2 and Ni doped CeO_2

4.3.2.4.*6.* Temperature programmed reduction:

The reducibility of $NiO/Ce_xNi_{1-x}O_{2-\delta}$ catalyst is studied by H2-TPR and results are presented in Fig.4.17, along with CeO_2 support for reference. Typical results in the temperature range 150 to 550^oC indicated three main reduction peaks (denoted as T1, T2, and T3) in 15NiCe sample.

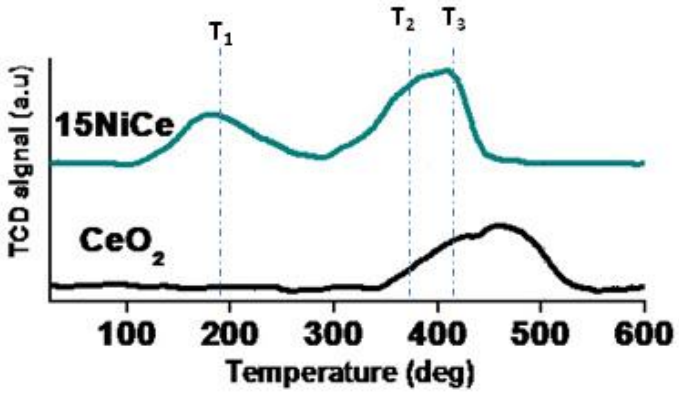

Figure 4.17: TPR spectra of CeO_2 and Ni doped CeO_2

The peak at around 200^0C can be attributed to the replacement of Ce^{4+} by Ni^{2+} into the lattice of CeO_2. Due to this charge imbalance lattice distortion would occur that leads to the formation of Ni–O–Ce solid solution [126]. As a result, reactive oxygen species are generated that may be reduced easily at low temperatures [119, 125-127]. The second reduction peak (T_2) between 350 and 410°C can be attributed to the reduction of strongly interactive NiO species with CeO_2 supports, whereas, the third reduction peak at above 410^oC due to bulk ceria reduction in 15NiCe. The hydrogen consumption and T_{max} during the TPR are given in Table 4.2. As seen in Table 4.2, the highest H_2consumption observed for 586 µmole/g for 15NiCe.

4.3.2.4.7. X-ray photo electron spectroscopy:

The deconvoluted XPS spectra of Ce_{3d}, Ni_{2p} and O_{1s} for 15% Ni catalyst are shown in Fig.4.18(a), (b) and (c) respectively. The Ce_{3d} core level spectra for all the samples were deconvoluted into eight contributions, as shown in Fig.4.17 (a). The four main $3d_{5/2}$ features at 882.7, 884.1, 888.5, and 898.3 eV correspond to V, V',V'' and V''' components, while the $3d_{3/2}$

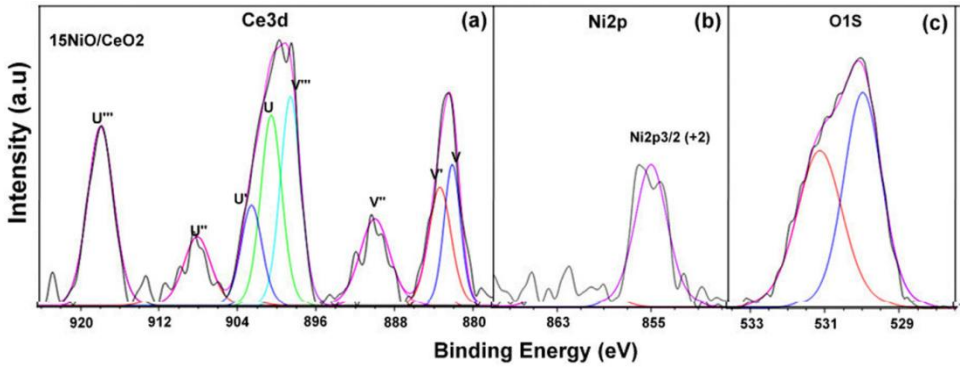

Figure 4.18: Ce3d (a), Ni2p (b), O1s (c) XPS spectra of 15NiCe catalyst

features at 901.3, 903.4, 907.3, and 916.9 eV correspond to U, U',U'' and U''' components, respectively [128]. The presence of the fingerprint U''' satellite peak at about 919.9 eV confirms the Ce^{+4} oxidation state. The relative intensity of well separated U''' from the remaining signals is often used to assess the degree of reduction of Ce ions in the surface region. The appearance of characteristic bands of Ce^{+3} labelled as V' at 884.1 eV and U' at 903.4 eV suggests that both oxidation states Ce^{+4} and Ce^{+3} co-exist on the surfaces of 15NiCe sample [120]. Figure 4.18(b) shows Ni $2p_{3/2}$ for the 15NiCe samples, having a main peak centered at 849.9 eV assigned to Ni^{+2} species. The main XPS peak of Ni^{+2}centered at approximately 849.9 eV relatively higher B.E corresponds to NiO (847.9eV) representing the NiO intimately interacting with the CeO_2 support in consistent with TPR analysis. The XPS spectra of O_{1s} for both catalysts are given in Fig. 4.18(c). The main peak at 529.8 eV has been assigned to the lattice oxygen in ceria and nickel oxides (O^{2-} species). The other peak 531.5 eV assigned for ''O^- ion" deficiencies in the subsurface layer of metal oxides due to the formation of $Ce_{1-x}Ni_xO_{2-\delta}$ solid solution [119].

Table 4.2: Crystallite sizes, lattice parameters and BET Surface Areas, TPR profile, ICP-OES and Raman peak intensity ratio of CeO_2 and 15wt%NiO/$Ce_xNi_{1-x}O_{2-\delta}$

Catalyst	Crystallite Size (nm)		Lattice parameter (A^o)	Surface area (m^2/g)	H_2 consumption values (µmole/g)[a]		NiO content (wt%)[b]		(A_2/A_1)[c]
	CeO_2	NiO			T_1	T_2	Total	Free	
0NiCe	20	-	5.412	60	-	-			0.1
15NiCe	10	-	5.390	47	586 (190°C)	1823 (402°C)	14.6	5	1.4

a H_2 consumption values calculated by integrating the reduction signal and comparison was made by pre-calibrated signals.
b Quantified the amount of Ni present on 15% NiCe catalyst before and after enrichment.

c The peak area of the bands at 460 (A_1) and 588 (A_2)cm^{-1} was calculated from Raman spectra.

4.3.2.4.8. Catalytic DBD plasma reactor for CO oxidation by in-situ N_2O decomposition:

Figure 4.19 presents the performance of plasma reactor on addition of CeO_2 and NiO/CeO_2 catalyst during the conversion of 0.4 vol% each of N_2O and CO for SIE variation between 0.1 and 1.6 kJ/L at a fixed residence time of 40.8 s (40 ml/min flow rate). NTP reactor was intigreted with 0.5 g catalyst flakes in a packed bed configuration. Interesting observation is that addition of the catalyst increases the conversion of reactants as shown in Fig. 4.19. It can be seen in Fig. 4.19 that at 1.6 kJ/L,NiO/CeO_2 catalyst exhibits 100 and 96% conversion of N_2O and CO and close to 5% oxygen selectivity was detected (Fig. 4.20). Under the same experimental conditions, plasma reactor alone showed only 88 and 75% respectively for N_2O and CO (27.5% O_2 selectivity). Whereas, plasma combined only with CeO_2 showed slightly better conversion of 92 and 87% respectively for N_2O and CO (11.5% O_2 selectivity).

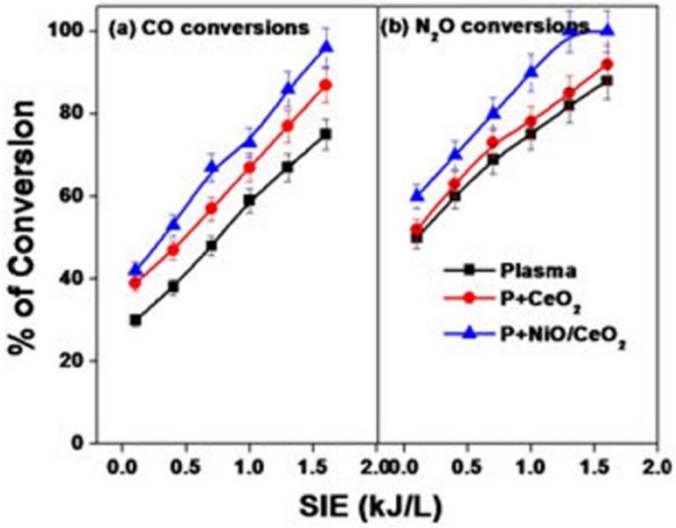

Figure 4.19: Performance of plasma reactor with CeO_2 and NiO/CeO_2 catalysts during conversion of 0.4 v% each of N_2O and CO.

As seen from the data presented in Fig. 4.19 that CO conversion was 96% for NiO/CeO_2 combined plasma system, higher than that of plasma alone (75%). It may be concluded that addition of NiO to CeO_2 may increase oxygen vacancies that may be compensated by the atomic oxygen formed due to N_2O

decomposition. Raman and TPR also confirmed the formation of $Ce_xNi_{1-x}O_{2-\delta}$ solid solution that not only improved the catalyst activity but also the selectivity to CO_2. The best activity and selectivity of NiO/CeO_2 catalyst towards CO_2 (100%) may be due to high redox nature of NiO/CeO_2 that can stabilize atomic oxygen. Oxygen mass balance during N_2O decomposition was estimated with and without catalyst, which confirms the decrease in O_2 selectivity by the addition of catalyst (27.5 to 5% at 1.6 W shown in Fig. 4.20).It is worth mentioning that recombination of atomic oxygen is prevented on NiO/CeO_2. Raman spectra confirmed the presence of defects on NiO/CeO_2 catalyst and the presence of the oxygen vacancies due to the formation of $Ce_xNi_{1-x}O_{2-\delta}$ solid solution [129], whereas TPR confirmed the enhanced reducibility of low temperature reduction peak (TPR spectra) indicating the oxygen mobility within $Ce_xNi_{1-x}O_{2-\delta}$ solid solution [123]. Therefore, the probability of adsorption of O^* is high on NiO/CeO_2[123, 124,129] that may improve the CO_2 selectivity in plasma catalytic approach, whereas, recombination of atomic oxygen may be primary reaction for plasma alone. The slight improvement on NiO addition to CeO_2 was due to creation of more defect sites.

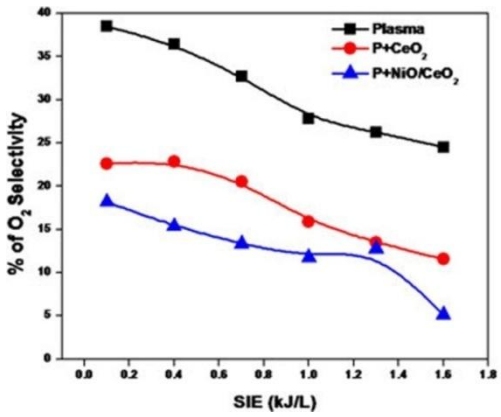

Figure 4.20: Selectivity profile of O_2 estimated and compared for with and without catalyst

4.4. Conclusions: Direct decomposition of nitrous oxide into N_2 and O_2 was studied in a nonthermal plasma dielectric barrier discharge (DBD) reactor operated under ambient conditions. Typical results indicated that even though high residence time favored high conversion; it also demands high input energy. Hence, for the practical applications, high concentration and low residence time are preferred. By

optimizing the reaction conditions, close to 100% N_2O decomposition was achieved at 1.6 W. It was confirmed that packing the discharge volume influences the conversion and among the dielectric materials studied, ceramic beads showed the best conversion that was assigned due to improved discharge strength. It has been concluded that the packed bed DBD is an efficient approach to control N_2O emissions. Moreover the CO oxidation by in-situ decomposition of N_2O was carried out in a dielectric barrier discharge reactor packed with modified CeO_2 catalysts. The performance of the DBD rector was found to increase on addition of NiO/CeO_2 catalyst that may be assigned due to the presence of oxygen vacancies on the surface of the catalyst that stabilize the atomic oxygen formed during N_2O decomposition. Absence of NO confirms that catalytic plasma approach developed in the present study showed promise for direct decomposition of N_2O into N_2 and O_2 and for in-situ conversion of CO into CO_2.

CHAPTER 5

Catalytic nonthermal plasma reactor for dry reforming of methane

5. 1. Introduction

The negative effect greenhouse gases, especially carbon dioxide (CO_2) and methane (CH_4) is well established and there is an immediate need to control the emission of these gases [130-133]. Traditional approaches to regulate CO_2 include sequestration, whereas methane has been converted to hydrogen in steam methane reforming (SMR). Even though hydrogen production by this approach is a fledged technique, it may not be environmentally benign due to simultaneous evolution of carbon dioxide (CO_2), whereas CO_2 sequestration has a limited scope. During the past decades, CO_2 reforming of CH_4, also known as dry reforming of methane (DMR) has been attracting considerable attention from both industrial and environmental perspectives, especially as an alternative for the production of synthesis gas (H_2+CO)[134]. Syngas is one of the most important industrial feed stocks for the production of a variety of chemicals in so-called Fischer Tropsch processes [135-137].Even though several thermal, catalytic, plasma and plasma catalytic processes were proposed for dry reforming,[50, 127, 130,138-141]on a closer look, dry reforming is more endothermic and demands 20% higher energy than SMR. In addition, optimization of conditions for desired H_2/CO ratio has been a challenge. Dry reforming conditions imply temperatures in the range 800-1100 ^{0}C and a pressure well above ambient conditions where catalyst may not be very active and undergoes deactivation [130].

In recent years, industrial applications of non-thermal plasma (NTP) generated under ambient conditions has been receiving considerable attention [47, 50, 59, 136,142]. NTP generated by electrical discharges under ambient conditions has specific advantages like mild operating conditions, as NTP is mainly composed of electrons, ions, excited atoms and molecules, radicals and metastable ions. These highly energetic electrons initiate the chemical reactions in gas phase. In addition, due to low degree of ionization, most of the energy in NTP will be utilized for accelerating electrons. Hence, with a suitable

configuration of the reactor and catalyst, dry reforming by NTP approach may be made energetically feasible [47, 59,142].

The combination of plasma and heterogeneous catalysis for syngas production by hydrocarbon reforming has been recently tested and it was concluded that both chemical and physical properties of the plasma and catalyst may be modified by the integration of catalyst in plasma discharge zone [43, 58, 138]. The presence of catalyst in plasma may show synergy to maximize the process performance [58].It has been shown that metal based catalysts on different supports (Al_2O_3, SiO_2, TiO_2, ZrO_2, CeO_2 and zeolites) showed significant activity in dry reforming [143-147]. Especially, Ni-based catalysts have been widely tested for dry reforming reaction due to their low cost, high activity and selectivity [143, 147-149]. Many studies have been focused on the selection of promoters, supports and preparation methods to increase the activity of Ni-based catalysts for dry reforming [148-156].It was reported that Ni-based catalysts prepared by the impregnation method deactivate quickly [134].

During the present study, solution combustion (SC) was employed to prepare $NiOx/Al_2O_3$ catalysts with varied NiO contents from 10 to 30 wt. %. The as-synthesized catalysts were characterized by N_2 adsorption–desorption, XRD, TEM and H_2-TPR. Dry reforming of methane was tested by operating the plasma in dielectric barrier discharge (DBD) configuration and with Ni/Al_2O_3 integration plasma. Plasma reactor was optimized and various parameters like applied voltages, composition of the gas mixture and catalyst combination to achieve the best performance.

5. 2. Experimental

5.2.1. Catalyst preparation

Desired amounts of Ni $(NO_3)_2 \cdot 6H_2O$ and Al $(NO_3)_3 \cdot 9H_2O$ were dissolved in minimum amount of water and required amount of citric acid to maintain oxidant/fuel = 1 was added under vigorous stirring [150]. The resulting solution after sonication at room temperature for 2 h was transferred to a quartz beaker and introduced into the preheated muffle furnace at 450°C to achieve spontaneous combustion. The prepared $Ni–Al_2O_3$ catalysts were denoted as x% Ni–Al (where x=10, 20 and 30 wt% Ni on Al_2O_3 in the catalyst).

For comparison, Al_2O_3 were also prepared under the same conditions. Synthesized metal oxides were reduced to the metallic state in H_2 atmosphere (100 mL min^{-1}) for 6h at 600 °C. After reduction, the Ni-based catalyst was cooled to room temperature in H_2 flow to prevent bulk oxidation of the Ni nanoparticles [34].

5.2.2. Catalyst characterization

Nitrogen adsorption–desorption isotherms were obtained with a Quantachromeautosorb automated gas sorption analyzer (NOVA 2200e). Prior to adsorption, the samples were degassed under vacuum at 200 °C for 4 h. Specific surface areas were determined by Brunauer Emmet Teller (BET) method. Powder X-ray diffraction (XRD) patterns were obtained on a PANalyticalX'pert pro X-ray diffractometer using Cu Kα (λ= 1.541 Å radiation, 30 mA, 40 kV). The formation of nano sized catalyst was confirmed by TEM performed on a FEI model TECNAI G 220 S-Twin instrument. The catalyst powders were dispersed in ethanol by ultrasonic and the suspension was then dropped onto a carbon-coated copper grid. ICP-OES on a Teledyne prodigy high dispersion analysis was performed to identify the amount of Ni present. The nickel dispersion (calculated from H_2-chemisorption after 6 h reduction at 600 °C) and H_2-temperature programmed reduction (H_2-TPR) measurements were carried out in a flow system Quantachromeautosorb-IQ (automated gas sorption Analyzer) equipped with a thermal conductivity detector (TPR-TCD). Prior to the H_2-TPR measurements, a 50 mg of the sample placed in a quartz U-tube reactor was pretreated in argon stream at 300 °C for 0.5 h and then cooled to room temperature. The TPR profile was recorded by increasing the temperature of catalyst bed at 30 °C to 950°C in 10% H_2 flow 50 mL min^{-1}.

5.2.3. Plasma reactor

The experimental set-up is shown in Fig. 5.1. Briefly, Non-thermal plasma was generated in a cylindrical quartz tube. Outer surface of the quartz tube wrapped with copper wire for 15 cm acts as an outer electrode, whereas a stainless steel rod placed at the center of the tube was the inner electrode. The discharge gap was 3.5 mm that corresponds to adischarge volume of 27.2 cm^3. 10% of this active volume

between electrodes was packed with Ni/Al_2O_3 catalyst placed in between quartz wool plugs towards the outlet of the reactor. The flow rate of the gas mixture was kept constant at 40 ml/min and a required amount of high pure argon was used as the diluent to achieve desired concentration.Plasma reactor was powered by a high voltage AC generator (Yaskawa varispeed F7 AC inverter upto 40 kV and 50 Hz). The voltage (V) and charge (Q) waveforms were recorded with an oscilloscope Tektronix, (TDS 2014B) by using a 1000:1 high voltage probe (Agilent 34136A HV). The voltage across the capacitance multiplied by its capacitance corresponds to charge accumulated in reactor. The plasma input energy per cycle is equal to the area enclosed by the charge-voltage curve in the V-Q Lissajous figure [47].The specific input energy (SIE) was calculated by dividing the power with flow rate of the gas as expressed below,

SIE (J/L) = Power (W)/ gas flow rate (L/Sec)

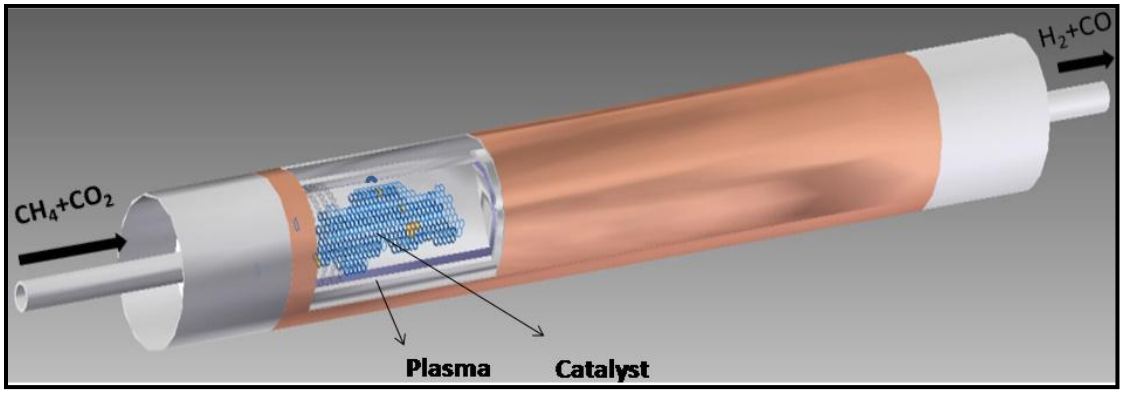

Figure 5.1: Schematic representation of catalyst packed dielectric barrier discharge reactor for dry reforming of methane.

The gas mixture was controlled by a set of mass flow controllers (Aalborg-USA). CH_4 (10 vol% diluted in Ar) and CO_2 (5 vol% diluted in Ar) gases were introduced into the reactor. At the reactor outlet gas analysis was made with an online gas chromatograph (Varian 450-GC), whereas an on-line GC-MS (Thermo Fischer) was used to identify the by-products. CH_4 and CO_2 conversion, CO and H_2 selectivity, H_2/CO ratio and H_2 yield are calculated as given below

$$\mathrm{CH_4\ conversion\ (\%)} = \frac{[\mathrm{CH_4}]\ \text{in inlet} - \text{moles of } [\mathrm{CH_4}]\ \text{outlet}}{[\mathrm{CH_4}]\ \text{in inlet}} \times 100$$

$$\mathrm{CO_2\ conversion\ (\%)} = \frac{[\mathrm{CO_2}]\text{in inlet} - [\mathrm{CO_2}]\ \text{outlet}}{[\mathrm{CO_2}]\ \text{in inlet}} \times 100$$

$$\mathrm{H_2\ selectivity\ (\%)} = \frac{[\mathrm{H_2}]\ \text{produced}}{2 \times [\mathrm{CH_4}]\ \text{converted}} \times 100$$

$$\mathrm{CO\ selectivity\ (\%)} = \frac{[\mathrm{CO}]\ \text{produced}}{[\mathrm{CH_4}]\ \text{converted} + [\mathrm{CO_2}]\ \text{converted}} \times 100$$

$$\mathrm{H_2/CO\ ratio} = \frac{[\mathrm{H_2}]\ \text{produced}}{[\mathrm{CO}]\ \text{produced}}$$

$$\mathrm{H_2 yield} = \frac{\mathrm{CH_4 conversion\ XH_2 selectivity}}{100}$$

5.3. Results and Discussion:

5.3.1 XRD characterization & N_2 adsorption studies:

XRD patterns of the reduced samples shown in Fig. 5.2 confirmed the characteristic patterns of γ-Al_2O_3, $NiAl_2O_4$ and Ni phases. These XRD patterns also revealed that γ-Al_2O_3 and Ni had low crystallinity, as evidenced by the broad peaks due to the presence of γ-Al_2O_3 and $NiAl_2O_4$, respectively[134].The designed catalyst exhibited high specific surface area (SSA of 0, 10%, 20% and 30%Ni/Al_2O_3 is 250, 240, 230 and 195 m^2g^{-1} respectively). With increasing nickel loading, the main diffraction peak of γ-Al_2O_3 shifted to lower 'd' spacing due to diffusion of NiO particles into the support structure to form the $NiAl_2O_4$ phase [150]. The peaks for the defect spinel phase may be observed at values 2θ 37^0, 43.5^0 and

66.7^0; whereas relatively higher 2θ values indicated that Ni^{2+} in the spinel phase has been reduced to Ni^0. From ICP-OES experiment it is confirmed that the Ni % in the catalysts 10, 20 and 30% of Ni/Al are very close to the expected nickel loading (Shown in Table 5.1). The estimated metal dispersion for 10, 20, 30%Ni/ Al_2O_3catalysts are shown in Table 5.1 and it may be concluded that higher nickel dispersion is observed for 20%Ni/Al.

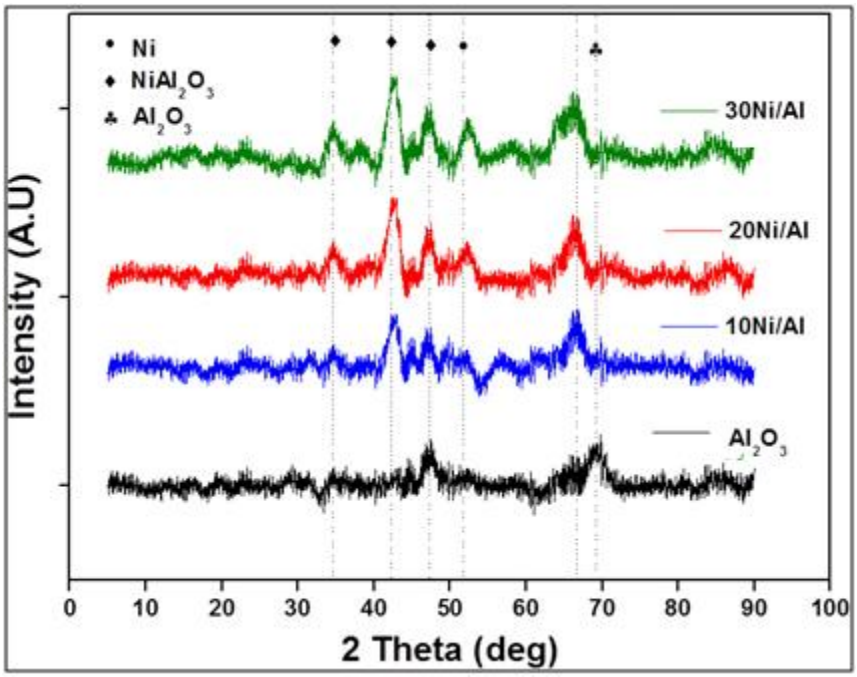

Figure 5.2: XRD patterns of reduced Ni–Al_2O_3 catalysts and Al_2O_3support.

Table 5.1: Physicochemical characteristics of the catalysts.

Catalyst	Surface Area (m^2/g)		Metal dispersion (%)	Ni content (wt%)	Carbon deposit after 1hr reaction ($mmole_{Carbon}/g_{cat}$)
	Before Treatment	After 1hr Treatment			
10%Ni/Al_2O_3	**240**	**220**	**2.9**	**9.1**	**0.38**
20%Ni/Al_2O_3	**230**	**225**	**4.2**	**18.5**	**0.32**
30%Ni/Al_2O_3	**195**	**150**	**3.0**	**28.9**	**0.71**

5.3.2. TEM

The TEM micrographs of the reduced 20%Ni/Al_2O_3 catalysts are presented in Fig.5.3. As seen in Fig. 5.3, Ni nanoparticles with typical diameter < 6 nm are uniformly dispersed on γ-Al_2O_3 indicating that solution

combustion method is a quick method for one pot synthesis of highly dispersed Ni nanoparticles on Al_2O_3. The inset diffraction pattern confirms the d-spacing 0.22 nm matches well with value calculated from XRD. The particle size of Ni in 10% and 30% Ni/Al_2O_3 is 13 and 18 nm respectively. Obtained results suggested that the spinel formation or solid solution enhances the particle dispersion which resulted in low particle sizes for aforementioned 20%Ni/Al_2O_3 [73, 150, 151].

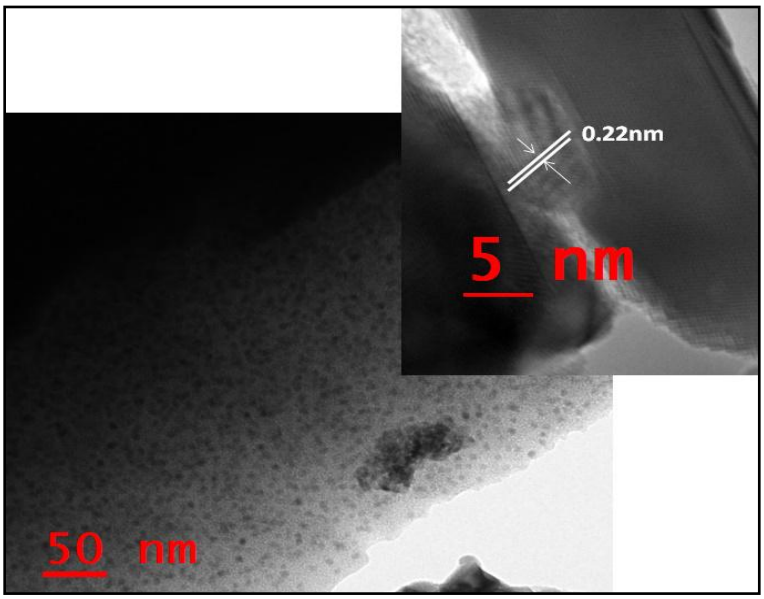

Figure 5.3: Typical Transmission Electron Microscopy (TEM) of the reduced 20Ni–Al catalyst.

5.3.4. H_2-TPR

Figure 5.4 presents the TPR profiles of NiO/Al_2O_3 catalysts confirming the reducibility of Ni^{2+} ions. The reduction events may be mainly divided into four types: α, β_1, β_2 and γ[151]. The small peak located in the lower temperature region (<450 ^{0}C) was assigned to α-type NiO species, which are free nickel oxides species that may have a weak interaction with alumina.[34] The peak around 530 to 750 ^{0}C represents β_1 and β_2-type NiO species that may have relatively stronger interaction with alumina than that of α-type NiO [151].Previously it was reported that β_1-type NiO species with Ni-rich mixed oxide phase are more reducible NiO than β_2-type NiO species with Al-rich mixed oxide phase [152, 153]. Clearly, for NiO/Al_2O_3 catalysts, as the Ni loading increases, β_1 species gradually increase up to 20% and then

decreases for further loading, while β_2-type NiO species continue to increase. The high-temperature peaks above 800 ^{0}C are assigned to γ-type NiO species which are due to the stable nickel aluminates that has a spinel structure [150].

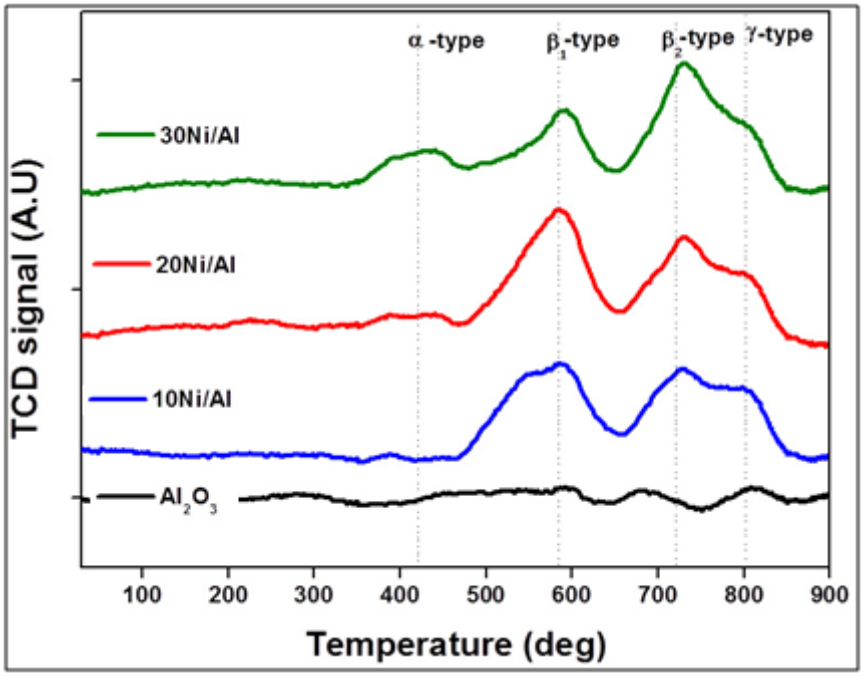

Figure 5.4: TPR spectra of fresh calcined Ni–Al_2O_3 catalysts.

5.4. Effects of mole ratio of CH_4 and CO_2

In order to understand the influence of CH_4/CO_2 molar ratio on conversion of the reactants, the mole ratios of CH_4 and CO_2 are varied between (1:2, 1:1 and 2:1 with balance argon) at a constant flow rate of 40 ml/min (residence time of 40.8 s) and the typical results are presented in Fig. 5.5. The voltage was varied between 12 to 26 kV at 50 Hz that corresponds to SIE variation between 2.1 to 7.2 kJ/L. As seen in Fig. 5.5, on decreasing the amount of methane in the feed gas, conversion increases. CH_4 conversion was 38 (at 5.2 kJ/L), 46 (at 6 kJ/L) and 52% (7.2 kJ/L) respectively for 2:1, 1:1 and 1:2 CH_4/CO_2 mole ratios. The same trend was observed for CO_2 conversion and under the same experimental conditions, CO_2 conversion was 23, 39 and 43%, respectively. It may be concluded that CH_4 and CO_2 conversions are lowest for 2:1 mixture and on decreasing the CH_4 concentration in the mixture, conversion increased.

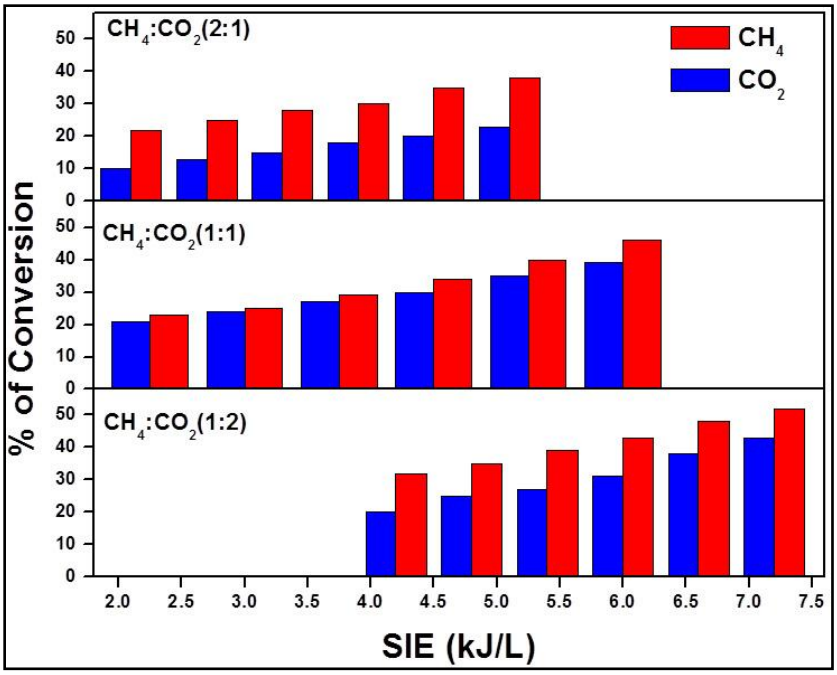

Figure 5.5: Conversions of CH_4 and CO_2 in NTP-DBD reactor for different mole ratios.

Figure 5.6a shows the selectivity to H_2 and CO as a function of SIE for different CH_4/CO_2 ratios. As seen from the Fig.5.6a, best selectivity to H_2 and CO was achieved at high initial concentration of methane**.** For CH_4/CO_2 =2:1, the H_2 and CO selectivity was 35 and 38%, respectively at the SIE of 5.2 kJ/L. With 1:1 and 1:2 ratios, the H_2 and CO selectivity is 32.5, 38.5% (6 kJ/L) and 25, 43% (7.2 kJ/L) respectively. Figure 5.6b shows the H_2/CO ratio as a function of SIE for all the three CH_4/CO_2 ratios. The average H_2/CO ratio for 2:1 mixture was 1.18, which decreased to 0.8 and 0.6 on varying CH_4/CO_2 to 1:1 and 1:2, respectively.

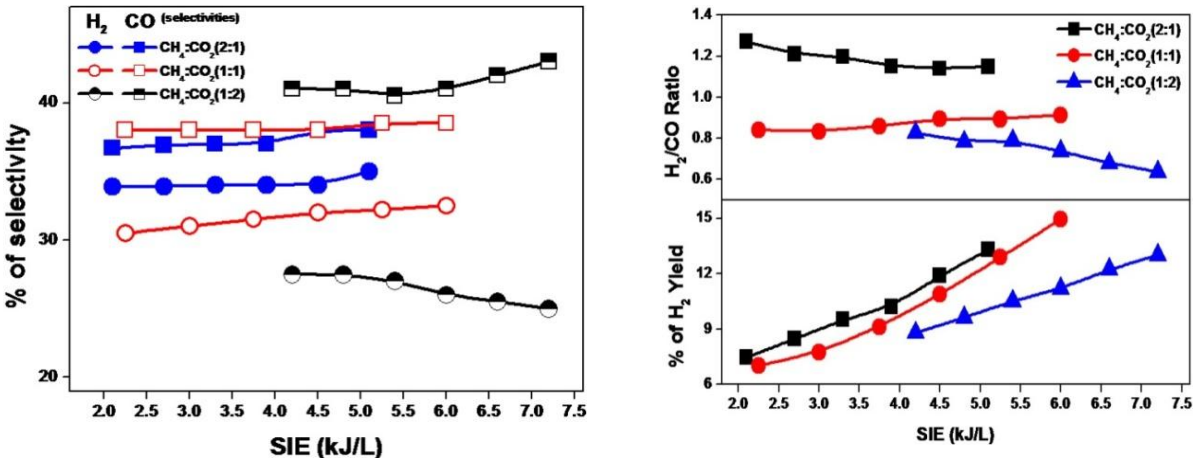

Figure 5.6: (a) H_2 and CO selectivity, (b) H_2/CO ratio and (c) H_2 yield

5.5. Effects catalyst on the conversion of CH_4 and CO_2:

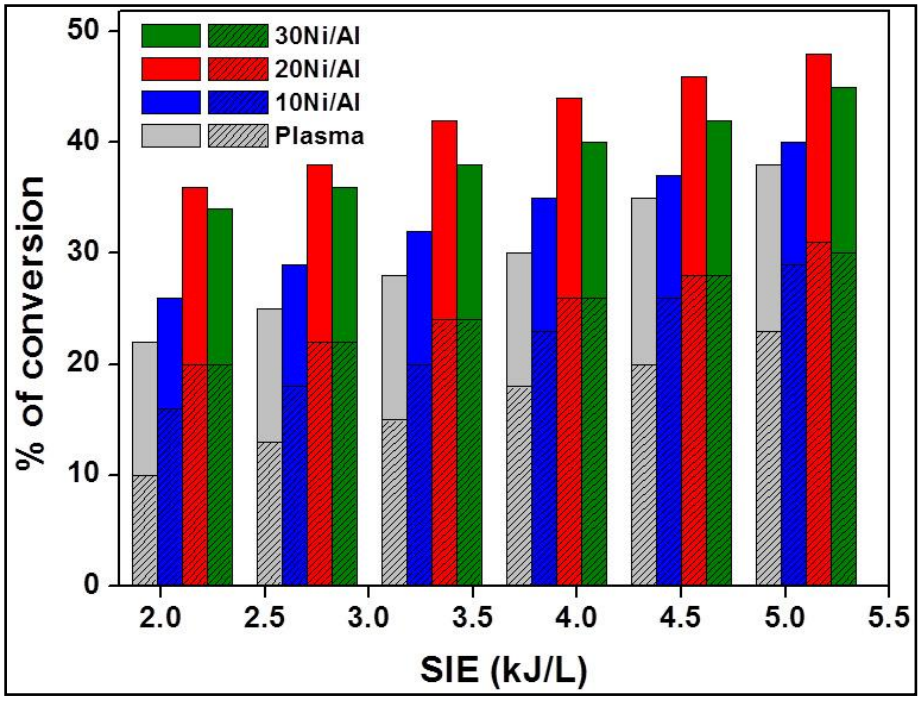

Figure 5.7: Effect of catalyst on CH_4 and CO_2 at the reagents molar ratio of CH_4:CO_2- 2:1.

Figure 5.7 shows the performance of catalytic plasma reactor as a function of SIE on integration of 10, 20 and 30% Ni-aluminate DBD reactor. The total gas flow rate was maintained at 40 ml min^{-1} and 1g of the catalyst flakes are loaded in a packed configuration and the reactant feed ratio, i.e., CH_4/CO_2 fixed at 2:1.

As the SIE increases, CH_4 and CO_2 conversions increased gradually. It is worth mentioning that the conversions of CH_4 and CO_2 with plasma reactor without catalyst was 38 and 23% respectively at SIE of 5.2 kJ/L. Interesting observation is the improvement in the conversion on addition of 10, 20 and 30% NiO/Al_2O_3 to plasma reactor. The conversion of CH_4 increased to 40, 49 and 45%. Under the same experimental conditions, CO_2 conversion also increased to 29, 30 and 30% respectively. For CH_4/CO_2 = 2:1, the conversion of CH_4 for 20 % Ni/Al_2O_3 (49%) was higher than that of plasma (38%), 10% Ni/Al_2O_3 (40%) and 30% Ni/Al_2O_3 (45%). The decrease in the conversion over 30% Ni/Al_2O_3 may be due to more carbon deposit on the catalyst surface. It is logical to assume that 30% Ni loadings leads to more acidic sites that may favor carbon formation. Also Ni/Al_2O_3 developed in the present study is a good catalyst for carbon gasification, as confirmed by temperature programmed oxidation, where deposited carbon was oxidized [157].

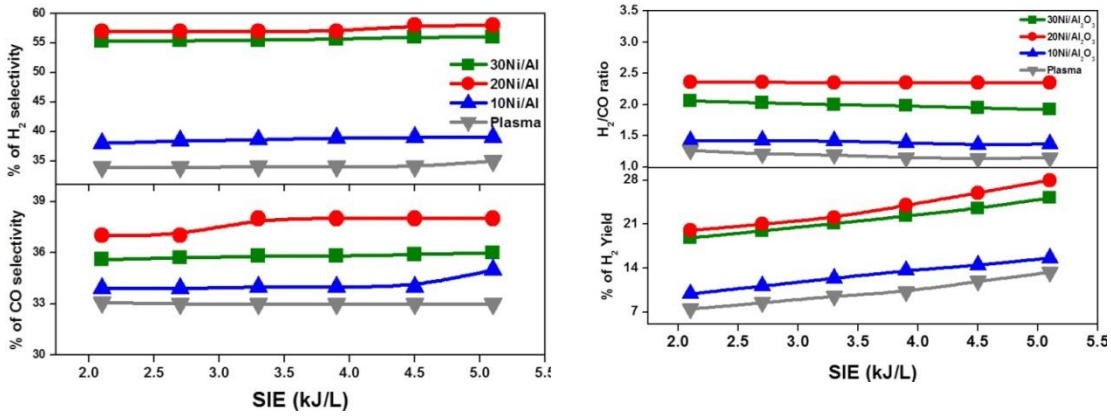

Figure 5.8: Effect of catalyst on (a) H_2 and CO selectivity, (b) H_2/CO ratio and (c) H_2 yield of reactant feed ratio of CH_4/CO_2 = 2:1

Figure 5.8a represents the influence of 10, 20 and 30% Ni/Al_2O_3 on the H_2 and CO selectivity at a constant feed ratio of 2:1. As seen in Fig. 5.8a, on addition of NiO catalysts, the selectivity of H_2 significantly increased from 35 to 40%, 59% and 56 % respectively, whereas CO selectivity nearly remains the same around 35%. Interesting observation is the improvement in H_2/CO ratio to 2.25 on addition of 20% Ni/Al_2O_3 against1.18 with plasma reactor (Fig. 5.8b). Like-wise, double the amount of H_2 yield was achieved in the presence of 20% Ni/Al_2O_3 as compared to plasma and plasma with other catalytic systems (Fig. 5.8c). The best activity of 20%Ni loading may be due to small crystallite size, high

nickel dispersion and high reducibility. For 20%Ni/Al_2O_3catalyst, low and high temperature $NiAl_2O_4$ phase reduction peaks occurred at 580°C (β_1) and 710 (β_2) respectively, as shown in Fig. 5.4. It is emphasized in literature that the surface $NiAl_2O_4$ is easily reducible than the bulk $NiAl_2O_4$ phase and also has more resistance to sintering, compared to free NiO. Therefore the reducibility of surface $NiAl_2O_4$ is more for 20%Ni loading than other weight ratios, hence the highest catalytic activity.

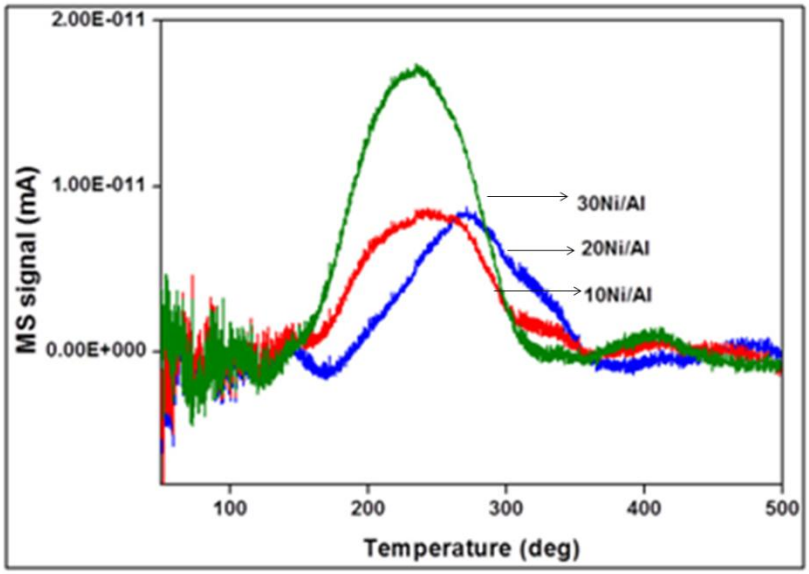

Figure 5.9:. Formation of CO_2 on different Ni/Al_2O_3 catalytic systems after 1 h reaction

In order to ensure the carbon deposit on catalyst during the course of the reaction, temperature programmed oxidation of the spent catalysts was carried out and results are shown in Fig. 5.9. It is clear from Fig. 5.9 that the carbon deposition on spent catalyst gradually increased with increasing Ni loading 20% showed lowest carbon formation, which is in agreement with the best catalytic activity of 20% Ni/Al_2O_3 catalyst. Furthermore XRD patterns of the spent catalysts remain the same (not shown) and a small decrease in the surface area of the samples was observed (Table 5.1) probably due to sintering of $NiAl_2O_4$ during the course of reaction. Formation of other reaction products such as ethane, propane, propene and traces of methanol were observed, however, they were not quantified.

5.6. Conclusions:

Dry reforming of methane with carbon dioxide was carried out in a nonthermal plasma reactor operated in a dielectric barrier discharge configuration. Influence of composition of the reactants in the feed was investigated at room temperature, at a constant feed flow rate 40 mL/min and with the voltage variation between 12 to 26 kV. With decreasing CH_4/CO_2 mole ratio, both CH_4 and CO_2 conversion increased gradually. Consequently, the selectivity to CO and H_2 and H_2/CO ratio in the synthesis gas increased. The specific energy demand depends on the mole ratio of the reactants and it followed the trend 1:2>1:1>2:1 for CH_4:CO_2. It was observed that H_2/CO ratio was only 1.2 with plasma reactor alone. In order to improve the performance of the DBD reactor, Ni catalysts were prepared by combustion synthesis and 10% of the active discharge volume was packed with catalysts. Typical results indicated the improved performance of the reactor for dilute mixtures and addition of Ni/Al_2O_3 catalysts. Among the catalysts studied, 20% Ni/Al_2O_3 showed the best conversion and highest H_2/CO ratio of 2.25 against 1.2 with plasma reactor alone. The best catalytic behavior of 20% Ni/Al_2O_3 catalyst in the dry reforming of methane may be due to the formation of nanocrystalline $NiAl_2O_4$, highly dispersed Ni nanoparticles and/or due to high reducibility, of the 20%Ni/Al_2O_3catalyst as compared to higher or lower wt% of Ni. However, there is a need to optimize the reaction conditions to decrease the input energy and make the process feasible for practical applications.

CHAPTER 6

Nonthermal plasma assisted co-processing of CH_4 and N_2O for methanol production

6.1. Introduction

Natural gas is a mixture of several hydrocarbons (at least 95%) and non-hydrocarbon gases such as nitrogen (up to 5 %), carbon dioxide and hydrogen sulfide. Methane (CH_4) is the principal component (between 70 and 90 %) of most natural gas reserves [158]. For decades, methane has been the feed stock for chemical industry, especially for the production of valuable chemicals and fuels, such as hydrogen gas, higher hydrocarbons, syngas (a mixture of CO and H_2), methanol (CH_3OH) and formaldehyde (CH_2O). Development of efficient natural gas conversion technologies is therefore essential for a sustainable feedstock for the chemical industry and for protecting our environment. The conversion of methane to value-added products has gained a lot of attention. While the study continues on the oxidative coupling [159, 160] and selective oxidation [161, 162]processes, significant attention has been directed to the production of synthesis gas [18, 21, 163]. In conventional steam methane reforming and CO_2 reforming, methane will be converted to syngas that may be converted into a variety of products in a set of downstream processes, such as Fischer–Tropsch process [164-167]. Metal catalysts, e.g. Ni, Co and noble metals (Pt, Rh), are very active for CPOM. However, the stability of catalysts is still a matter of concern, despite intensive investigation of CPOM over metallic catalysts [168-170]. Moreover metallic catalysts may suffer from deactivation due to sintering and metal loss via the formation of volatile metal oxides [171]. Study on CPOM over thermally stable oxides is rather limited [172-175]. However, partial oxidation of CH_4 directly to methanol or formaldehyde offers interesting opportunities and may lead to the production of liquid fuels and chemicals. In addition, CH_4 and N_2O are long-lived in the atmosphere and are major contributors to global warming [51, 52]. In this direction, various attempts have been made to convert methane into methanol [176-178].

It has been first demonstrated by Lunsford and co-workers that molybdenum supported on silica was an excellent catalyst for partial oxidation of CH_4 with N_2O [179-181]. However, the selectivity to methanol is not high. However, conventional thermal methods for CPOM typically require extreme reaction conditions such as high temperature (up to 1000 ^oC) and pressure (>10 atm), which limit the industrial applications of the catalytic partial oxidation process.

As methane is a stable compound due to high C–H bond strength and perfect symmetry, reactions with methane, especially partial oxidation to methanol (MPOM) demands severe reaction conditions [180]. Alternatively, decomposition of CH_4 by using nonthermal plasmas (NTP) under ambient conditions is an alternative route for the utilization of methane for conversion to more valuable products (H_2, CH_3OH and HCHO). NTP offers unique advantages like inducing gas phase reactions by electron collisions, ease of operation, etc. As stated earlier, NTP is characterized by high electron temperatures and the bulk gas temperature remains at room temperature [47, 58, 142, 182,183].

Experiments performed by Shepelevet al. with CH_4 and O_2 in a DBD reactor reached a methanol selectivity of 20% [184]. In addition, a pulsed corona/DBD discharge was also investigated for the direct partial oxidation of methane to methanol in a methane flow with small amounts of oxygen. In these experiments that were performed under ambient conditions, a relatively high methanol yield of2.4% and a high methanol selectivity of 33% were reported. Even in a mixture of CH_4 and air (7:3), a methanol concentration of 0.6 vol% was obtained at atmospheric temperature and pressure. Small amounts of methanol were also observed in a pulsed streamer corona operating in a mixture of CH_4 with CO_2 or water vapour. Okazaki et al. and Okumoto et al. [185, 186] have investigated the direct conversion of $CH_4$to CH_3OH using silent electric discharge at 250 Hz and voltages up to 25 kV, major products were CH_3OH and CO_2. Selectivity of methanol was greater at lower oxygen concentrations, and dissociation of oxygen was noted as the primary pre-requisite for methanol formation.

Another interesting aspect was that the addition of catalyst to the DBD reactor also leads to a better activity and selectivity than plasma alone. There were studies reporting catalytic partial oxidation of methane (CPOM) to methanol over various catalysts by using NTP reactor [187, 188]. Noble metal catalysts, such as Ir, Au, Ru, Pt and Rh were investigated and they have higher activity and selectivity than the base metal catalysts. In addition, base metal catalysts need long pretreatment in reducing atmosphere and rapidly lose activity on contact with air. However,due to cost benefits, base metal systems have advantage over noble metal ones. Consequently, it is important to develop a stable, noble metal-free and highly active system for CPOM reaction. Among the non-noble metal catalysts studied so far, cobalt-based catalysts were reported to show the best performance. Cobalt-based catalysts, however, prone for deactivation due to the carbon deposition, and this deactivation increases with the increasing reaction temperature [189]. In this context, due to the carbon tolerant nature, Ni based catalysts on various supports were tested for CPOM reaction [156, 190-192]. However, the product distribution and methanol selectivity was not satisfactory. It was reported that rare earth oxides, such as CeO_2, Y_2O_3, La_2O_3, offer the greatest potential as catalyst support for Ni catalyst due to their high oxygen storage capacity and adequate metal-support interactions [174, 193-195].

In addition to the support effect, the doped metal can also affect the catalytic performance. Number of studies revealed that the bimetallic catalysts are more active than monometallic ones [194-198]. Specific interactions between metal species in bimetallic catalysts also results in a completely different adsorption properties [196]. For example, it has been demonstrated that addition of Cu or Na, K metals to the Ni- catalyst decreases the reduction temperature of the NiO and increases the catalyst durability, due to the interactions between Ni and the doped species [197].

In the present study, NTP assisted co-processing of nitrous oxide (N_2O) and methane (CH_4) was attempted. The Influence of various conditions like specific input energy (SIE), mole ratio of the feed gases were studied. Further, catalytic performance of Cu doped Ni catalyst supported on the $CeO_2$was

investigated. The promoting effect of Cu to Ni catalyst for the methanol and hydrogen production during plasma assisted CPOM reaction was studied.

6.2. Experimental

6.2.1. Catalyst synthesis: The copper substituted nickel on ceria bimetallic catalysts was prepared by solution combustion synthesis using citric acid as the fuel. For comparison, Cu (10 wt%), Ni (10 wt%) loaded on ceria were also prepared. The final catalysts were denoted as 10Cu/Ce, 10Ni/Ceand Cu-Ni(5-5)/Ce respectively. In a typical synthesis, appropriate amounts of $(NH_4)_2Ce(NO_3)_6{\cdot}6H_2O$, $Cu(NO_3)_2$, $Ni(NO_3)_2$. H_2O and citric acid (oxidant/fuel=1) were dissolved in minimum amount of distilled water at room temperature and sonicated for 30 min and transferred into an alumina crucible. The alumina crucible was then placed in a preheated furnace maintained at ~450^0C for 5 min. The solution undergoes dehydration and a spark appears at one corner, which spreads throughout the mass yielding a voluminous solid product with grey color. Prior to the activity test, the samples were calcined at 600^0C over 4 hours to remove the carbon content.

6.2.2. Characterization techniques: Formation and identification of the designed catalysts were done with powder X-ray diffraction (XRD) patterns by PANalyticalX'pert pro X-ray diffractometer using Cu K_α (λ = 1.541 Å radiation, 30 mA, 40 kV). Crystallite size was calculated by using the Scherrer's equation. The textural properties were studied by N_2 adsorption/desorption measurements at liquid nitrogen temperature (at 77K) in a Quantachromeautosorb automated gas sorption analyzer (NOVA 2200e). Before analysis, the samples were degassed at 250^oC for 6 h in vacuum.

The size and morphology of the nanoparticles were examined by using an FEI model TECNAI-G-220 S-Twin TEM instrument. To investigate the surface enrichment, the as-prepared samples were immersed in 50% dilute nitric acid solution for 24 h, filtered, and washed with deionized water thoroughly to remove any dissolved nickel oxide in the sample. Raman spectra of CeO_2 and ceria supported bimetallic catalysts were recorded on a Bruker senterra dispersive Raman microscope with

laser excitation of wavelength of 532 nm. X-ray Photoelectron Spectroscopy (XPS) data of the combustion synthesized catalysts were recorded by an Axis Ultra instrument under ultra-high vacuum condition ($<10^{-8}$Torr) and a monochromatic Al Kα X-ray source (1486.6 eV).

Temperature Programmed Reduction (TPR), temperature Programmed decomposition (TPD) and catalytic activity measurements were carried out in a flow system (Quantachrom eautosorb-IQ automated gas sorption Analyzer) equipped with a thermal conductivity detector (TPR-TCD). The data was reconfirmed with an in-built mass spectrometer (RGA Prisma plus-200) controlled by the software Quadera and the second confirmation was done with a pre-calibrated ULTRAMAT 23 multi-gas Analyzer (SIEMENS) that measures CO, CO_2 and O_2. For TPR measurements, 50mg of the sample was sandwiched between quartz wool plugs in a U-shaped quartz reactor and flushed with He for 30 min. The TPR profiles were obtained by heating the sample from room temperature to the desired temperature (600^oC) in 10% H_2 in Ar, (gas flow rates 40 ml / min and heating rate of 10^oC/min) and the gaseous products were sampled through a fine control leak valve to TCD after passing through a cold tarp to remove H_2O. Quantitative analysis was done by integrating the reduction signal and comparison was made by pre-calibrated signals.

6.2.3. Plasma reactor: A detailed description of the DBD reactor was reported elsewhere [47]. In a slightly modified configuration, the dielectric discharge was generated in a cylindrical quartz tube with an inner diameter of 20 mm. A copper wire rolled on the outer surface of the quartz tube acts as the outer electrode, whereas a stainless steel rod was used as the inner electrode (Figure6.1). The discharge length was 15 cm and discharge gap was fixed at 3.5 mm. The inner electrode was connected to AC high voltage source (Yaskawa varispeed F7 AC inverter, AC voltage 0-40 kV and frequency 50-1000 Hz variable), whereas the outer electrode was grounded. The discharge was ignited by applying AC high voltage in the range 12–20 kV (peak–peak) at 50 Hz. The flow rate of gas was controlled with mass flow controllers (GFC-17,Aalborg-USA). The energy dissipated during one period of voltage is calculated from the V-Q Lissajous diagram taken at different applied voltages and at fixed discharge gap of 3.5 mm and 50 Hz

frequency shown in Fig.6.2 (Shown for feed ratio of CH_4/N_2O-5:1 from 12-22 kV).The electrical power applied to the discharge in the DBD reactor was measured by using the V-Q Lissajous diagram, where the charge Q (i.e., time integrated current) was recorded by measuring the voltage across the capacitor (C = 1.5 μF) connected in series to the ground electrode.

Applied voltage was measured with a 1000:1 high voltage probe (Agilent 34136A) and the V–Q wave forms were monitored by a digital oscilloscope (Tektronix TDS 2014 B). The area of Lissajous figure (Figure 6.2) characterizes the energy dissipated during one period of voltage, from which power was calculated by multiplying with frequency.Specific input energy (SIE) of the discharge was calculated by following relation,

$$SIE\ (J/L) = \frac{Power\ (W)}{Gas\ flow\ rate\ (^{L}/_{sec})}$$

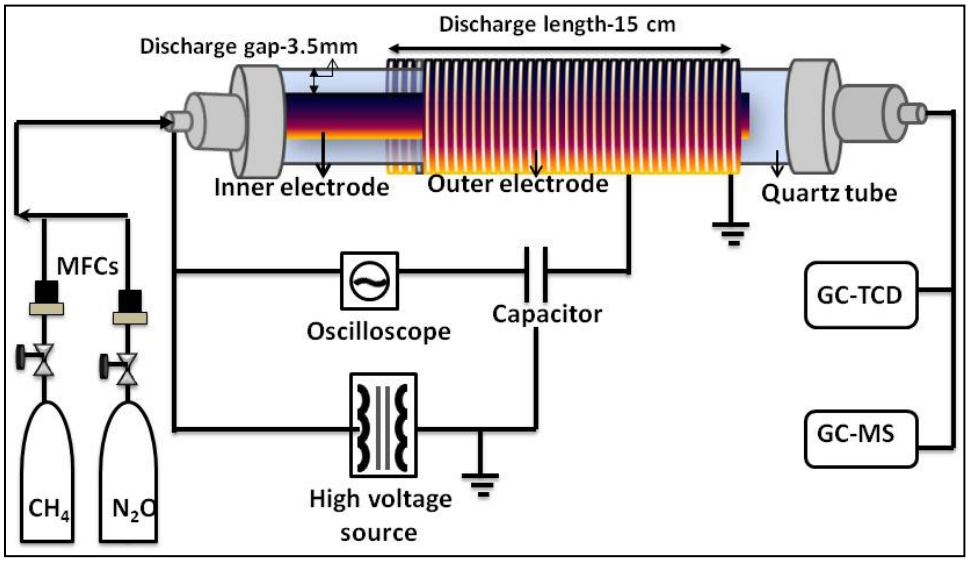

Figure 6.1: Schematic representation of NTP-DBD reactor

The gases used in the present study are high pure CH_4 (10% CH_4 diluted in argon) and N_2O (10% N_2O diluted in argon). CH_4 and N_2O were introduced into the discharge zone through a Teflon tube, whose concentrations along with the products (Methanol formaldehyde and hydrogen) were measured

with a gas chromatograph (Varian 450 GC) equipped with two TCD detectors, whereas an infrared CO_x analyzer (AIC, India) was used to monitor the CO and CO_2 formed in the reaction.

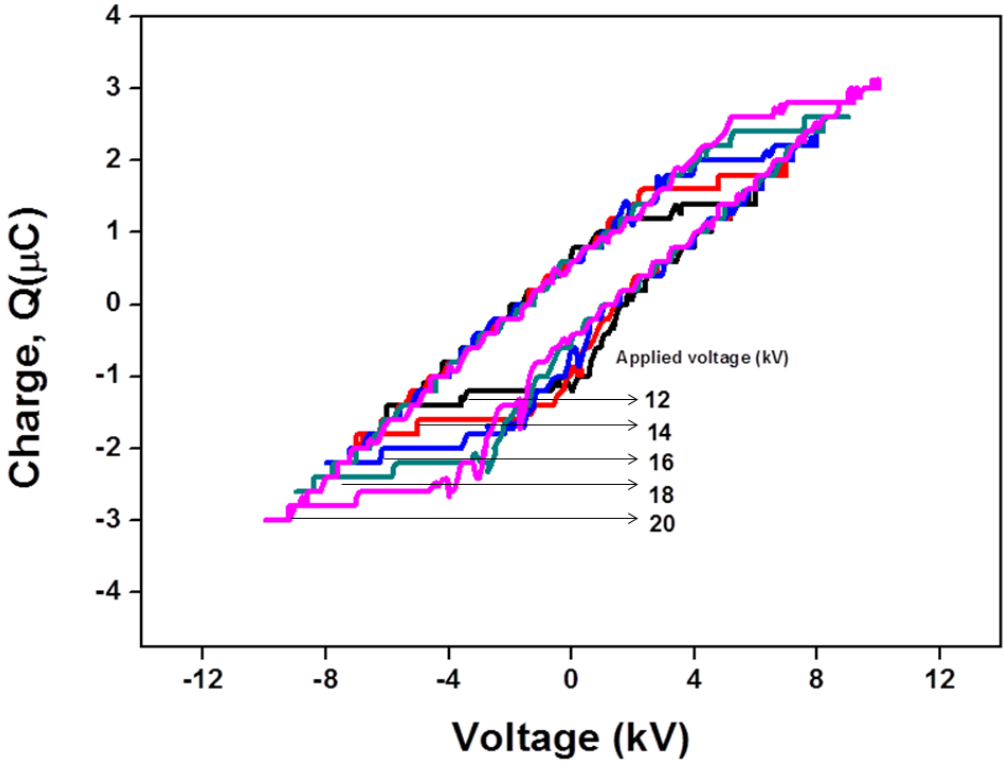

Figure 6.2: V-Q Lissajous diagrams of 12-22 kV taken at 3.5 mm discharge gap and 50 Hz frequencyfor feed ratio of CH_4/N_2O-5:1

Concentration of hydrogen was confirmed with a hydrogen gas analyser (Siemens, calomat 6E), whereas, other hydrocarbon products were identified by using GC-MS (Thermofisher). The selectivity of methanol, formaldehyde, hydrogen CO_2, CO and total carbon selectivity was defined as follows,

$$Conversion\ of\ CH_4\ (\%) = \frac{[CH_4]out}{[CH_4]in}\ X\ 100$$

$$Conversion\ of\ N_2O\ (\%) = \frac{[N_2O]out}{[N_2O]in}\ X\ 100$$

$$Selectivity\ of\ CH_3OH\ (\%) = \frac{[CH_3OH]out}{[CH_4]in}\ X\ 100$$

$$Selectivity\ of\ HCHO\ (\%) = \frac{[HCHO]out}{[CH_4]in}\ X\ 100$$

$$Selectivity\ of\ CO\ (\%) = \frac{[CO]out}{[CH_4]in}\ X\ 100$$

$$Selectivity\ of\ CO_2\ (\%) = \frac{[CO_2]out}{[CH_4]in}\ X\ 100$$

$$Selectivity\ of\ H_2\ (\%) = \frac{[H_2]out}{2\ x\ [CH_2]in}\ X\ 100$$

$$Total\ carbon\ selectivity\ (\%) = \frac{[CH_3OH]out + [HCHO]out + [CO]out + [CO_2]out}{[CH_4]in}\ X\ 100$$

6.3. Results and discussion

6.3.1. XRD: Crystalline phases of the Cu-Ni/CeO_2 catalysts

Figure 6.3 shows the XRD patterns of the 10CuO/CeO_2, 10NiO/CeO_2 and the Cu doped NiO/CeO_2 catalysts with 10 wt.% of metal loading. The XRD patterns of the all catalysts confirmed the fluorite structure of CeO_2 sample, confirming the dispersion of nickel oxide, and copper oxide.

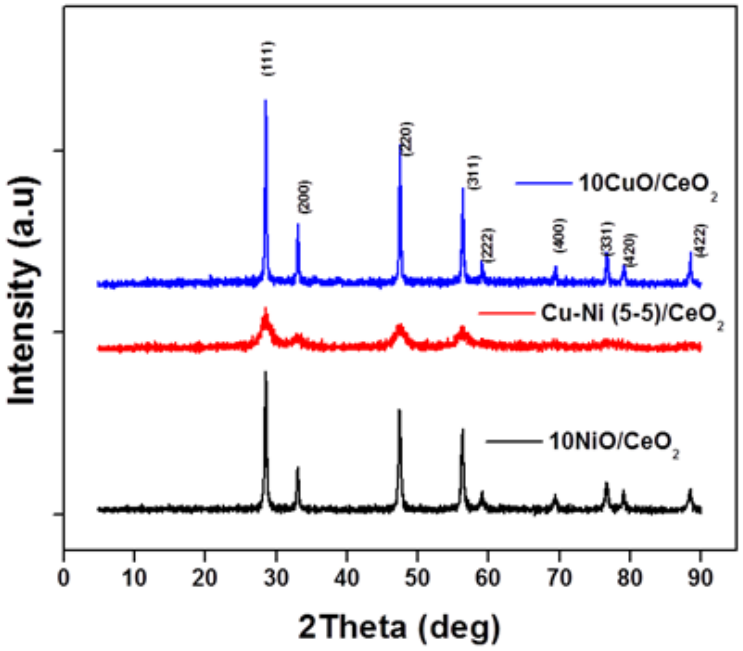

Figure 6.3: Powdered XRD patterns of fresh CuNiCe catalysts

This may infer that the nickel and copper may be dispersed finely on the support because of the segregation effect of the Cu-Ni system [197, 199]. On the bimetallic sample, diffraction peaks of Cu, Ni or Cu-Ni alloy were not observed, probably due to the small particle size of the active phase, which is below the detection limit. As seen in Table 6.1, the cell parameter decreases on introducing CuO and NiO content to CeO_2. The Cu and Ni addition also decreased the crystallite size of CeO_2 as shown in Table 6.1 that confirms the particle size of 15, 12, 9 and 11 nm, respectively for CeO_2, NiO/CeO_2, $CuO\text{-}NiO/CeO_2$ and CuO/CeO_2.

6.3.2. Textural properties of the Cu-Ni (5-5)/CeO_2 system

Table 6.1 shows the textural properties of the catalytic materials obtained from N_2 physi-sorption measurement at 77 K. It showed that doping CeO_2 with copper or nickel results in a slight decrease in the BET surface area. The same effect was observed on the bimetallic samples.

Table 6.1:

Catalyst	Surface area (m_2/g)	Average crystallite size of CeO_2	Lattice parameter (A^o)	Carbon deposit after reaction ($mmole_{Carbon}/g_{cat}$)
CeO_2	**87**	**15**	**5.412**	**-**
10Ni/Ce	**50**	**12**	**5.410**	**0.78**
5Ni5Cu/Ce	**60**	**9**	**5.407**	**0.20**
10Cu/Ce	**55**	**11**	**5.408**	**0.42**

Typical TEM image with backscatter analysis of the as-synthesized Cu-Ni (5-5)/CeO_2 catalyst prepared is present in Fig. 6.4.From the TEM images, the particles of Cu-Ni/CeO_2 catalyst are uniformly distributed. This is expected since the doped Cu could promote the dispersion of Ni metal on the CeO_2 surface, as confirmed by the XRD data. Based on the XRD and TEM results, it may be concluded that Cu-Ni alloy is formed in the catalyst [199].

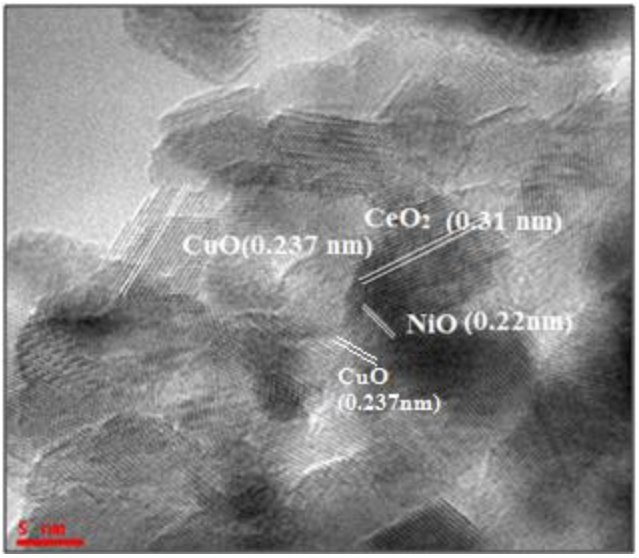

Figure 6.4: TEM of Cu5Ni5Ce

6.3.3. Raman spectra:

Figure 6.5 presents the Raman spectra of various catalysts along with CeO_2 support for comparison. Two distinct peaks at 460 and 588 cm^{-1} are observed for NiO and CuO in addition to CeO_2. It can be seen from Fig.6.5 that the band at 462 $cm^{-1}$was due to F_{2g} Raman active interior phonon mode of CeO_2fluorite structure, whereas, the second band at ca. 588 cm^{-1} is reported to be due to defect-induced D-band that confirms oxygen vacancies. As seen from Fig. 6.5, the peak at 462 $cm^{-1}$is shifted to 458 cm^{-1} for CuO/CeO_2 and NiO/CeO_2, indicating the change in the lattice parameters [73], which is consistent with the lattice parameters calculated from XRD. The most probable interpretation for the shift and broadening of the peaks is the presence of oxygen vacancies, corresponding to a stoichiometry of CeO_{2-x}, confirming the formation of Ni-Ce-O and Cu-Ce-O solid solutions [200-202]. It is known that the substitution of $Cu^{2+}$and $Ni^{+2}$for Ce^{4+} would generate oxygen vacancies around M^{2+}-O-Ce^{4+} in order to maintain charge neutrality. The peak at 462 cm^{-1} became broader, weaker and shifted to 448 $cm^{-1}$for Cu-Ni(5-5)/CeO_2. No bandsat 552 and631 cm^{-1}were observed for NiO species [202]. This means that the substitution of Ni^{2+} for Ce^{4+} inside the CeO_2 structure to form a solid solution.

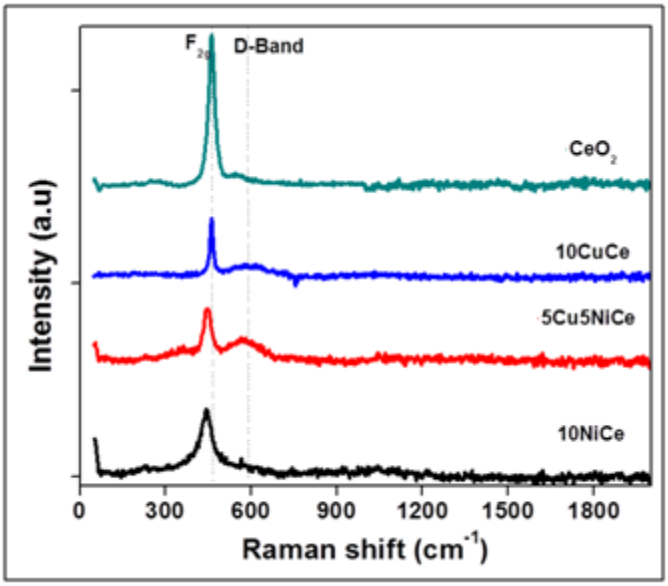

Figure 6.5: Visible Raman spectra of the support and the catalysts excited by 532nm laser.

6.3.4. XPS:

In order to determine the nature of interactions in CuO–NiO/CeO_2 samples, X-ray photoelectron spectra of O1s, Ce3d, Ni2p and Cu2pregions was recorded for CuO–NiO(5-5)/CeO_2 samples(Figure 6.6). The O1s spectrum of CuO–NiO(5-5)/CeO_2 sample in Fig. 6.6aconfirms two peaks at 529 eV and 531 eV which are attributed to lattice O^{2-} ion and surface impurities such asO^{1-}[73, 202]. The Ce3d spectrum in Fig.6.6b shows characteristic V (882.5eV), V'' (888.9eV) and V''' (898.3 eV) lines of Ce3d5/2 and U (900.8 eV), U'' (907.5 eV) and U''' (916.7eV) lines of $Ce3d_{3/2}$ originating from different final states of Ce^{4+} ion [202].There is no indication of Ce^{3+} ion present in the sample.

XPS of Ni $2p_{3/2}$ in Fig. 6.6c shows a well-screened main feature at 855.6 eV due to $2p^5$ $3d^9$ configuration and a poorly screened satellite at 861.1 eV assigned to $2p^5$ $3d^8$excited state configuration [73]. Similarly the Cu_2pspectrum in Fig. 6.6d shows the characteristic spin orbit splitting peaksat 933.7eV and 952.7 eV due to well-screened final state of $2p^5$ $3d^{10}$configuration of Cu^{2+} ion. The poorly screened satellites occurring at 943.3 eVand962.3eV correspond to excited state of$2p^5$ $3d^9$configuration. The binding energy of the $Ni2p_{3/2}$ main peak from CuO–NiO(5-5)/CeO_2 sample is 1.6 eV higher than that of the pure NiO (854 eV). However, such a shift has not occurred in case of $Cu2p_{3/2}$. Here, the presence of

Ni^{3+} due to the formation of $CeNiO_3$ phase is ruled out as this should show considerably higher binding energy in $Ni2p_{3/2}$ spectrum. These observations indicated that the wetting between Ni^{2+} ions and CeO_2 is stronger than that of Cu^{2+}ions and CeO_2. In conclusion, the $Cu^{2+}$and Ce^{4+} ions in CuO–NiO(5-5)/CeO_2sample showcharacteristicCu2pand Ce3d photoemission signatures while Ni^{2+} ions showed a shift in Ni2p spectrum to higher binding energy due to stronger interaction with the support as well as with CuO phase.

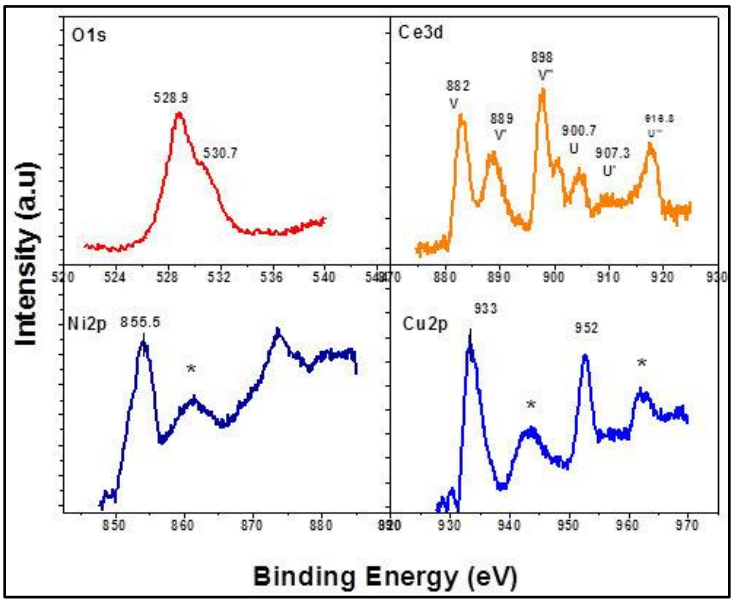

Figure 6.6: O 1s (a), Ce 3d (b), Ni 2p (c) and Cu 2p (d) XPS spectra of the Cu-Ni (5-5)/CeO_2.

6.3.5. Temperature-programmed reduction of the Cu-Ni-base catalysts supported on CeO_2

Temperature programmed reduction (TPR) profiles with hydrogen are shown in Fig.6.7. TPR profile of the bare CeO_2 sample showed a broad peak above 500 °C, which is assigned to the reduction of surface oxygen. Calcined CuO/CeO_2 catalyst showed reduction peaks below 300 °C indicating the presence of different kinds of Cu species [73, 202]. Peaks below 200 °C were attributed due to the reduction of highly dispersed CuO and the peak above 200 °C was due to the reduction of the bulk CuO. The NiO/CeO_2 catalyst showed a sharp reduction peak at around 335°C that may be attributed to the reduction of NiO to metallic Ni crystallites [73].

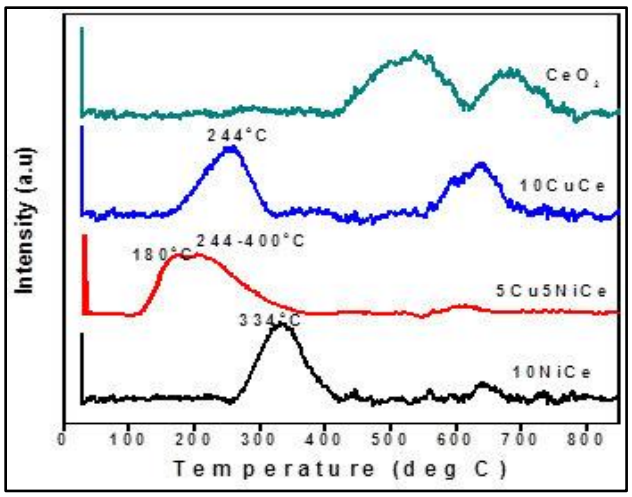

Figure 6.7: H_2-TPR profiles of the catalysts.

TPR profile of the bimetallic catalysts showed the reduction peaks at lower temperature than NiO/CeO_2 catalyst. It has been reported that supported NiO could be reduced at low temperatures in the presence of Cu. Because, Cu causes spill over of hydrogen to Ni that results in simultaneous reduction of both CuO and NiO thereby shifting the reduction peak to low temperatures [202]. This indicates that the bimetallic phase has different interactions with the support and promoted the nickel reduction at lower temperatures.

6.4. Conversion of CH_4, N_2O in NTP-DBD reactor

6.4.1 Effect of feed gas ratio on the conversion of CH_4, N_2O: In order to understand the influence of feed ratio of the reacting gases on the performance of the plasma reactor (Shown in Figure 6.1), mole ratio of CH_4 and N_2O were varied between 5:1, 1:1 and 1:5 (diluted in argon) at a constant gas flow rate of 60 ml/min that corresponds to the gas residence time of 27.2 s with discharge gap of 3.5 mm.The specific energy, measured in kJ/L of feed gas, was varied by changing the applied voltage. As seen from Fig.6.8, at any given SIE, the conversions of CH_4 decreased on increasing the feed ratio, whereas N_2O increased with the increasing CH_4/N_2O feed ratio. At 6 kJ/L, CH_4 conversion was 10, 35 and 45%, whereas N_2Oconversion was 55, 37 and 25%, respectively for feed ratio variation 5:1, 1:1 and 1:5 mole ratios.

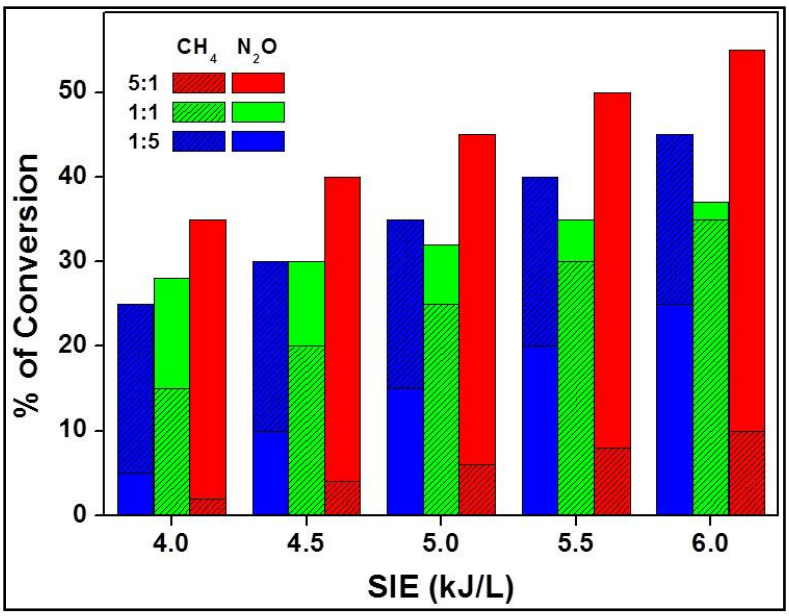

Figure 6.8: Conversion of CH_4 and N_2O during the partial oxidation of CH_4 to CH_3OH in a DBD reactor, flow rate – 60 mL $min^{-1}$and discharge gap – 3.5 mm.

6.4.2. Effects of reactant mole ratio on by-product formation:

In general, it is believed that the generation of the energetic electrons is the initial step in plasma initiated reactions. These electrons may collide and dissociate the reactant gas. Hence, the increasing conversion at higher SIE may be due to the presence of more number of energetic electrons [47, 203]. The selectivity to five main by-products, i.e. CH_3OH, HCHO, H_2, CO and CO_2 for different CH_4/N_2O molar ratios at a SIE 6kJ/L are shown in Fig. 6.9 that presented the selectivity to CH_3OH, HCHO and H_2 decreases, while the selectivity of CO and CO_2 increased on increasing CH_4/N_2O molar ratio. Above tendencies are reasonable, as at CH_4/N_2O-5:1 ratio, more CH_4 molecules are available in the discharge region that may be converted into hydrogen and oxygenated hydrocarbons. The selectivity to methanol was highest (28%) for CH_4/N_2O-5:1 that decreased to 23 and 13% respectively for 1:1 and 1:5 ratios. A similar trend was observed for HCHO and H_2, where the highest selectivity was achieved for CH_4:N_2O-5:1 (18, 46% respectively for HCHO and H_2) that decreased to 13, 36% and 5, 17% for 1:1 and 1:5 feed ratios.

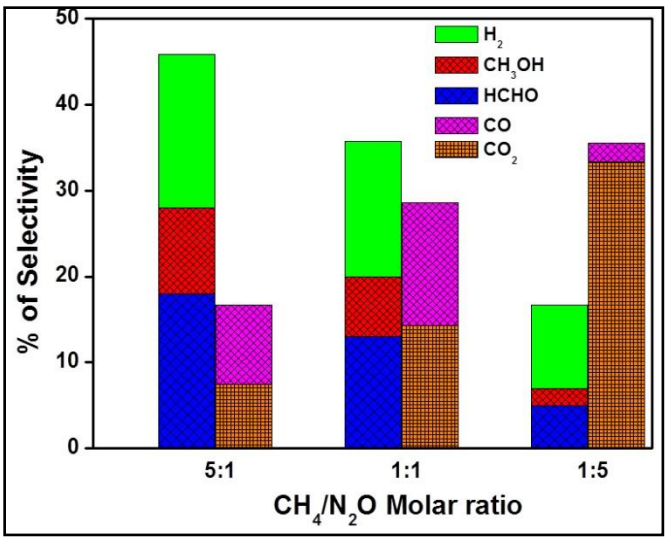

Figure 6.9: Selectivities of H_2,CH_3OH, HCHO, CO and CO_2 during the partial oxidation of CH_4 to CH_3OH in a DBD reactor at SIE – 6kJL^{-1}, flow rate – 60 mL min^{-1} and discharge gap – 3.5 mm.

Figure 6.9 also confirms the best selectivity to deep/total oxidation (selectivity to CO and CO_2) at CH_4/N_2O-1:5 probably due to the formation of highest amount of oxygen by N_2O decomposition. The selectivity of CO was 16% for CH_4/N_2O of 5:1 that increased to 29 and 36% on changing the feed ratio to 1:1 and 1:5. Under the same experimental conditions, CO_2 selectivity was 7.5, 14.5 and 33.5%, respectively. Conversion and selectivity (in moles/L*10^{-2}) at 6 kJ/L for various mole ratios expressed in molar basis as shown in Table 6.2.

Table 6.2: Conversion and Yield (in moles/L*10^{-2}) at 6 kJ/L for various mole ratios

Conversion and Yield	**5:1**	**1:1**	**1:5**
CH_4(in moles/L*10^{-2})	**2.23**	**4.68**	**2.00**
N_2O(in moles/L*10^{-2})	**2.45**	**4.95**	**5.57**
S_{CH3OH}	**0.57**	**0.98**	**0.15**
S_{HCHO}	**0.26**	**0.44**	**0.11**
S_{CO}	**0.39**	**1.33**	**0.71**
S_{CO2}	**0.18**	**0.66**	**0.66**
S_{H2}	**2.00**	**3.34**	**0.66**
S_{carbon}	**1.43**	**3.43**	**1.65**

Figure 6.10 presents the carbon mass balance (to the desired products listed above) at 6kJ/L. Among studied, CH_4/N_2O-1:5 showed best selectivity (up to ~81 %), whereas, 1:1, 5:1 showed slightly

lower values of 75 and 70%. In addition to the main products (CH_3OH, HCHO, H_2, CO and CO_2), formation of other products such as ethane, propane, propene, etc were identified by GCMS, however they were not quantified. Concerning the mechanism of plasma activation of CH_4 and N_2O, many reports deal with the radical processes. The reaction may be initiated by the formation of metal stable argon that reacts with N_2O via energy transfer reactions to produce atomic oxygen, whereas, electron collision reaction of N_2O and CH_4 may form other products like CH_3, CH_2, CH, C_2H, OH and C_2. Reaction of atomic oxygen with methane may form methanol.

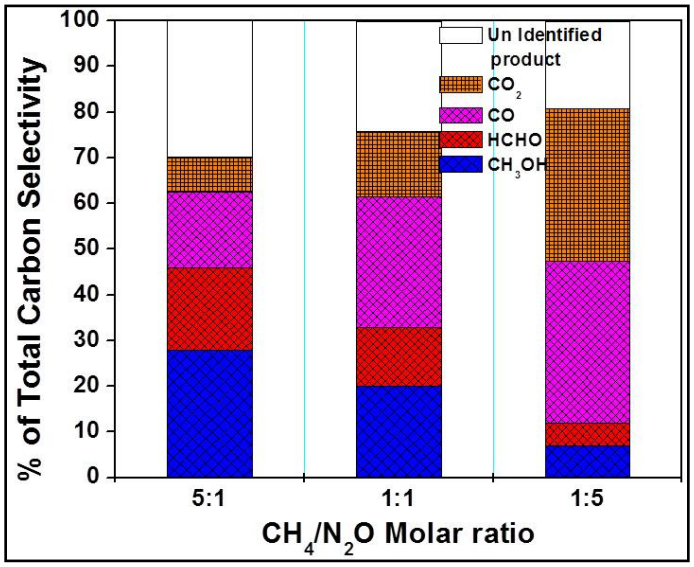

Figure 6.10: Carbon balance during the partial oxidation of CH_4 to CH_3OH in a DBD reactor at SIE – 6kJL^{-1}, flow rate – 60 mL min^{-1} and discharge gap – 3.5 mm.

For 5:1 feed ratio of CH_4 and N_2O, the conversion increased with increasing input power. At 4.5 W input power and discharge length of 15 cm, the rate of conversion of CH_4 and N_2O was $0.87x10^{-6}$ and $2.2x10^{-6}$mol/sec, respectively and the sum of energy efficiency for CH_4 and N_2O decomposition is 37.06%, which is comparable with the data reported by Yaoet.al [204]. The energy efficiency is 10.3% for methanol production and the corresponding energy demand was $1.0x10^7$ J/mol.

6.4.3. Effects of catalyst on CH_4-N_2O conversion:

Figure 6.11 presents the comparative activity of various catalysts for CH_4 and N_2O conversion at the SIE of 6kJ/L at gas flow rate of 60 mL min^{-1}. Nearly 1 g of the catalyst flakes were loaded inside the reactor, and the reaction was carried at a fixed feed ratio of 5:1. Figure 6.11 indicate a high conversion of CH_4 (18%) and N_2O (60%) on addition of 10%NiO/CeO_2 to plasma system at the SIE of 6kJ/L, which increased further to 23% and 65% with Cu-Ni (5-5)/CeO_2. It is worth mentioning that under the same conditions, NiO and plasma alone showed low conversion.

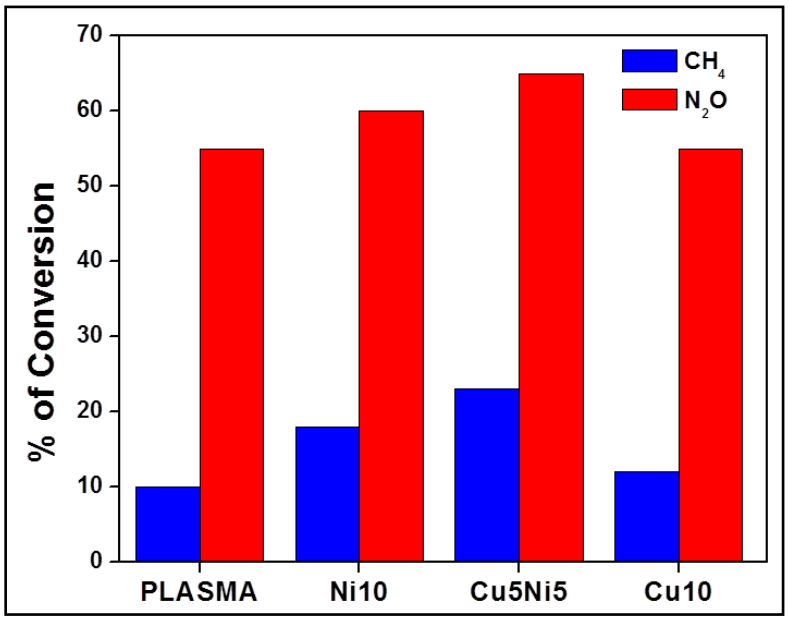

Figure 6.11: Effect of catalyst on the conversion of CH_4 and N_2O during the partial oxidation of CH_4 to CH_3OH in a DBD reactor, flow rate – 60 mL min^{-1} and discharge gap – 3.5 mm.

This is in accordance with Wang, who reported that the addition of Cu to the NiO/CeO_2 catalyst was effective in improving the catalyst activity during methane conversion. With further increasing copper content (10wt% Cu addition to CeO_2), the conversion of CH_4 decreased to 12%, whereas N_2O conversion was ~ 55%. Therefore the order of the catalytic activity of the CeO_2 catalysts followed the trend CuO-NiO (5-5)/CeO_2>NiO (10%)/CeO_2>CuO(10%)/CeO_2~Plasma . From the Raman results (based on the area of the peak from oxygen vacancies), the amount of A_2/A_1 ratio of (Cu/Ni)-O-Ce solid solution also followed the order Cu-Ni/CeO_2>NiO/CeO_2>CuO/CeO_2, indicating that the catalytic activity is related to

the solid solution formation. The increasing amount of lattice oxygen vacancies may facilitate oxygen transfer and facilities the catalytic reaction. The presence of Cu, Ni in the CeO_2 favours the segregation of metallic ions to form CuO clusters on the surface of ceria that increases the ion mobility due to the formation of a Ni-O-Ce solid solution. Incorporating Ni^{2+} into cerium oxide promoted the reducibility of Ce^{4+} (Ni^{2+}) to Ce^{3+} (Ni^{+}) and may enhance the flexibility of copper ions to adapt the oxidation state of Cu^{+} while maintaining the electronic neutrality of the lattice. Another cause would be the substitution of Cu^{2+} for Ce^{4+} in the CeO_2 lattice and the spontaneous transformation of the Ce^{4+} into the larger Ce^{3+}, making this substitution easier due to the similarity of the ion radii of Cu^{+} (r-Cu^{+} = 0.096 nm), Ce^{3+} (r-Ce^{3+} = 0.0103 nm) and Ce^{4+} (r-Ce^{4+} = 0.092 nm), which have the same face centered cubic crystal structure with an octahedral coordination environment [199]. This suggested that adsorbed oxygen can be transformed into lattice oxygen by the introduction of CuO, thus promoting the catalytic activity. This would be due to the presence of Cu^{+} and Ce^{3+}in the catalyst, which favours the formation of oxygen vacancies in the oxide surface.

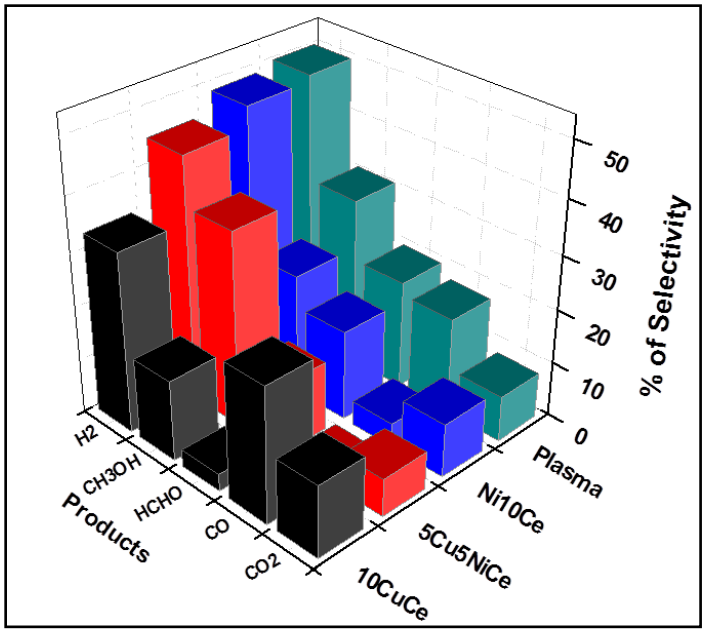

Figure 6.12: Selectivities of H_2,CH_3OH, HCHO, CO and CO_2 during the catalyst effect on partial oxidation of CH_4 to CH_3OH in a DBD reactor at SIE – 6kJL^{-1}, flow rate – 60 mL min^{-1} and discharge gap – 3.5 mm.

6.4.4. Effects of catalyst on by-product formation:

The formation of CH_3OH, H_2, HCHO, CO and CO_2 were measured for both plasma and plasma catalytic system and shown in Fig. 6.12. It has been observed that the CH_3OH selectivity was highest (36%) for Cu-Ni (5-5 wt%)/CeO_2 than remaining systems (NiO/CeO_2-22.2% and CuO/CeO_2-15%) and plasma alone (31%). The Cu-Ni/Ce sample is preferable for methanol synthesis in plasma-catalytic system when compared to NiO/ CeO_2 and CuO/CeO_2 and plasma alone. H_2 and HCHO selectivities followed the order plasma (50 and 20%) >NiO/CeO_2 (49 and 16.6%) > Cu-Ni/CeO_2 (45 and 13%) >CuO/CeO_2 (33 and 3%) respectively. The CO and CO_2 selectivities are highest with CuO/CeO_2 (25 and 13.3%) and plasma alone (17.8 and 8.4%), respectively, whereas NiO/CeO_2 (4.4 and 10%) and Cu-Ni(5-5 wt%)/CeO_2 (2 and 7%) showed lower selectivity than CuO/CeO_2 and the plasma system.

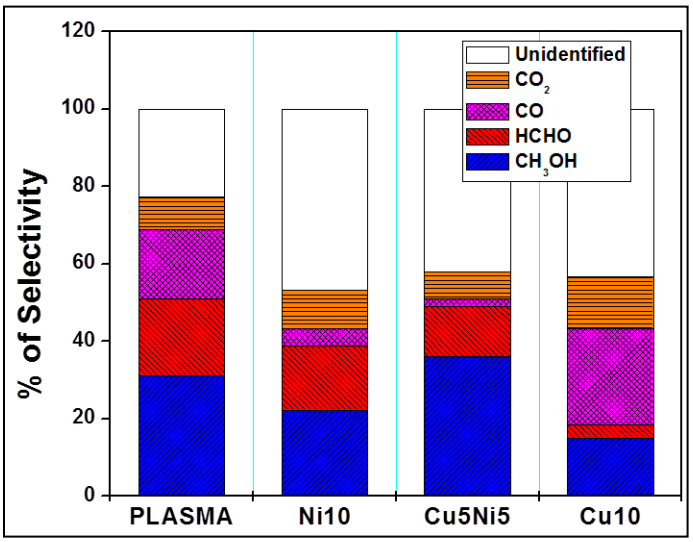

Figure 6.13: Carbon balance during the catalyst effect on partial oxidation of CH_4 to CH_3OH in a DBD reactor at SIE – 6kJL^{-1}, flow rate – 60 mL min^{-1} and discharge gap – 3.5 mm.

It was noticed that the CO selectivity on Cu-Ni/ CeO_2 catalyst decreased rapidly, but the CO_2 selectivity did not change significantly. This result suggested a different pathway other than sequential oxidation, and indicated that Cu-Ni/CeO_2 catalyst was more active for CO reaction than CuO/CeO_2 catalyst. This difference is probably attributed to the presence of active sites on the surface of Cu-Ni/CeO_2 catalyst, which may facilitate CO hydrogenation to produce methanol. CuO doping into the NiO-CeO_2 decreased the activity of the catalyst and facilitates the adsorption of the CO, which gets reduced to form methanol.

Figure 6.13 presents the carbon mass balance (to the products listed above) at 6 kJ /L. Among all the systems studied, the total carbon selectivity follows the order: Plasma alone (77.2%) > Cu-Ni/CeO_2 (58%) >CuO/CeO_2 (56.6%) >NiO/CeO_2 (53.2%). In addition to the above five products, the formation of other by-products was confirmed by GC-MS. Some other higher hydrocarbons were also produced in plasma-catalytic system. Especially C_2H_6, is the main by-product. To ensure that the carbon deposited on the catalyst during the course of the reaction, temperature-programmed oxidation of the spent catalysts was carried out, and results are shown in Fig. 6.14. It is clear from the Fig.6.14 that the carbon deposition was highest for NiO/CeO_2 than CuO/$CeO_2$and Cu-Ni/CeO_2(Table 6.1). It has been observed that the XRD patterns of the spent catalysts remain the same and a small decrease in the surface area of the samples was observed (Table 6.1).

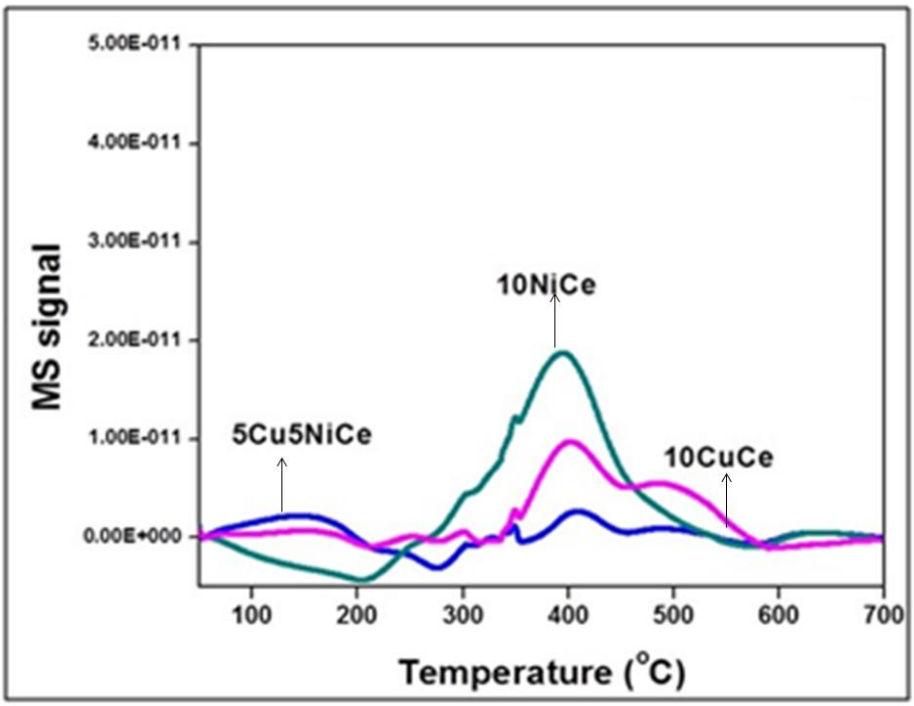

Figure 6.14: Temperature programmed oxidation of spent catalysts.

6.4.5. Reaction mechanism

The decomposition of methane and nitrous oxide mainly takes place in the discharge. Free radical mechanism in nonthermal plasma processes is widely accepted [50, 60,114]. NTP is used to generate high

energy electrons and excited species. These energetic species impact CH_4 and N_2O to generate free radicals or neutrals, positive ions, negative ions, and excited molecules or atoms, through electron impact dissociation and electron ionization–dissociation processes. The collisions of methane molecules with energetic electrons lead to the formation of active radicals such as CH_3^*, CH_2^*, CH^*, C_2H^*, and C_2[109, 113-115]. The main reactions were described as below.

(1) The initial reactions in the plasma reactor may involve the excitation of Ar as follows:

$Ar + e \rightarrow Ar^* + e$……..….. (35)

(2) The initiation of radicals in the discharge channels could be expressed below, in the CH_4/N_2O/Ar system, N_2O and CH_4 can be excited and dissociated as follows:

Electron collision reactions with N_2O:

$Ar^* + N_2O \rightarrow Ar + N_2 + O^*$……..…….. (36)

$N_2O + O^* \rightarrow N_2 + O_2$ ……..……... (37)

$O^* + O^* \rightarrow O_2$……..….. (38)

Electron collision reactions with CH_4:

$Ar^* + CH_4 \rightarrow Ar + CH_3^* + H^*$ ……..…..….. (39)

$Ar^* + CH_3^* \rightarrow Ar + CH_2^* + H^*$ ……...….. (40)

$Ar^* + CH_2^* \rightarrow Ar + CH^* + H^*$ ……..….. (41)

(3) The product selectivity may be explained by the following radical mechanism

$H^* + H^* \rightarrow H_2$……..……. (42)

$CH_3^* + O^* \rightarrow CH_3O^*$……...…….. (43)

$CH_3O^* + H^* \rightarrow CH_3OH$..…….(44)

$CH_3O^* + CH_4 \rightarrow CH_3OH + CH_3^*$……..…… (45)

$CH_3^* + (O^*, O_2, OH^*) \rightarrow HCHO + (H^*, OH^*, H_2)$….. (46)

$CH_4 + CH_3O^* \rightarrow CH_3^* + CH_3OH$……..…….. (47)

$CH_2OH^* + (O_2, H) \rightarrow HCHO + (HO_2^*, H_2)$……..….. (48)

$HCHO + (H^*, OH^*) \rightarrow HCO^* + (H_2, H_2O)$…….. (49)

$CH_x + O^* \rightarrow CO + xH^*$……...…….. (50)

$HCO^* \rightarrow H^* + CO$……..……... (51)

$HCO^* + OH^* \rightarrow CO + 2OH^*$……....…… (52)

$HCO^* + O^* \rightarrow CO + OH^*$……..……... (53)

$CO + O^* \rightarrow CO_2$……..…….. (54)

$CO + OH^* \rightarrow CO_2 + H^*$……..…….. (55)

$CO_2 + (H^*, OH^*) \rightarrow CO + (OH^*, H_2O)$……..……..(56)

6.5. Conclusions

A dielectric barrier discharge reactor was used for co-processing methane and nitrous oxide. Typical results indicated that nonthermal plasma provides an advantage of in-situ decomposition of N_2O to N_2 and atomic oxygen that was used for *in-situ* conversion of methane into value added products like CH_3OH, HCHO, H_2, CO and CO_2. The conversion of the reactants and product selectivity varies significantly on changing the mole ratio of the reactants. At CH_4/N_2O of 5:1, the selectivity to CH_3OH was 28% and for HCHO, it was 18%. The same feed ratio also favored the high selectivity to methanol

and formaldehyde, whereas the feed ratio of 1:5 favored the deep oxidation. Further the same reaction was investigated in the presence of catalysts like CuO/CeO_2, NiO/CeO_2 and Cu-Ni (5-5)/CeO_2 added to NTP. Among the studied catalysts, Cu-Ni (5:5 wt%) containing ceria was found to show the best selectivity for methanol and syngas.

CHAPTER7

Summary and Conclusions

The direct decomposition of GHGs into value added products has been studied in a non-thermal plasma dielectric barrier discharge reactor. The present study investigated the energy consumption and the effectiveness of NTP technique in order to understand the feasibility of the process. The general conclusions of the present study may be summarized as follows:

- Plasma-assisted simultaneous splitting of water and CO_2 for syngas synthesis along with co-generation of CNFs was studied in a DBD plasma reactor. The characterization of catalysts confirmed by TEM, Raman, XRD and TPO techniques. CO_2 conversion decreased with decreasing residence time (RT). The reactor with partially reduced catalyst ($Ni/\gamma\text{-}Al_2O_3$) showed better CO_2 conversion than the unreduced $NiO/\gamma\text{-}Al_2O_3$ and with no catalyst (plasma alone).
- Direct decomposition of nitrous oxide into N_2 and O_2 in the presence of Ar gas was studied in a nonthermal plasma dielectric barrier discharge (DBD) reactor operated under ambient conditions. Typical results indicated that even though high residence time favoured high conversion; it also demands high input energy. Hence, for the practical applications, high concentration and low residence time are preferred. By optimizing the reaction conditions, close to 100% N_2O decomposition was achieved at 1.6 W. The performance of the DBD rector was found to increase on addition of NiO/CeO_2 catalyst that may be assigned due to the presence of oxygen vacancies on the surface of the catalyst that stabilize the atomic oxygen formed during CO oxidation by N_2O decomposition.
- Dry reforming of methane with carbon dioxide was carried out in a nonthermal plasma reactor operated in a dielectric barrier discharge configuration. Influence of composition of the reactants in the feed was investigated at room temperature, at a constant feed flow rate 40 mL/min and with the voltage variation between 12 to 26 kV. With decreasing CH_4/CO_2 mole ratio, both CH_4 and CO_2 conversion increases gradually. Consequently, the selectivity to CO and H_2 and H_2/CO ratio

in the synthesis gas increased. The specific energy demand depends on the mole ratio of the reactants and it followed the trend 1:2>1:1>2:1 for CH_4:CO_2. It was observed that H_2/CO ratio was only 1.2 with plasma reactor alone. In order to improve the performance of the DBD reactor, Ni catalysts were prepared by combustion synthesis and 10% of the active discharge volume was packed with catalysts. Typical results indicated the improved performance of the reactor for dilute mixtures and addition of Ni/Al_2O_3 catalysts. Among the catalysts studied, 20% Ni/Al_2O_3 showed the best conversion and highest H_2/CO ratio of 2.25 against 1.2 with plasma reactor alone. The adsorption, desorption and reaction of Ni catalyst under plasmas is still new. However, the better catalytic behavior of 20% Ni/Al_2O_3 catalyst in the dry reforming of methane may be due to the formation of nanocrystalline $NiAl_2O_4$, highly dispersed Ni nanoparticles and/or due to high reducibility as compared to higher or lower wt% of Ni.

- A dielectric barrier discharge reactor was also used for co-processing methane and nitrous oxide. The conversion of the reactants and product selectivity varies significantly on changing the mole ratio of the reactants. The feed ratio of 5:1 favours the high selectivity to methanol and formaldehyde, whereas the feed ratio of 1:5 favors the deep oxidation. Further the partial oxidation of methane with nitrous oxide under non thermal plasma dielectric barrier discharge reactor was investigated in the presence of catalysts like CuO/CeO_2, NiO/CeO_2 and Cu-Ni (5-5)/CeO_2 that were prepared by solution combustion synthesis. Among the studied catalysts, Cu-Ni (5:5 wt%) containing ceria, was found to show the best selectivity for the partial oxidation of methane to methanol and syngas. The overall conclusion is that we convert greenhouse gases to value added products (H_2, CH_3OH, HCHO, syngas ect.) by using catalytic non-thermal plasma reactor. Even though catalytic NTP reactor developed in this study has the promise during the activation of GHGs, there is a need to understand the nature of the species formed, especially in the presence of the catalyst, for large scale applications. At present, these reactions are not energetically feasible and further studies are needed to improve the energy efficiency.

References:

[1] L.F. Liotta, G. Pantaleo, F. Puleo and A.M. Venezia. Au/CeO2-SBA-15 catalysts for CO oxidation: Effect of ceria loading on physic-chemical properties and catalytic performances. Catalysis Today.
[2] F. Boccuzzi, A. Chiorino, M. Manzoli, P. Lu, T. Akita, S. Ichikawa and M. Haruta. Au/TiO2 Nanosized Samples: A Catalytic, TEM, and FTIR Study of the Effect of Calcination Temperature on the CO Oxidation. Journal of Catalysis 202, (2001) 256-267.
[3] K.C. Chou, N.M. Markovic, J. Kim, P.N. Ross and G.A. Somorjai. An in Situ Time-Dependent Study of CO Oxidation on Pt(111) in Aqueous Solution by Voltammetry and Sum Frequency Generation. The Journal of Physical Chemistry B 107, (2003) 1840-1844.
[4] M. Haruta, N. Yamada, T. Kobayashi and S. Iijima. J. Catal. 115, (1989) 301.
[5] B.E. Hayden, D. Pletcher, M.E. Rendall and J.-P. Suchsland. CO Oxidation on Gold in Acidic Environments: Particle Size and Substrate Effects. The Journal of Physical Chemistry C 111, (2007) 17044-17051.
[6] S. Hoffer, S. Baldelli, K. Chou, P. Ross and G.A. Somorjai. CO Oxidation on Electrified Platinum Surfaces in Acetonitrile/Water Solutions Studied by Sum Frequency Generation and Cyclic Voltammetry. The Journal of Physical Chemistry B 106, (2002) 6473-6478.
[7] S. Jia, C.-H. Hsia and D.H. Son. In Situ Study of Room-Temperature Oxidation Kinetics of Colloidal Co Nanocrystals Investigated by Faraday Rotation Measurement. The Journal of Physical Chemistry C 115, (2010) 92-96.
[8] J.-Y. Luo, M. Meng, Y.-Q. Zha and L.-H. Guo. Identification of the Active Sites for CO and C3H8 Total Oxidation over Nanostructured CuO−CeO2 and Co3O4−CeO2 Catalysts. The Journal of Physical Chemistry C 112, (2008) 8694-8701.
[9] G. Samjeské, K.-i. Komatsu and M. Osawa. Dynamics of CO Oxidation on a Polycrystalline Platinum Electrode: A Time-Resolved Infrared Study. The Journal of Physical Chemistry C 113, (2009) 10222-10228.
[10] H. Wang, L.-F. Cui, Y. Yang, H. Sanchez Casalongue, J.T. Robinson, Y. Liang, Y. Cui and H. Dai. Mn3O4−Graphene Hybrid as a High-Capacity Anode Material for Lithium Ion Batteries. Journal of the American Chemical Society 132, (2010) 13978-13980.
[11] T. Roy Choudhury, T. Padmanabhan and R. Srianand. Semi-analytic approach to understanding the distribution of neutral hydrogen in the Universe. Monthly Notices of the Royal Astronomical Society 322, (2001) 561-575.
[12] T.R. Choudhury, R. Srianand and T. Padmanabhan. Semianalytic Approach to Understanding the Distribution of Neutral Hydrogen in the Universe: Comparison of Simulations with Observations. The Astrophysical Journal 559, (2001) 29.
[13] S.S. Bharadwaj and L.D. Schmidt. Catalytic partial oxidation of natural gas to syngas. Fuel Processing Technology 42, (1995) 109-127.
[14] A. Czernichowski and P. Czernichowski, Electrically assisted partial oxidation of light hydrocarbons by oxygen, in, Google Patents, 1999.
[15] M.A. Escobedo Bretado, M.D. Delgado Vigil, J.S. Gutiérrez, A. López Ortiz and V. Collins-Martínez. Hydrogen production by absorption enhanced water gas shift (AEWGS). International Journal of Hydrogen Energy 35, (2010) 12083-12090.
[16] J. Rostrup-Nielsen, Catalytic steam reforming in Catalysis science and technology. JR Anderson and M. Boudart, Editors, in, Springer-Verlag: Berlin, 1984.
[17] S.C. Tsang, J.B. Claridge and M.L.H. Green. Recent advances in the conversion of methane to synthesis gas. Catalysis Today 23, (1995) 3-15.
[18] J.R. Rostrup-Nielsen. Production of synthesis gas. Catalysis Today 18, (1993) 305-324.
[19] J. Rostrup-Nielsen. 40 years in catalysis. Catalysis Today 111, (2006) 4-11.
[20] J.R. Rostrup-Nielsen, Aspects of CO2-reforming of Methane, in: H.E. Curry-Hyde, R.F. Howe (Eds.) Studies in Surface Science and Catalysis, Elsevier, 1994, pp. 25-41.
[21] J.R. Rostrup-Nielsen. Syngas in perspective. Catalysis Today 71, (2002) 243-247.

[22] M. Fathi, E. Bjorgum, T. Viig and O.A. Rokstad. Partial oxidation of methane to synthesis gas:: Elimination of gas phase oxygen. Catalysis Today 63, (2000) 489-497.
[23] J.N. Armor. The multiple roles for catalysis in the production of H2. Applied Catalysis A: General 176, (1999) 159-176.
[24] Z.X. Cheng, X.G. Zhao, J.L. Li and Q.M. Zhu. Role of support in CO2 reforming of CH4 over a Ni/γ-Al2O3 catalyst. Applied Catalysis A: General 205, (2001) 31-36.
[25] J.H. Edwards and A.M. Maitra. The chemistry of methane reforming with carbon dioxide and its current and potential applications. Fuel Processing Technology 42, (1995) 269-289.
[26] R. Levitan, M. Levy, H. Rosin and R. Rubin. Closed-loop operation of a solar chemical heat pipe at the Weizmann Institute solar furnace. Solar Energy Materials 24, (1991) 464-477.
[27] P. Ferreira-Aparicio, M.J. Benito and J.L. Sanz. New Trends in Reforming Technologies: from Hydrogen Industrial Plants to Multifuel Microreformers. Catalysis Reviews 47, (2005) 491-588.
[28] J. Luche, O. Aubry, A. Khacef and J.-M. Cormier. Syngas production from methane oxidation using a non-thermal plasma: Experiments and kinetic modeling. Chemical Engineering Journal 149, (2009) 35-41.
[29] A. Steinfeld and R. Palumbo, Solar Thermochemical Process Technology, in: R.A. Meyers (Ed.) Encyclopedia of Physical Science and Technology (Third Edition), Academic Press, New York, 2003, pp. 237-256.
[30] J.J. Vargo. Clinical applications of the argon plasma coagulator. Gastrointestinal Endoscopy 59, (2004) 81-88.
[31] B. Eliasson and U. Kogelschatz. Nonequilibrium volume plasma chemical processing. Plasma Science, IEEE Transactions on 19, (1991) 1063-1077.
[32] L. Tonks. The Birth of "Plasma". American Journal of Physics 35, (1967) 857-858.
[33] X. Hu, G. Li and J.C. Yu. Design, Fabrication, and Modification of Nanostructured Semiconductor Materials for Environmental and Energy Applications. Langmuir 26, (2009) 3031-3039.
[34] M. Cooper, G. Fridman, A. Fridman and S.G. Joshi. Biological responses of Bacillus stratosphericus to Floating Electrode-Dielectric Barrier Discharge Plasma Treatment. Journal of Applied Microbiology 109, (2010) 2039-2048.
[35] H. Conrads and M. Schmidt. Plasma generation and plasma sources. Plasma Sources Science and Technology 9, (2000) 441.
[36] K.A. Fenlon, K.C. Jones and K.T. Semple. The effect of soil:water ratios on the induction of isoproturon, cypermethrin and diazinon mineralisation. Chemosphere 82, (2011) 163-168.
[37] L.B. Marks, X. Yu, Z. Vujaskovic, W. Small Jr, R. Folz and M.S. Anscher. Radiation-induced lung injury. Seminars in Radiation Oncology 13, (2003) 333-345.
[38] D. Hegemann, M.M. Hossain, E. Körner and D.J. Balazs. Macroscopic Description of Plasma Polymerization. Plasma Processes and Polymers 4, (2007) 229-238.
[39] A. Meiners, M. Leck and B. Abel. Multiple parameter optimization and spectroscopic characterization of a dielectric barrier discharge in N 2. Plasma Sources Science and Technology 18, (2009) 045015.
[40] J. Chang, x, Shih, P.A. Lawless and T. Yamamoto. Corona discharge processes. Plasma Science, IEEE Transactions on 19, (1991) 1152-1166.
[41] H.-H. Kim. Nonthermal Plasma Processing for Air-Pollution Control: A Historical Review, Current Issues, and Future Prospects. Plasma Processes and Polymers 1, (2004) 91-110.
[42] S.U. Kalghatgi, G. Fridman, M. Cooper, G. Nagaraj, M. Peddinghaus, M. Balasubramanian, V.N. Vasilets, A.F. Gutsol, A. Fridman and G. Friedman. Mechanism of Blood Coagulation by Nonthermal Atmospheric Pressure Dielectric Barrier Discharge Plasma. Plasma Science, IEEE Transactions on 35, (2007) 1559-1566.
[43] J. Karuppiah, L. Sivachrandiran, R. Karvembu and C. Subrahmanyam. Catalytic Plasma Reactor for Abatement of Dilute Nitrobenzene. Chinese Journal of Catalysis 32, (2011) 795-799.
[44] U. Kogelschatz. Filamentary, patterned, and diffuse barrier discharges. Plasma Science, IEEE Transactions on 30, (2002) 1400-1408.

[45] C.L. Enloe, T. McLaughlin, G.I. Font and J.W. Baughn. Parameterization of Temporal Structure in the Single-Dielectric-Barrier Aerodynamic Plasma Actuator. AIAA Journal 44, (2006) 1127-1136.
[46] T. von Woedtke, S. Reuter, K. Masur and K.D. Weltmann. Plasmas for medicine. Physics Reports 530, (2013) 291-320.
[47] E. Linga Reddy, V.M. Biju and C. Subrahmanyam. Production of hydrogen and sulfur from hydrogen sulfide assisted by nonthermal plasma. Applied Energy 95, (2012) 87-92.
[48] X. Tu, H.J. Gallon, M.V. Twigg, P.A. Gorry and J.C. Whitehead. Dry reforming of methane over a Ni/Al 2 O 3 catalyst in a coaxial dielectric barrier discharge reactor. Journal of Physics D: Applied Physics 44, (2011) 274007.
[49] H.J. Gallon, X. Tu and J.C. Whitehead. Effects of Reactor Packing Materials on H2 Production by CO2 Reforming of CH4 in a Dielectric Barrier Discharge. Plasma Processes and Polymers 9, (2012) 90-97.
[50] H.J. Gallon, X. Tu, M.V. Twigg and J.C. Whitehead. Plasma-assisted methane reduction of a NiO catalyst—Low temperature activation of methane and formation of carbon nanofibres. Applied Catalysis B: Environmental 106, (2011) 616-620.
[51] M.O. Adebajo. Green chemistry perspectives of methane conversion via oxidative methylation of aromatics over zeolite catalysts. Green Chemistry 9, (2007) 526-539.
[52] C.L. McMullin, A.W. Pierpont and T.R. Cundari. Complete methane-to-methanol catalytic cycle: A DFT study of oxygen atom transfer from N2O to late-row (MNi, Cu, Zn) β-diketiminate CH activation catalysts. Polyhedron 52, (2013) 945-956.
[53] S.M. Starikovskaia. Plasma assisted ignition and combustion. Journal of Physics D: Applied Physics 39, (2006) R265.
[54] G. Lou, A. Bao, M. Nishihara, S. Keshav, Y.G. Utkin, J.W. Rich, W.R. Lempert and I.V. Adamovich. Ignition of premixed hydrocarbon–air flows by repetitively pulsed, nanosecond pulse duration plasma. Proceedings of the Combustion Institute 31, (2007) 3327-3334.
[55] N.B. Anikin, S.M. Starikovskaia and A.Y. Starikovskii. Study of the oxidation of alkanes in their mixtures with oxygen and air under the action of a pulsed volume nanosecond discharge. Plasma Physics Reports 30, (2004) 1028-1042.
[56] T. Ombrello, X. Qin, Y. Ju, A. Gutsol, A. Fridman and C. Carter. Combustion Enhancement via Stabilized Piecewise Nonequilibrium Gliding Arc Plasma Discharge. AIAA Journal 44, (2006) 142-150.
[57] C. Subrahmanyam, M. Magureanu, A. Renken and L. Kiwi-Minsker. Catalytic abatement of volatile organic compounds assisted by non-thermal plasma: Part 1. A novel dielectric barrier discharge reactor containing catalytic electrode. Applied Catalysis B: Environmental 65, (2006) 150-156.
[58] J. Karuppiah, R. Karvembu and C. Subrahmanyam. The catalytic effect of MnOx and CoOx on the decomposition of nitrobenzene in a non-thermal plasma reactor. Chemical Engineering Journal 180, (2012) 39-45.
[59] E.L. Reddy, V.M. Biju and C. Subrahmanyam. Hydrogen production from hydrogen sulfide in a packed-bed DBD reactor. International Journal of Hydrogen Energy 37, (2012) 8217-8222.
[60] S. Mahammadunnisa, E.L. Reddy, P.R.M.K. Reddy and C. Subrahmanyam. A Facile Approach for Direct Decomposition of Nitrous Oxide Assisted by Non-Thermal Plasma. Plasma Processes and Polymers 10, (2013) 444-450.
[61] M. Magureanu, N.B. Mandache, V.I. Parvulescu, C. Subrahmanyam, A. Renken and L. Kiwi-Minsker. Improved performance of non-thermal plasma reactor during decomposition of trichloroethylene: Optimization of the reactor geometry and introduction of catalytic electrode. Applied Catalysis B: Environmental 74, (2007) 270-277.
[62] U. Kogelschatz. Dielectric-Barrier Discharges: Their History, Discharge Physics, and Industrial Applications. Plasma Chemistry and Plasma Processing 23, (2003) 1-46.
[63] V.I. Gibalov, J. Dřímal, M. Wronski and V.G. Samoilovich. Barrier Discharge The Transferred Charge and Ozone Synthesis. Contributions to Plasma Physics 31, (1991) 89-99.
[64] J.R. Conder and J.H. Purnell. Gas chromatography at finite concentrations. Part 2.-A generalised retention theory. Transactions of the Faraday Society 64, (1968) 3100-3111.

[65] J.C. Giddings. Theory of Minimum Time Operation in Gas Chromatography. Analytical Chemistry 34, (1962) 314-319.
[66] S. Sorge and T. Pechstein. Fully integrated thermal conductivity sensor for gas chromatography without dead volume. Sensors and Actuators A: Physical 63, (1997) 191-195.
[67] P. Gallezot, X-Ray Techniques in Catalysis, in: J. Anderson, M. Boudart (Eds.) Catalysis, Springer Berlin Heidelberg, 1984, pp. 221-273.
[68] R. Lamber, N. Jaeger and G. Schulz-Ekloff. Electron microscopy study of the interaction of Ni, Pd and Pt with carbon: I. Nickel catalyzed graphitization of amorphous carbon. Surface Science 197, (1988) 402-414.
[69] A.W. Aylor, L.J. Lobree, J.A. Reimer and A.T. Bell. Investigations of the Dispersion of Pd in H-ZSM-5. Journal of Catalysis 172, (1997) 453-462.
[70] B.M. Weckhuysen and R.A. Schoonheydt. Recent progress in diffuse reflectance spectroscopy of supported metal oxide catalysts. Catalysis Today 49, (1999) 441-451.
[71] P.J. Cumpson. Angle-resolved XPS and AES: Depth-resolution limits and a general comparison of properties of depth-profile reconstruction methods. Journal of Electron Spectroscopy and Related Phenomena 73, (1995) 25-52.
[72] D.A.M. Monti and A. Baiker. Temperature-programmed reduction. Parametric sensitivity and estimation of kinetic parameters. Journal of Catalysis 83, (1983) 323-335.
[73] S. Mahammadunnisa, P. Manoj Kumar Reddy, N. Lingaiah and C. Subrahmanyam. NiO/Ce1-xNixO2-[small delta] as an alternative to noble metal catalysts for CO oxidation. Catalysis Science & Technology 3, (2013) 730-736.
[74] F. Gal, M. Brach, G. Braibant, C. Bény and K. Michel. What can be learned from natural analogue studies in view of CO2 leakage issues in Carbon Capture and Storage applications? Geochemical case study of Sainte-Marguerite area (French Massif Central). International Journal of Greenhouse Gas Control 10, (2012) 470-485.
[75] P. Zapp, A. Schreiber, J. Marx, M. Haines, J.-F. Hake and J. Gale. Overall environmental impacts of CCS technologies—A life cycle approach. International Journal of Greenhouse Gas Control 8, (2012) 12-21.
[76] J.R. Rostrup-Nielsen. New aspects of syngas production and use. Catalysis Today 63, (2000) 159-164.
[77] J.A. Turner. Sustainable Hydrogen Production. Science 305, (2004) 972-974.
[78] P. Furler, J.R. Scheffe and A. Steinfeld. Syngas production by simultaneous splitting of H2O and CO2via ceria redox reactions in a high-temperature solar reactor. Energy & Environmental Science 5, (2012) 6098-6103.
[79] A. Le Gal, S. Abanades and G. Flamant. CO2 and H2O Splitting for Thermochemical Production of Solar Fuels Using Nonstoichiometric Ceria and Ceria/Zirconia Solid Solutions. Energy & Fuels 25, (2011) 4836-4845.
[80] C. Perkins and A.W. Weimer. Likely near-term solar-thermal water splitting technologies. International Journal of Hydrogen Energy 29, (2004) 1587-1599.
[81] A. Steinfeld. Solar thermochemical production of hydrogen - A review. Solar Energy 78, (2005) 603-615.
[82] W.C. Chueh, C. Falter, M. Abbott, D. Scipio, P. Furler, S.M. Haile and A. Steinfeld. High-Flux Solar-Driven Thermochemical Dissociation of CO2 and H2O Using Nonstoichiometric Ceria. Science 330, (2010) 1797-1801.
[83] P.S. Georgilakis. Technical challenges associated with the integration of wind power into power systems. Renewable and Sustainable Energy Reviews 12, (2008) 852-863.
[84] S.H. Jensen, P.H. Larsen and M. Mogensen. Hydrogen and synthetic fuel production from renewable energy sources. International Journal of Hydrogen Energy 32, (2007) 3253-3257.
[85] C.M. Stoots, J.J. Hartvigsen, J.E. O'Brien and J.S. Herring. Syngas Production via High-Temperature Coelectrolysis of Steam and Carbon Dioxide. Journal of Fuel Cell Science and Technology 6, (2008) 011014-011014.

[86] C. Stoots, J. O'Brien and J. Hartvigsen. Results of recent high temperature coelectrolysis studies at the Idaho National Laboratory. International Journal of Hydrogen Energy 34, (2009) 4208-4215.
[87] Z. Zhan, W. Kobsiriphat, J.R. Wilson, M. Pillai, I. Kim and S.A. Barnett. Syngas Production By Coelectrolysis of CO2/H2O: The Basis for a Renewable Energy Cycle. Energy & Fuels 23, (2009) 3089-3096.
[88] B. Kumar, J.M. Smieja, A.F. Sasayama and C.P. Kubiak. Tunable, light-assisted co-generation of CO and H2 from CO2 and H2O by Re(bipy-tbu)(CO)3Cl and p-Si in non-aqueous medium. Chemical Communications 48, (2012) 272-274.
[89] C.-S. Chen, J.-H. Lin, A.-S. Lin, H.-T. Huang and H.-L. Ma. Synthesis of carbon nanofiber from catalytic hydrogenation of CO2 over Ni–K/Al2O3 catalysts. Carbon 46, (2008) 369-371.
[90] C.S. Chen, J.H. Lin, J.H. You and K.H. Yang. Effects of Potassium on Ni−K/Al2O3 Catalysts in the Synthesis of Carbon Nanofibers by Catalytic Hydrogenation of CO2†. The Journal of Physical Chemistry A 114, (2009) 3773-3781.
[91] K.Y. Koo, H.-S. Roh, Y.T. Seo, D.J. Seo, W.L. Yoon and S.B. Park. Coke study on MgO-promoted Ni/Al2O3 catalyst in combined H2O and CO2 reforming of methane for gas to liquid (GTL) process. Applied Catalysis A: General 340, (2008) 183-190.
[92] M. Benoit, A. Rodrigues, Q. Zhang, E. Fourré, K. De Oliveira Vigier, J.-M. Tatibouët and F. Jérôme. Depolymerization of Cellulose Assisted by a Nonthermal Atmospheric Plasma. Angewandte Chemie International Edition 50, (2011) 8964-8967.
[93] G. Centi and F. Vazzana. Selective catalytic reduction of N2O in industrial emissions containing O2, H2O and SO2: behavior of Fe/ZSM-5 catalysts. Catalysis Today 53, (1999) 683-693.
[94] M.H. THIEMENS and W.C. TROGLER. Nylon Production: An Unknown Source of Atmospheric Nitrous Oxide. Science 251, (1991) 932-934.
[95] Y. Li and J.N. Armor. Catalytic decomposition of nitrous oxide on metal exchanged zeolites. Applied Catalysis B: Environmental 1, (1992) L21-L29.
[96] Y. Li and J.N. Armor. Selective catalytic reduction of NOx with methane over metal exchange zeolites. Applied Catalysis B: Environmental 2, (1993) 239-256.
[97] M. Galle, D.W. Agar and O. Watzenberger. Thermal N2O decomposition in regenerative heat exchanger reactors. Chemical Engineering Science 56, (2001) 1587-1595.
[98] T. Atabarut and E. Ekinci. Thermal Treatment of Landfill Leachate and the Emission Control. Journal of Environmental Science and Health, Part A 41, (2006) 1931-1942.
[99] S. Kameoka, T. Suzuki, K. Yuzaki, T. Takeda, S. Tanaka, S. Ito, T. Miyadera and K. Kunimori. Selective catalytic reduction of N2O with methane in the presence of excess oxygen over Fe-BEA zeolite. Chemical Communications (2000) 745-746.
[100] H. Jiang, H. Wang, F. Liang, S. Werth, T. Schiestel and J. Caro. Direct Decomposition of Nitrous Oxide to Nitrogen by In Situ Oxygen Removal with a Perovskite Membrane. Angewandte Chemie International Edition 48, (2009) 2983-2986.
[101] S. Liu, Y. Cong, Y. Huang, X. Zhao and T. Zhang. TiO2 promoted Ir/Al2O3 catalysts for direct decomposition of N2O. Catalysis Today 175, (2011) 264-270.
[102] D.V. Zatsepin, S.M. Starikovskaya and A.Y. Starikovskii. Nonthermal decomposition of nitrous oxide in a high-current pulsed discharge. Plasma Physics Reports 29, (2003) 517-527.
[103] S.M. Starikovskaia, N.B. Anikin, S.V. Pancheshnyi, D.V. Zatsepin and A.Y. Starikovskii. Pulsed breakdown at high overvoltage: development, propagation and energy branching. Plasma Sources Science and Technology 10, (2001) 344.
[104] T. Tamura, Y. Kaburaki, R. Sasaki, H. Miyahara and A. Okino. Direct Decomposition of Anesthetic Gas Exhaust Using Atmospheric Pressure Multigas Inductively Coupled Plasma. Plasma Science, IEEE Transactions on 39, (2011) 1684-1688.
[105] K. Krawczyk. Conversion of Nitrous Oxide by Positive Pulsed Corona Discharge. Plasma Science, IEEE Transactions on 37, (2009) 884-889.

[106] M. Tsuji, J. Kumagae, K. Nakano, T. Matsuzaki and T. Tsuji. Decomposition of N2O in a microwave-absorbent assisted discharge of N2 at atmospheric pressure. Applied Surface Science 217, (2003) 134-148.
[107] K. Krawczyk, M. Drozdowski and K. Naperty. Nitrous oxide processing by a combination of gliding and microwave discharges. Catalysis Today 119, (2007) 239-242.
[108] J.M. Austin and A.L.S. Smith. Decomposition of N 2 O in a glow discharge. Journal of Physics D: Applied Physics 6, (1973) 2236.
[109] G.-B. Zhao, M.D. Argyle and M. Radosz. Effect of CO on NO and N2O conversions in nonthermal argon plasma. Journal of Applied Physics 99, (2006) -.
[110] X. Hu, J. Nicholas, J.-J. Zhang, T.M. Linjewile, P.d. Filippis and P.K. Agarwal. The destruction of N2O in a pulsed corona discharge reactor. Fuel 81, (2002) 1259-1268.
[111] U. Roland, F. Holzer, A. Pöppl and F.D. Kopinke. Combination of non-thermal plasma and heterogeneous catalysis for oxidation of volatile organic compounds: Part 3. Electron paramagnetic resonance (EPR) studies of plasma-treated porous alumina. Applied Catalysis B: Environmental 58, (2005) 227-234.
[112] W.-J. Liang, H.-P. Fang, J. Li, F. Zheng, J.-X. Li and Y.-Q. Jin. Performance of non-thermal DBD plasma reactor during the removal of hydrogen sulfide. Journal of Electrostatics 69, (2011) 206-213.
[113] S. Futamura, A. Zhang, H. Einaga and H. Kabashima. Involvement of catalyst materials in nonthermal plasma chemical processing of hazardous air pollutants. Catalysis Today 72, (2002) 259-265.
[114] G.-B. Zhao, X. Hu, M.D. Argyle and M. Radosz. Effect of CO2 on Nonthermal-Plasma Reactions of Nitrogen Oxides in N2. 2. Percent-Level Concentrations. Industrial & Engineering Chemistry Research 44, (2005) 3935-3946.
[115] G.-B. Zhao, X. Hu, M.D. Argyle and M. Radosz. Effect of CO2 on Nonthermal-Plasma Reactions of Nitrogen Oxides in N2. 1. PPM-Level Concentrations. Industrial & Engineering Chemistry Research 44, (2005) 3925-3934.
[116] X. Hu, G.-B. Zhao, J.-J. Zhang, L. Wang and M. Radosz. Nonthermal-Plasma Reactions of Dilute Nitrogen Oxide Mixtures: NOx-in-Argon and NOx + CO-in-Argon. Industrial & Engineering Chemistry Research 43, (2004) 7456-7464.
[117] V.M. Gonzalez-Delacruz, F. Ternero, R. Pereñíguez, A. Caballero and J.P. Holgado. Study of nanostructured Ni/CeO2 catalysts prepared by combustion synthesis in dry reforming of methane. Applied Catalysis A: General 384, (2010) 1-9.
[118] J. Xu, B. Xue, Y.-M. Liu, Y.-X. Li, Y. Cao and K.-N. Fan. Mesostructured Ni-doped ceria as an efficient catalyst for styrene synthesis by oxidative dehydrogenation of ethylbenzene. Applied Catalysis A: General 405, (2011) 142-148.
[119] P.V.R. Rao, V.P. Kumar, G.S. Rao and K.V.R. Chary. Vapor phase selective hydrogenation of acetone to methyl isobutyl ketone (MIBK) over Ni/CeO2 catalysts. Catalysis Science & Technology 2, (2012) 1665-1673.
[120] R.K. Pati, I.C. Lee, S. Hou, O. Akhuemonkhan, K.J. Gaskell, Q. Wang, A.I. Frenkel, D. Chu, L.G. Salamanca-Riba and S.H. Ehrman. Flame Synthesis of Nanosized Cu−Ce−O, Ni−Ce−O, and Fe−Ce−O Catalysts for the Water-Gas Shift (WGS) Reaction. ACS Applied Materials & Interfaces 1, (2009) 2624-2635.
[121] A. Bensalem, J.C. Muller and F. Bozon-Verduraz. Faraday communications. From bulk CeO2 to supported cerium-oxygen clusters: a diffuse reflectance approach. Journal of the Chemical Society, Faraday Transactions 88, (1992) 153-154.
[122] V. Sánchez Escribano, E. Fernández López, M. Panizza, C. Resini, J.M. Gallardo Amores and G. Busca. Characterization of cubic ceria–zirconia powders by X-ray diffraction and vibrational and electronic spectroscopy. Solid State Sciences 5, (2003) 1369-1376.
[123] B.M. Reddy, L. Katta and G. Thrimurthulu. Novel Nanocrystalline Ce1−xLaxO2−δ (x = 0.2) Solid Solutions: Structural Characteristics and Catalytic Performance. Chemistry of Materials 22, (2009) 467-475.

[124] Z.-Y. Pu, J.-Q. Lu, M.-F. Luo and Y.-L. Xie. Study of Oxygen Vacancies in Ce0.9Pr0.1O2-δ Solid Solution by in Situ X-ray Diffraction and in Situ Raman Spectroscopy. The Journal of Physical Chemistry C 111, (2007) 18695-18702.
[125] L. Meng, A.-P. Jia, J.-Q. Lu, L.-F. Luo, W.-X. Huang and M.-F. Luo. Synergetic Effects of PdO Species on CO Oxidation over PdO–CeO2 Catalysts. The Journal of Physical Chemistry C 115, (2011) 19789-19796.
[126] B. Choudhury and A. Choudhury. Ce3+ and oxygen vacancy mediated tuning of structural and optical properties of CeO2 nanoparticles. Materials Chemistry and Physics 131, (2012) 666-671.
[127] B. Koubaissy, A. Pietraszek, A.C. Roger and A. Kiennemann. CO2 reforming of methane over Ce-Zr-Ni-Me mixed catalysts. Catalysis Today 157, (2010) 436-439.
[128] J. Jia, J.N. Kondo, K. Domen and K. Tamaru. Infrared Study of CO Adsorption and Oxidation over Au/Al2O3 Catalyst at 150 K. The Journal of Physical Chemistry B 105, (2001) 3017-3022.
[129] S. Sato, R. Takahashi, T. Sodesawa and N. Yamamoto. Dehydration of 1,4-butanediol into 3-buten-1-ol catalyzed by ceria. Catalysis Communications 5, (2004) 397-400.
[130] Q. Wang, B.-H. Yan, Y. Jin and Y. Cheng. Dry Reforming of Methane in a Dielectric Barrier Discharge Reactor with Ni/Al2O3 Catalyst: Interaction of Catalyst and Plasma. Energy & Fuels 23, (2009) 4196-4201.
[131] B. Delmon. How to reduce the greenhouse effect, and a few other questions concerning catalysis. Applied Catalysis B: Environmental 1, (1992) 139-147.
[132] H. Hu Yun, Advances in CO₂ Conversion and Utilization, in: ACS Symposium Series, American Chemical Society, 2010, pp. 0.
[133] Y. Lim, C.-J. Lee, Y.S. Jeong, I.H. Song, C.J. Lee and C. Han. Optimal Design and Decision for Combined Steam Reforming Process with Dry Methane Reforming to Reuse CO2 as a Raw Material. Industrial & Engineering Chemistry Research 51, (2012) 4982-4989.
[134] M. Zangouei, A.Z. Moghaddam and M. Arasteh, The influence of nickel loading on reducibility of NiO/Al 2 O 3 catalysts synthesized by sol-gel method, 2010.
[135] S.N. Naik, V.V. Goud, P.K. Rout and A.K. Dalai. Production of first and second generation biofuels: A comprehensive review. Renewable and Sustainable Energy Reviews 14, (2010) 578-597.
[136] J.C. van Dyk, M.J. Keyser and M. Coertzen. Syngas production from South African coal sources using Sasol–Lurgi gasifiers. International Journal of Coal Geology 65, (2006) 243-253.
[137] P.K. Cheekatamarla and C.M. Finnerty. Reforming catalysts for hydrogen generation in fuel cell applications. Journal of Power Sources 160, (2006) 490-499.
[138] L. Xu, H. Song and L. Chou. Carbon dioxide reforming of methane over ordered mesoporous NiO–MgO–Al2O3 composite oxides. Applied Catalysis B: Environmental 108–109, (2011) 177-190.
[139] C.-j. Liu, J. Ye, J. Jiang and Y. Pan. Progresses in the Preparation of Coke Resistant Ni-based Catalyst for Steam and CO2 Reforming of Methane. ChemCatChem 3, (2011) 529-541.
[140] X. Yan and C.-j. Liu. Effect of the catalyst structure on the formation of carbon nanotubes over Ni/MgO catalyst. Diamond and Related Materials 31, (2013) 50-57.
[141] B.H. Yan, Q. Wang, Y. Jin and Y. Cheng. Dry Reforming of Methane with Carbon Dioxide Using Pulsed DC Arc Plasma at Atmospheric Pressure. Plasma Chemistry and Plasma Processing 30, (2010) 257-266.
[142] C. Subrahmanyam, B. Louis, F. Rainone, B. Viswanathan, A. Renken and T.K. Varadarajan. Catalytic oxidation of toluene with molecular oxygen over Cr-substituted mesoporous materials. Applied Catalysis A: General 241, (2003) 205-215.
[143] X.E. Verykios. Catalytic dry reforming of natural gas for the production of chemicals and hydrogen. International Journal of Hydrogen Energy 28, (2003) 1045-1063.
[144] A. Shamsi, Methane Dry Reforming over Carbide, Nickel-Based, and Noble Metal Catalysts, in: CO₂ Conversion and Utilization, American Chemical Society, 2002, pp. 182-196.
[145] N. Wang, W. Chu, T. Zhang and X.S. Zhao. Synthesis, characterization and catalytic performances of Ce-SBA-15 supported nickel catalysts for methane dry reforming to hydrogen and syngas. International Journal of Hydrogen Energy 37, (2012) 19-30.

[146] Q. Ma, D. Wang, M. Wu, T. Zhao, Y. Yoneyama and N. Tsubaki. Effect of catalytic site position: Nickel nanocatalyst selectively loaded inside or outside carbon nanotubes for methane dry reforming. Fuel.
[147] A. Brungs, A.E. York, J. Claridge, C. Márquez-Alvarez and M.H. Green. Dry reforming of methane to synthesis gas over supported molybdenum carbide catalysts. Catalysis Letters 70, (2000) 117-122.
[148] Y.S. Mok, D.J. Koh, D.N. Shin and K.T. Kim. Reduction of nitrogen oxides from simulated exhaust gas by using plasma–catalytic process. Fuel Processing Technology 86, (2004) 303-317.
[149] S. Tang, L. Ji, J. Lin, H.C. Zeng, K.L. Tan and K. Li. CO2 Reforming of Methane to Synthesis Gas over Sol–Gel-made Ni/γ-Al2O3 Catalysts from Organometallic Precursors. Journal of Catalysis 194, (2000) 424-430.
[150] N.F.P. Ribeiro, R.C.R. Neto, S.F. Moya, M.M.V.M. Souza and M. Schmal. Synthesis of NiAl2O4 with high surface area as precursor of Ni nanoparticles for hydrogen production. International Journal of Hydrogen Energy 35, (2010) 11725-11732.
[151] D. Hu, J. Gao, Y. Ping, L. Jia, P. Gunawan, Z. Zhong, G. Xu, F. Gu and F. Su. Enhanced Investigation of CO Methanation over Ni/Al2O3 Catalysts for Synthetic Natural Gas Production. Industrial & Engineering Chemistry Research 51, (2012) 4875-4886.
[152] J. Zhang, H. Xu, X. Jin, Q. Ge and W. Li. Characterizations and activities of the nano-sized Ni/Al2O3 and Ni/La–Al2O3 catalysts for NH3 decomposition. Applied Catalysis A: General 290, (2005) 87-96.
[153] K.Y. Koo, H.-S. Roh, Y.T. Seo, D.J. Seo, W.L. Yoon and S. Bin Park. A highly effective and stable nano-sized Ni/MgO–Al2O3 catalyst for gas to liquids (GTL) process. International Journal of Hydrogen Energy 33, (2008) 2036-2043.
[154] V.R. Choudhary, A.M. Rajput and B. Prabhakar. Low temperature oxidative conversion of methane to syngas over NiO-CaO catalyst. Catalysis Letters 15, (1992) 363-370.
[155] B.B. Sahoo, N. Sahoo and U.K. Saha. Effect of H2:CO ratio in syngas on the performance of a dual fuel diesel engine operation. Applied Thermal Engineering 49, (2012) 139-146.
[156] H. Özdemir, M.A. Faruk Öksüzömer and M. Ali Gürkaynak. Preparation and characterization of Ni based catalysts for the catalytic partial oxidation of methane: Effect of support basicity on H2/CO ratio and carbon deposition. International Journal of Hydrogen Energy 35, (2010) 12147-12160.
[157] D. Li, Y. Nakagawa and K. Tomishige. Methane reforming to synthesis gas over Ni catalysts modified with noble metals. Applied Catalysis A: General 408, (2011) 1-24.
[158] A. Mosier, D. Schimel, D. Valentine, K. Bronson and W. Parton. Methane and nitrous oxide fluxes in native, fertilized and cultivated grasslands. Nature 350, (1991) 330-332.
[159] K.L. Hull, E.L. Lanni and M.S. Sanford. Highly Regioselective Catalytic Oxidative Coupling Reactions: Synthetic and Mechanistic Investigations. Journal of the American Chemical Society 128, (2006) 14047-14049.
[160] D. Kalyani, N.R. Deprez, L.V. Desai and M.S. Sanford. Oxidative C−H Activation/C−C Bond Forming Reactions: Synthetic Scope and Mechanistic Insights. Journal of the American Chemical Society 127, (2005) 7330-7331.
[161] A. Abad, P. Concepción, A. Corma and H. García. A Collaborative Effect between Gold and a Support Induces the Selective Oxidation of Alcohols. Angewandte Chemie International Edition 44, (2005) 4066-4069.
[162] S.S. Stahl. Palladium Oxidase Catalysis: Selective Oxidation of Organic Chemicals by Direct Dioxygen-Coupled Turnover. Angewandte Chemie International Edition 43, (2004) 3400-3420.
[163] H.J. Vinegar, S.L. Wellington, E.P. de Rouffignac, I.E. Berchenko and R.M. Van Hardeveld, In situ production of synthesis gas from a hydrocarbon containing formation, the synthesis gas having a selected H2 to CO ratio, in, Google Patents, 2004.
[164] D. Schanke, E. Bergene and A. Holmen, Fischer-tropsch synthesis, in, Google Patents, 2001.
[165] M. Röper, Fischer-Tropsch Synthesis, in: W. Keim (Ed.) Catalysis in C1 Chemistry, Springer Netherlands, 1983, pp. 41-88.

[166] E. Iglesia. Design, synthesis, and use of cobalt-based Fischer-Tropsch synthesis catalysts. Applied Catalysis A: General 161, (1997) 59-78.
[167] H. Schulz. Short history and present trends of Fischer–Tropsch synthesis. Applied Catalysis A: General 186, (1999) 3-12.
[168] S. Kamalifar, S. Sharifnia, M.E. Aalami-Aleagha and M.R. Panahi. Preparation and characterization of metallic catalyst using wire arc spraying and its application in partial oxidation of methane. Catalysis Communications 11, (2010) 689-693.
[169] F. Meng, G. Chen, Y. Wang and Y. Liu. Metallic Ni monolith–Ni/MgAl2O4 dual bed catalysts for the autothermal partial oxidation of methane to synthesis gas. International Journal of Hydrogen Energy 35, (2010) 8182-8190.
[170] R. Sabori, S. Sharifnia, M.E. Aalami-Aleagha and M.R. Panahi. Promotion of Metallic Catalysts by Metal Oxide Powders in Partial Oxidation of Methane. Journal of the Taiwan Institute of Chemical Engineers 43, (2012) 153-158.
[171] Y. Wang, W. Wang, X. Hong, Y. Li and Z. Zhang. Yttrium-stabilized zirconia-promoted metallic nickel catalysts for the partial oxidation of methane to hydrogen. International Journal of Hydrogen Energy 34, (2009) 2252-2259.
[172] A.C. Ferreira, A.M. Ferraria, A.M.B. do Rego, A.P. Gonçalves, A.V. Girão, R. Correia, T.A. Gasche and J.B. Branco. Partial oxidation of methane over bimetallic copper–cerium oxide catalysts. Journal of Molecular Catalysis A: Chemical 320, (2010) 47-55.
[173] M. Morales, F. Espiell and M. Segarra. Performance and stability of La0.5Sr0.5CoO3−δ perovskite as catalyst precursor for syngas production by partial oxidation of methane. International Journal of Hydrogen Energy 39, (2014) 6454-6461.
[174] G. Nahar and V. Dupont. Hydrogen production from simple alkanes and oxygenated hydrocarbons over ceria–zirconia supported catalysts: Review. Renewable and Sustainable Energy Reviews 32, (2014) 777-796.
[175] Y. Wei, H. Wang and K. Li. Ce-Fe-O mixed oxide as oxygen carrier for the direct partial oxidation of methane to syngas. Journal of Rare Earths 28, (2010) 560-565.
[176] M. Okumoto, B.S. Rajanikanth, S. Katsura and A. Mizuno. Nonthermal plasma approach in direct methanol synthesis from CH₄. Industry Applications, IEEE Transactions on 34, (1998) 940-944.
[177] E.M. Wilcox, G.W. Roberts and J.J. Spivey. Direct catalytic formation of acetic acid from CO2 and methane. Catalysis Today 88, (2003) 83-90.
[178] X. Zhang, D.H. He, Q.J. Zhang, B.Q. Xu and Q.M. Zhu, Methanol from oxidation of methane over MoOx/La-Co-oxide catalysts, in: B. Xinhe, X. Yide (Eds.) Studies in Surface Science and Catalysis, Elsevier, 2004, pp. 541-546.
[179] R.S. Liu, M. Iwamoto and J.H. Lunsford. Partial oxidation of methane by nitrous oxide over molybdenum oxide supported on silica. Journal of the Chemical Society, Chemical Communications 0, (1982) 78-79.
[180] H.F. Liu, R.S. Liu, K.Y. Liew, R.E. Johnson and J.H. Lunsford. Partial oxidation of methane by nitrous oxide over molybdenum on silica. Journal Name: J. Am. Chem. Soc.; (United States); Journal Volume: 106:15 (1984) Medium: X; Size: Pages: 4117-4121.
[181] J.H. Lunsford. Catalytic conversion of methane to more useful chemicals and fuels: a challenge for the 21st century. Catalysis Today 63, (2000) 165-174.
[182] V. Ravi, Y.S. Mok, B.S. Rajanikanth and H.-C. Kang. Temperature effect on hydrocarbon-enhanced nitric oxide conversion using a dielectric barrier discharge reactor. Fuel Processing Technology 81, (2003) 187-199.
[183] C. Subrahmanyam, A. Renken and L. Kiwi-Minsker. Novel catalytic non-thermal plasma reactor for the abatement of VOCs. Chemical Engineering Journal 134, (2007) 78-83.
[184] S.S. Shepelev, H.D. Gesser and N.R. Hunter. Light paraffin oxidative conversion in a silent electric discharge. Plasma Chemistry and Plasma Processing 13, (1993) 479-488.

[185] Seung-Soo Kim, Hwaung Lee , Hyung Keun Song , and Byung-Ki Na , Plasma Catalytic Reaction of Methane with Sol-Gel-Derived Pt/γ-Al2O3 Catalyst in Dielectric-BarrierDischarge Reactor. J. Ind. Eng. Chemistry 12, (2006) 558-565.
[186] C.-j. Liu, G.-h. Xu and T. Wang. Non-thermal plasma approaches in CO2 utilization. Fuel Processing Technology 58, (1999) 119-134.
[187] T. Nozaki, A. Hattori and K. Okazaki. Partial oxidation of methane using a microscale non-equilibrium plasma reactor. Catalysis Today 98, (2004) 607-616.
[188] G. Petitpas, J.D. Rollier, A. Darmon, J. Gonzalez-Aguilar, R. Metkemeijer and L. Fulcheri. A comparative study of non-thermal plasma assisted reforming technologies. International Journal of Hydrogen Energy 32, (2007) 2848-2867.
[189] B. Christian Enger, R. Lødeng and A. Holmen. A review of catalytic partial oxidation of methane to synthesis gas with emphasis on reaction mechanisms over transition metal catalysts. Applied Catalysis A: General 346, (2008) 1-27.
[190] G.P. Berrocal, A.L.M.D. Silva, J.M. Assaf, A. Albornoz and M.d.C. Rangel. Novel supports for nickel-based catalysts for the partial oxidation of methane. Catalysis Today 149, (2010) 240-247.
[191] V.A. Kirillov, Z.A. Fedorova, M.M. Danilova, V.I. Zaikovskii, N.A. Kuzin, V.A. Kuzmin, T.A. Krieger and V.D. Mescheryakov. Porous nickel based catalysts for partial oxidation of methane to synthesis gas. Applied Catalysis A: General 401, (2011) 170-175.
[192] Q. Miao, G. Xiong, S. Sheng, W. Cui, L. Xu and X. Guo. Partial oxidation of methane to syngas over nickel-based catalysts modified by alkali metal oxide and rare earth metal oxide. Applied Catalysis A: General 154, (1997) 17-27.
[193] T.-J. Huang and C.-H. Wang. Methane decomposition and self de-coking over gadolinia-doped ceria-supported Ni catalysts. Chemical Engineering Journal 132, (2007) 97-103.
[194] A.S. Larimi and S.M. Alavi. Ceria-Zirconia supported Ni catalysts for partial oxidation of methane to synthesis gas. Fuel 102, (2012) 366-371.
[195] M.D. Salazar-Villalpando and B. Reyes. Hydrogen production over Ni/ceria-supported catalysts by partial oxidation of methane. International Journal of Hydrogen Energy 34, (2009) 9723-9729.
[196] E. Poggio Fraccari, O. D'Alessandro, J. Sambeth, G. Baronetti and F. Mariño. Ce–Mn mixed oxides as supports of copper- and nickel-based catalysts for water–gas shift reaction. Fuel Processing Technology 119, (2014) 67-73.
[197] E. Poggio-Fraccari, F. Mariño, M. Laborde and G. Baronetti. Copper and nickel catalysts supported on praseodymium-doped ceria (PDC) for the water-gas shift reaction. Applied Catalysis A: General 460–461, (2013) 15-20.
[198] E. Poggio-Fraccari, J. Sambeth, G. Baronetti and F. Mariño. Cu/MnOx–CeO2 and Ni/MnOx–CeO2 catalysts for the water–gas shift reaction: Metal–support interaction. International Journal of Hydrogen Energy.
[199] J.-H. Lin, P. Biswas, V.V. Guliants and S. Misture. Hydrogen production by water–gas shift reaction over bimetallic Cu–Ni catalysts supported on La-doped mesoporous ceria. Applied Catalysis A: General 387, (2010) 87-94.
[200] D. Gamarra, A. Hornés, Z. Koppány, Z. Schay, G. Munuera, J. Soria and A. Martínez-Arias. Catalytic processes during preferential oxidation of CO in H2-rich streams over catalysts based on copper–ceria. Journal of Power Sources 169, (2007) 110-116.
[201] A. Hornés, D. Gamarra, G. Munuera, J.C. Conesa and A. Martínez-Arias. Catalytic properties of monometallic copper and bimetallic copper-nickel systems combined with ceria and Ce-X (X = Gd, Tb) mixed oxides applicable as SOFC anodes for direct oxidation of methane. Journal of Power Sources 169, (2007) 9-16.
[202] A. Hornés, D. Gamarra, G. Munuera, A. Fuerte, R.X. Valenzuela, M.J. Escudero, L. Daza, J.C. Conesa, P. Bera and A. Martínez-Arias. Structural, catalytic/redox and electrical characterization of systems combining Cu–Ni with CeO2 or Ce1−xMxO2−δ (M = Gd or Tb) for direct methane oxidation. Journal of Power Sources 192, (2009) 70-77.

[203] M. Magureanu, N.B. Mandache, J. Hu, R. Richards, M. Florea and V.I. Parvulescu. Plasma-assisted catalysis total oxidation of trichloroethylene over gold nano-particles embedded in SBA-15 catalysts. Applied Catalysis B: Environmental 76, (2007) 275-281.
[204] S.L. Yao, T. Takemoto, F. Ouyang, A. Nakayama, E. Suzuki, A. Mizuno and M. Okumoto. Selective Oxidation of Methane Using a Non-Thermal Pulsed Plasma. Energy & Fuels 14, (2000) 459-463.

LIST OF PUBLICATIONS BASED ON THE THESIS WORK

1. **Sk. Mahammadunnisa**, E.L. Reddy, P. M. K. Reddy and Ch. Subrahmanyam., A facile approach for direct decomposition of nitrous oxide assisted by nonthermal plasma, **Plasma Processes and Polymers. 2013; 10(5):444-450.**
2. **Sk. Mahammadunnisa**, E.L. Reddy, J. C. Whitehead and Ch. Subrahmanyam., CO_2 reduction to syngas and carbon Nanofibres by plasma assisted in-situ decomposition of water, **International Journal of Greenhouse Gas Control, 2013; 16(16):361-363.**
3. **Sk. Mahammadunnisa**,P. M. K. Reddy, and Ch. Subrahmanyam., dry reforming assisted non-thermal plasma catalytic reactor, **ACS Energy & Fuels 2013, *27* (8), 4441–4447**
4. **Sk. Mahammadunnisa**, P. M. K. Reddy, E.L. Reddy, and Ch. Subrahmanyam., Catalytic DBD plasma reactor for CO oxidation by in-situ N_2O decomposition, **Catalysis Today, 2013; 211:53-57.**
5. **Sk. Mahammadunnisa**, P. M. K. Reddy and Ch. Subrahmanyam., Nonthermal plasma assisted co-processing of CH_4 and N_2O for methanol production **RSC Advances 2014, 4, 4034-4036.**
6. **Sk. Mahammadunnisa** and Ch. Subrahmanyam., Catalytic plasma assisted processing of CH_4 and N_2O for methanol production **(Communicated to applied catalysis A).**

PRESENTATIONS IN INTERNATIONAL CONFERENCES

1. **Sk. Mahammadunnisa,** P. M. K. Reddy, and Ch. Subrahmanyam., Catalytic DBD plasma reactor for CO oxidation by in-situ N_2O decomposition. **2012 International Symposium on Plasmas for Catalyses and Energy Materials (ISPCEM-2012)** September 21-24, 2012; **Tianjin, China.**
2. **Sk. Mahammadunnisa,** P. M. K. Reddy, and Ch. Subrahmanyam., Catalytic Dry Reforming Assisted Nonthermal Plasma Catalytic Reactor .**AIChE2012** Oct 28 - Nov 2, 2012; **Pittsburgh, USA.**
3. **Sk. Mahammadunnisa,** P. M. K. Reddy, and Ch. Subrahmanyam., Nonthermal plasma assisted co-processing of CH_4 and N_2O for methanol production assisted by Non thermal plasma-DBD reactor. **AIChE2013** Nov 3 - Nov 8, 2013; **SanFrancisco, CA, USA.**

PRESENTATIONS IN NATIONAL CONFERENCES

4. **Sk. Mahammadunnisa,** P. M. K. Reddy, and Ch. Subrahmanyam., DBD plasma reactor for CO oxidation by in-situ N_2O decomposition., **21st National Symposium on Catalysis (PLASMA-2012)** 10-13 February, 2013; **IICT Hyderabad, India.**